Title

Connecting Molecular to Macroscale Adhesion for the Design of Robust Underwater Adhesives

Permalink

https://escholarship.org/uc/item/311893dj

Author

Lamberty, Zachary Dylan

Publication Date

2023

Connecting Molecular to Macroscale Adhesion for the Design of Robust Underwater Adhesives

By

Zachary Lamberty

A dissertation submitted in partial satisfaction of the

requirements for the degree of

Doctor of Philosophy

in

Chemical Engineering

in the

Graduate Division

of the

University of California, Berkeley

Committee in charge:

Professor Joelle Frechette, Chair
Professor Rui Wang
Professor Phillip Messersmith

Fall 2023

Connecting Molecular to Macroscale Adhesion for the Design of Robust Underwater Adhesives

Zachary Lamberty

Abstract

Connecting Molecular to Macroscale Adhesion for the Design of Robust Underwater Adhesives

by

Zachary Lamberty

Doctor of Philosophy in Chemical Engineering

University of California, Berkeley

Professor Joelle Frechette, Chair

Adhesives are required to bond to wet surfaces for everyday applications including wound closure tapes, wearable devices, naval repairs, or even in the everyday exposure of commonplace adhesives to humid environments. Yet adhesion is notoriously difficult to wet surfaces – water weakens the intermolecular forces necessary for adhesion and creates interfacial layers separating the adhesive and substrate. Recent progress in improving underwater adhesion has come in part through the inclusion of multidentate groups in adhesives – chemical functionalities with multiple adjacent attachment points, which are believed to make the bond more stable. While molecular scale studies of multidentate groups have supported the macroscale findings of improved underwater adhesion for multidentate adhesives, we have yet to fully understand how the dynamic nature of these bonds impacts the overall adhesive strength of the material.

Connecting macroscale adhesion to the strength and dynamics of interfacial bonds is notoriously hard. Adhesive strength results from a complex combination of physics, including energy dissipated in breaking interfacial bonds, local elastic and plastic deformation near the crack tip, and viscous dissipation within the adhesive as it stretches. The convolution of these mechanisms makes it challenging for researchers to isolate the role of interfacial chemical bonds on overall adhesion, yet understanding each facet is crucial for the rational design and improvement of adhesives. Untangling the role of interfacial chemistry in adhesion using model systems will inform the development of future adhesives.

In this thesis we will develop tools and methods to elucidate the effects of dynamic chemical bonds at an interface on the macroscale adhesive strength and apply these methods to the study of a model tridentate hydrogen bonding epoxy adhesive. First we will present the development of a novel technique to fabricate reactive metal surfaces with extremely low surface roughness. Controlling surface roughness is crucial to measuring adhesion and interfacial forces, as surface roughness can obscure the nanoscale phenomena of interest and variations in contact area due to roughness can skew measured adhesive strengths. By thermally evaporating reactive aluminum onto a smooth mica template, followed by removal of the template in water, we obtain uniform Al/AlO_3 surfaces of < 0.2 nm RMS roughness, rivaling the smoothness of the best noble metal

films. We then demonstrate the applications for these films by improving the estimate of the surface energy of aluminum through adhesion measurements, measuring the surface potential of aluminum in LiCl electrolyte solutions, and reporting improved the corrosion resistance of the ultra-smooth films.

We next investigate the adhesion of a model epoxy adhesive (diglycidyl ether of bisphenol A, DGEBA) containing tridentate hydrogen bonding moieties (tris(hydroxymethyl)amino methane, Tris) to determine the mechanism underlying the strong underwater adhesion of DGEBA-Tris. We first present a model to relate the bond activation energy to the macroscale adhesive strength of a material, and then use self-arresting crack measurements to demonstrate that tridentate adhesives follow predicted adhesive behavior. We next utilize a Surface Forces Apparatus to show that Tris-epoxies exhibit robust adhesion to both mica and ultra-smooth aluminum substrates in water. Finally, we establish that the adhesive strength of DGEBA-Tris epoxies reveals a bond activation energy of 26.6 ± 0.03 kBT in air and 30.3 ± 0.6 kBT in water. These activation energies suggest that adhesion is dominated by tridentate Hydrogen bonds in both air and water, allowing the adhesive to maintain its bonding strength in water.

We subsequently extend our insight into multidentate bonding by exploring the adhesive behavior of DGEBA-Tris polymers as a function of curing and of measurement temperature. We first identify a characteristic threshold velocity, above which DGEBA-Tris polymers exhibit amplified adhesion strength with increased velocity. We then show that while the equilibrium adhesion only minorly increases with cure, the threshold velocity rises dramatically due the increased extensibility of the longer polymer chains after cure. Next, we observe a small growth in zero-velocity adhesion as the temperature is raised from 9 °C to 60 °C which is again eclipsed by the large increase in threshold velocity. The variation of threshold velocity with temperature is shown to follow an Arrhenius dependence, suggesting that the adhesive fracture proceeds through the activated rupture of interfacial bonds. The bond strength is then estimated to be $35 \pm 4\, k_B T$ at 20 °C, providing further evidence that DGEBA-Tris adhesives form cooperative tridentate hydrogen bonds.

Contents

List of Figures

List of Tables

Acknowledgements

This thesis would not have been possible without the support of many different people and organizations for which I am deeply thankful. First of all, much of the work was funded and inspired by the United States Army Research Laboratory (ARL) under Cooperative Agreement Number W911NF-12-2-0022. Further financial support was supplied by the National Science Foundation (CMMI 1728082) and the American Chemical Society (ACS-PRF ND5-58606).

I am eternally grateful to my advisor Joelle Frechette for providing me the opportunity to pursue my studies at two premier universities and for her unending wisdom and support. She has continually challenged me to become a more effective researcher and a better scientist, never allowing me to stagnate. As we faced a global pandemic, cross-country move, and worker strike she showed me how to be adaptable and resilient in any situation. I would not be the person I am today without her.

I am so very thankful for my collaborators throughout my Ph.D., particularly Dr. Daniel Knorr and Dr. Ngon Tran at ARL, who provided much of the impetus for my work, continual guidance, and generous funding to make my studies possible. I am thankful for Patty McGuiggan at the Johns Hopkins University for her many conversations and guidance on the SFA, AFM, and adhesion. Furthermore, I am appreciative of the professors who have impacted me through my time at both Johns Hopkins and at Berkeley, and for my qualifying exam committee members, Prof. Rui Wang, Prof. Roya Maboudian, Prof. Karthik Shekhar, and Prof. Phillip Messersmith.

I am further indebted to the many scientists and students I have had the pleasure of working alongside. First and foremost is Dr. Christian van Engers, who mentored and guided me during my first year in the lab. Christian taught me how to be a diligent, meticulous, and effective scientist, and how to have fun while doing it. I am thankful for the many collaborations and discussions I had with Dr. Preeitka Karnal, Dr. Marina Pasquet, Dr. Anushka Jha, Dr. Sarah Berlinger, Yu Fu, Peiyao Wu, Lidya Gebremeskel, Devin Schinski, and Margaret Shen. I am additionally grateful for those who I taught as students or mentored as researchers, including Luke Pretzie, Junhao Liang, and Armstrong Gbessagee.

I could not have overcome the challenges of a Ph.D. without the support of my many friends along the way, including Derek Vandyke, Eli Kissman, Jessica de Oliveira Carminato, Bennett Parrish, Lanson Tang, Yu Fu, Marina Pasquet, Peiyao Wu, Preetika Karnal, and Peter Corkery. Thank you for continuing to provide joy in my life.

I would not be here today without the love and support of my parents and of my sister Erin, who have always had my back, supported my passions, and encouraged me to continue pushing myself. I am further indebted to all of my grandparents, Lou and Pat Lamberty and Ralph and Sandy Carpenter, who have all done so much to support me through all my studies.

Last but certainly not least, I am overwhelmingly grateful for my wife April, who has supported me through both the most stressful and the most exciting of times, through multiple coast-to-

coast moves, and the day-to-day challenges of life. There’s no one I’d rather have by my side as we confront our next adventure.

Introduction

1.1 Motivation

We rely upon adhesives every day to stick objects together. While many of us are familiar with sticky notes, bandages, and super glue, adhesives also are hidden behind a myriad of objects.[1] Adhesives hold phone screens together,[2] fasten furniture segments,[3] and bond nonwoven textile layers including in carpets and medical fabrics.[4] Adhesives are also critical to composites of fiberglass, carbon fiber, and aluminum – the strong, lightweight materials that have revolutionized the construction of airplanes, boats, cars, and buildings in recent decades.[5-7] Composites consist of two or more dissimilar materials that are bonded together, typically using an adhesive. The ability of the adhesive to hold the materials together is crucial to the strength of the composite material, and so a strong, durable adhesive is needed for the composite to last reliably for years.[8]

One of the major weaknesses of the stiff structural adhesives used for composites is water.[9, 10] Water weakens the intermolecular bonds that hold the adhesive to the adherend, lowering the ability of the adhesive to stick onto the surface.[11, 12] Water is also notoriously difficult to remove from the adherend surface, forming strongly bound interfacial layers that impede adhesion.[13] Sticking to wet surfaces is important for medical adhesives and wearable devices, since the surfaces of our bodies are covered in water.[14, 15] Underwater adhesion is also of great interest for maritime repairs, where the ability to patch ship hulls *in situ* would greatly improve the safety and reliability of these crafts.[12]

Just as important but less obvious is the durability of dry-bonded adhesives and composites that are later exposed to water.[9] Water is adept at migrating through cured adhesives to the interface, weaking the adhesion and ultimately leading to degradation and failure of the composite.[10] This can happen through direct exposure to water via rain or immersion but can also occur merely through repeated exposure to humid air.[16, 17] Anyone who has had a bandage fall off while swimming has witnessed water-induced adhesive failure. For composite materials used in structures or transportation, such a failure could be catastrophic.

In order to improve the underwater adhesion of composite materials, we must understand the interactions between water and an adhesive at the interface and work to develop chemistries that are able to bond strongly in water.[18, 19] As part of this task we must further our understanding of how molecular-scale surface forces can add up to generate a macroscale adhesive force and make our glues sticky.[20] The goal of directly relating an adhesive's chemical structure to the overall adhesive strength has long been sought by scientists to enable the *a priori* design and tuning of adhesive properties through leveraging molecular chemistry insight.[21-23] However, obtaining these structure-property relationships has proven far from easy, particularly at the interfacial level – it is extremely complex to capture all the multiscale dynamics of play, from the transfer of force from the molecular bond to the polymer chain, and subsequently the bulk polymer and onto the adherend.[20, 24, 25] Towards this goal, this thesis will develop experimental methods and theories to relate the strength of a single interfacial bond to the overall adhesive strength of the material.

1.2 Thesis outline

This thesis will connect macroscale adhesive experiments to state-of-the-art multiscale adhesion theories, allowing us to determine the molecular mechanisms behind a promising underwater structural adhesive.

Chapter 2 summarizes the theories and methodology that this thesis builds upon. We will build a foundation on the fundamental concepts in adhesion, including defining adhesion through the strain energy release rate and how surface forces, interfacial chemistry, and surface roughness affect adhesion. We will also describe relevant techniques used to measure adhesive strength, notably the JKR apparatus, Surface Forces Apparatus (SFA), and peeling measurements. We will then present a background of previous theories to relate molecular to macroscale adhesion, from van der Waals forces to Lake-Thomas and onto macroscale velocity-dependent models, and then discuss pitfalls and challenges in multiscale adhesion measurements, including avoiding surface roughness and viscoelasticity.

Chapter 3 describes a technique to fabricate ultra-smooth reactive metal (aluminum) films and demonstrate the use of these model surfaces to measure previously inaccessible surface sensitive phenomena.[26] Ultra-smooth aluminum films are created by first depositing aluminum onto freshly cleaved mica surfaces, then carefully removing the mica template underwater. The use of the smooth mica template reduces the RMS roughness of the aluminum from 0.9 nm (as-deposited) to <0.2 nm. We then show that the films produced *via* this method are of sufficient optical quality for SFA measurements, and that the smooth films have nearly 6-fold higher adhesion against mica in N_2 than the rough films due to improved molecular contact. We then report measurements of the surface potential of the smooth aluminum surfaces in LiCl solution, demonstrating that these films can be used for electrochemical studies. Finally, we show that smooth aluminum films exhibit suppressed corrosion in 5mM NaCl solution, with implications for our understanding of corrosion mechanisms.

Chapter 4 presents a theory to relate the velocity dependence of adhesive strength to the molecular bond strength at the interface.[27] We further apply this theory to elucidate the mechanism of DGEBA-Tris, a recently developed underwater structural adhesive suspected to function through cooperative tridentate hydrogen bonds. We first use self-arresting crack propagation in air to show that the adhesion of DGEBA-Tris with mica increases with velocity in the range of 5 nm/s – 5 μm/s, control experiments do not exhibit enhanced adhesion with velocity. We then employ the SFA to demonstrate that underwater adhesion of DGEBA-Tris with mica or aluminum is as strong as with mica/aluminum in N_2. We next determine the crack velocity at adhesive failure to reveal similar scaling of strain energy release rate as seen in air. Finally, we estimate the bond energy between DGEBA-Tris and mica to be between $23k_BT$ and $31k_BT$, proving that cooperative tridentate hydrogen bonds are responsible for the remarkable underwater adhesive properties of this material.

Chapter 5 builds upon the theories and methods of Chapter 4 to further understand the process of bond scission during adhesive debonding. Self-arresting crack propagation is used to investigate the role of cure, temperature, and velocity on the adhesion of DGEBA-Tris. DGEBA-Tris adhesives are first shown to exhibit increased adhesion with velocity, which begins after a characteristic threshold velocity. Increasing the cure of DGEBA-Tris is shown to only minorly affect the equilibrium adhesion yet drastically increase the threshold velocity, due to softening of the polymer chain with increased molecular weight. Increasing the measurement temperature between 9 – 60 ºC is then shown to also increase the transition velocity dramatically. The dependence of threshold velocity on temperature is shown to follow an Arrhenius-like dependence with a bond strength of $35 \pm 4\, k_B T$ at 20 ºC, confirming that DGEBA-Tris adhesives bond cooperatively at an interface and that adhesive debonding occurs through an activated process.

Chapter 6 concludes by providing an overview of my contributions in connecting molecular to macroscale adhesion and improving underwater adhesive chemistries. We discuss remaining challenges in obtaining molecular information from macroscale force measurements as well as in developing adhesives for improved underwater durability and strength. Finally, we suggest future directions in understanding how adhesives form contact underwater and in developing more robust models for relating molecular to macroscopic fracture.

2 Background

2.1 Fundamentals of adhesion

2.1.1 Forces underlying adhesion

At its heart, adhesion is the measure of how sticky something is. For something to be sticky it must have attractive forces that hold it onto another object. These attractive forces come from interactions at the interface of the adhesive. For most adhesives the primary interfacial interactions behind adhesion are van der Waals forces and hydrogen bonds, although other types of interactions have been leveraged for adhesion.[8] Van der Waals forces are present between all molecules, resulting from interactions between permanent dipoles, induced dipoles, and instantaneous dipoles in molecules.[28] Van der Waals forces between individual molecules can be quite weak and short range, but can become surprisingly strong and long-ranged between macroscopic surfaces.[29] Hydrogen bonds (H-bonds) are a particularly strong dipole-dipole interaction that occurs between an electron accepting group (H) and an electron donating group (O or N, often).[28] These interactions require H-bond accepting and donating groups to be in close proximity (roughly 0.175 nm), and are both stronger and more directional than van der Waals forces.[28] Covalent bonds, where electrons are shared between atoms,[15, 30] and coordination bonds, where the two shared electrons come from a single atom,[31] have been reported in adhesives but are uncommon.

Beyond surface interactions, the strength of an interfacial bond depends on how force is transferred from the point of loading to the interface.[32] This depends on the geometry of the system, which will be discussed in depth later, but also upon the bulk properties of the adhesive. Energy that is stored in elastic deformation of the adhesive or lost due to dissipative effects, such as viscoelasticity, will not be transferred to the interface and therefore will not work to break interfacial bonds.[20, 23] Dissipation during stretching can serve to amplify the forces at the interface and subsequently the overall adhesion, particularly for soft adhesives that can deform substantially before detaching.[33]

2.1.2 Quantifying adhesion

Adhesive theories generally begin with a crack that forms between the two materials (**Fig. 2.1**). The interfacial forces, including intermolecular bonds, will hold the two materials together and act to close the crack (retreat to the right in **Fig. 2.1**). An applied tensile force will work to pull the two materials apart, advancing the crack leftwards by breaking interfacial bonds. It takes a finite energy (per unit area) to extend the crack, as interactions between the two materials at the interface will be lost in the newly opened region. In the most basic picture, for two identical materials in a vacuum, this energy can be thought of as twice the surface energy γ of the material, the energy required per unit area to extend a surface.[28]

$$W = 2\gamma, \tag{2.1}$$

where W is the thermodynamic work of adhesion, and the factor of two arises as a result of two new surfaces being created as the crack is opened. If the two materials are different, **Eqn. 2.1** can be modified into[8]

$$W = \gamma_a + \gamma_s - \gamma_{as}, \qquad (2.2)$$

where γ_a is the surface energy of the adhesive, γ_s the surface energy of the substrate, and γ_{as} the interfacial free energy between the adhesive and substrate.

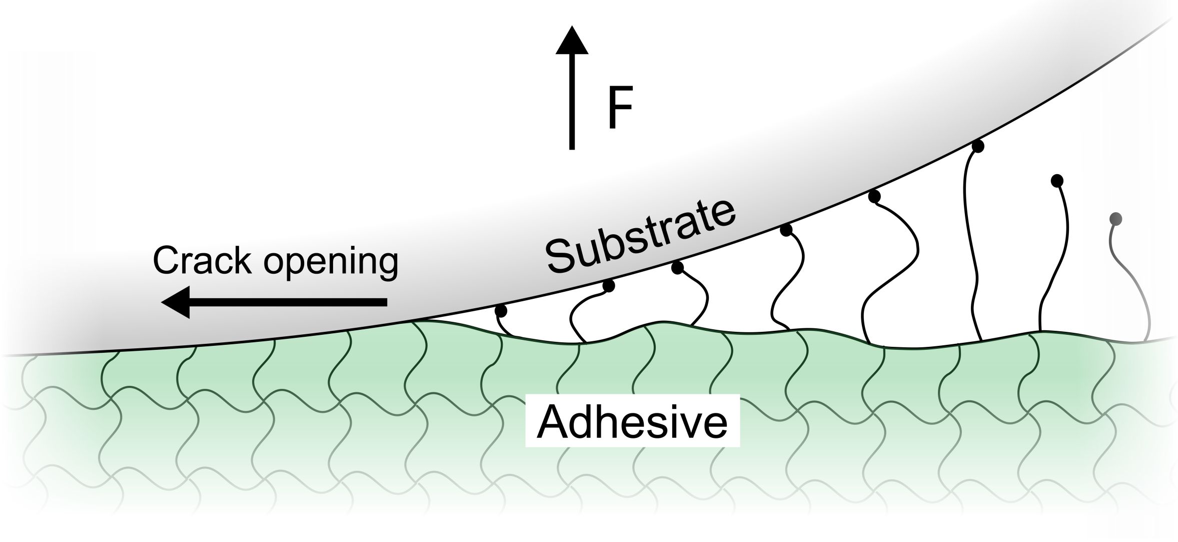

Figure 2.1 Microscopic view of a crack. Illustration of the opening of a crack between an adhesive and the opposing substrate. As a force is applied, the crack opens (advances leftwards), but interfacial bonds hold the surfaces together and resist crack motion.

In practice, the measured adhesion is almost always significantly larger than the predicted values of W.[8, 34] In general, a measurement of the surface energy is not adequate to predict the behavior of most adhesives, as the complexity of the system defies easy simplification to the wetting properties at the interface.[28] This discrepancy is partially due to fact that adhesion measurements are generally not reversible; energy losses occur in adhesive during finite-velocity tests that work to increase the measured adhesion.[35, 36] Other effects that can lead to deviations from W include hysteresis within the materials, time-dependent changes in the interface (contact aging), and roughness of the surfaces altering the true contact area.[8, 28]

Instead, a more rigorous definition of adhesion can include irreversible phenomena by conducting an energy balance between the applied load and the corresponding elastic deformation of the materials to obtain:[37]

$$\frac{\partial U_M}{\partial A} - \frac{\partial U_E}{\partial A} = \frac{\partial U_s}{\partial A} \equiv G. \quad (2.3)$$

In this equation U_M is the applied (mechanical) energy due to the force F, U_E is the energy stored in elastic deformation, and A is the area of contact. The remaining energy, U_S, is the energy that resists detachment, which is used to define G, the strain energy release rate. G is a robust measure of adhesion, including contributions and losses from both the interface and the bulk of the system. However, G is not a directly measurable quantity, and further models must be employed to extract G from experimental data.

2.1.3 Contact mechanics

Determining G from experiments requires knowledge of how measurable quantities (*e.g.* force, contact area, and indentation depth) are affected by adhesion. The exact relationship is highly dependent on the geometry of contact and thus a myriad of models have been utilized to suit the needs of each system.[38] Here we will present only those that are most relevant for this thesis, as well as background required to understand these models.

2.1.3.1 Sphere-on-flat (Hertz and JKR)

The contact between a sphere and a flat surface (or two spheres) was first studied by Hertz in 1882, who derived a model to relate the applied force F to the contact radius a and indentation depth δ in the case where no adhesion exists between the materials:[39]

$$F = \frac{4E^* a^3}{3R}. \quad (2.4)$$

In **Eqn. 2.4**, R is the radius of curvature of the sphere, as shown in **Fig. 2.2**, and E^* is the reduced elastic modulus, $E^* = \frac{1-\nu_1^2}{E_1} + \frac{1-\nu_2^2}{E_2}$, where ν_1 and E_1 are the Poisson's ratio and elastic modulus of material 1, respectively. The corresponding equation for the indentation depth is given by:[32]

$$a = \sqrt{R\delta}. \quad (2.5)$$

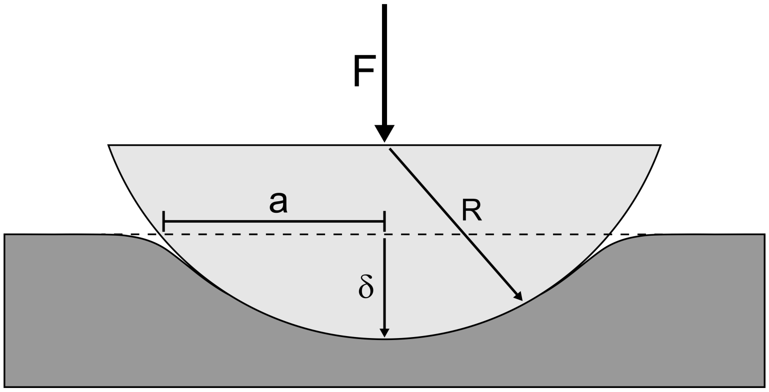

Figure 2.2 Diagram of sphere-on-flat contacts. Illustration showing the key parameters in a sphere-on-flat geometry, including the force F, contact radius a, radius of curvature R, and indentation depth δ.

In 1971 Johnson, Kendall, and Roberts extended Hertz theory to include adhesion, yielding **Eqn. 2.6**:[40]

$$a^3 = \frac{3R}{4E^*}\left(F + 3\pi GR + (6\pi GRF + (3\pi GR)^2)^{\frac{1}{2}}\right). \tag{2.6}$$

Eqn. 2.6 predicts that adhesion allows for a finite contact area at zero force, and that the materials will remain adhered under tensile force until $\frac{dF}{da} = 0$, when an elastic instability is reached and the materials will exhibit sudden adhesive failure. At this point **Eqn. 2.6** reduces to:[41]

$$\frac{F_C}{R} = -\frac{3}{2}\pi G_C, \tag{2.7}$$

where the subscript $_C$ indicates a critical value occurring at an instability point. Interestingly, **Eqn. 2.7** does not depend on the elastic modulus of the materials, allowing one to obtain a measure of G without explicit knowledge of the material stiffness. However, it should be noted that **Eqns 2.6** and **2.7** are only applicable for isotropic, linearly elastic materials, and they work best for large, soft materials where the scale of deformation is much larger than the range of surface forces.[41]**Eqn. 2.6** can also be generalized for different geometries if the compliance C of the system is known, yielding:[42]

$$G = -\frac{(F' - F)^2}{4\pi a}\frac{\partial C}{\partial a}\bigg|_F, \tag{2.8}$$

where F' is the Hertzian (non-adhesive) force required to generate the same contact area, given by **Eqn. 2.4**. This relationship is particularly useful in describing contacts with cylindrical punches and may also be modified to account for finite thickness effects.[43]

2.1.3.2 Peeling

A peel test is one of the most common methods used to probe adhesion.[44, 45] Often, a force is applied to the specimen at a set angle until the adhesive begins to peel off at a fixed velocity, which occurs at the critical force F_C of:[44]

$$\frac{F_c}{w} = E^* d(1 - \cos\theta) + \sqrt{\left(E^* d(1 - \cos\theta)\right)^2 + 2E^* d G_C}, \tag{2.9}$$

where w and d are the width and thickness of the peeled specimen and θ is the angle at which the peeling occurs (see **Fig. 2.3**). For a 90° peel, and where the elastic stretching of the peeled material is negligible, **Eqn. 2.9** becomes simply:[44]

$$F_{C,90^o} = wG_C. \tag{2.10}$$

It is also possible to measure adhesion through peeling not by controlling the peel force but through observing the distance that is peeled upon a given force or loading. One adroit method using this concept involves using a spacer to separate the materials at one end by a known amount, forming a crack and bending the more pliable material (**Fig. 2.3**).[46] The bending moment thus created is resisted by the adhesion between the two materials, and the balance between adhesive and bending energies results in a crack of length ℓ:[47]

$$G = \frac{9\mu d^3 h^2}{24\ell^4}. \tag{2.11}$$

Here μ is the shear modulus of the top sheet, d is thickness of the top sheet, and h is the height of the spacer. Since this method results in a crack of stable length, it is referred to as self-arresting crack propagation.

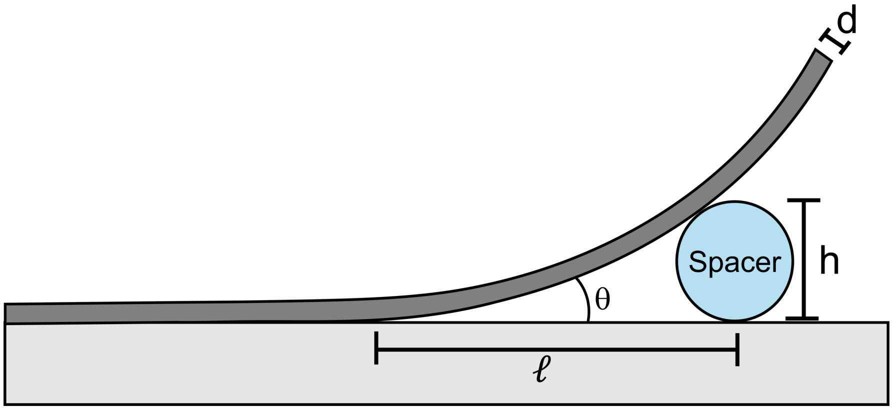

Figure 2.3 Diagram of self-arresting crack propagation measurements. Schematic showing the key parameters in self-arresting crack propagation, where ℓ is the crack length, h is the spacer height, d is the thickness of the bent sheet, and θ is the peeling angle.

2.2 Connecting molecular interactions to adhesion

For decades scientists have sought to relate the forces experienced between molecules to the interactions and phenomena experienced at larger length scales.[28] Some of the earliest advances came through the study of van der Waals forces. Between individual molecules, van der Waals forces decay proportionally to $1/D^6$, where D is the separation between the molecules.[37] In the 1930s, researchers including Hamaker, de Boer, and Derjaguin, showed that one can sum up each pairwise interaction between molecules to encompass all the molecules in two surfaces, thereby giving the van der Waals interaction between the two surfaces.[37] For two infinite planar surfaces, the interaction energy W per unit area due to van der Waals forces is:[29]

$$W = -\frac{A}{12\pi D^2}, \tag{2.12}$$

where A is the Hamaker constant for the materials and intervening medium. The dependence of macroscopic van der Waals interactions with $1/D^2$ makes these interactions markedly stronger and longer-range than their molecular analogs, accounting for their importance in everyday phenomena such as adhesion and wetting. The Hamaker constant itself can be related to the dielectric properties of the materials through Lifshitz theory, which allows for direct calculation of the macroscopic interactions through knowledge of the optical properties of the materials.[28]

Van der Waals forces are amenable to modeling in adhesion since they are instantaneous, invariant with time, and only depend on separation and geometry of the surfaces. The relationship between molecular and macroscale phenomena becomes more complex when we must consider both molecular and continuum behavior, as is the case for polymers adhesives. There are several compounding factors at play: more diverse and complex chemical interactions, deformation of each individual polymer at the interface, and time-dependent polymer relaxation and bond formation processes.

2.2.1 Interfacial chemistry

Many adhesives are capable of interactions beyond van der Waals forces, which can significantly increase their overall adhesion.[18] Hydrogen bonding interactions are common, although examples of covalent bonds and electrostatic interactions exist.[30, 48] Each of these intermolecular interactions are stronger than dispersive interactions, but require specific opposing chemistries in order to form a bond.[18, 21] A simplistic method of accounting for additional intermolecular interactions is to lump the interactions together into the surface energy of the material, which can be probed through contact angle goniometry.[34] While adhesion is clearly related to the surface energy of the material, as predicted by **Eqn. 2.2**, in practice this relationship is more qualitative than quantitative.[8, 49] Aside from effects of fracture mechanics and surface roughness, a major consideration is that the strength of these bonds is dependent on their environment and the opposing chemistry – a hydrogen bond will not form with a polyolefin, but could interact with the aromatic ring in polystyrene.[50, 51] This can be partially addressed by splitting the surface tension terms in **Eqn. 2.2** into the dispersive and polar (H-bonding) portions:[52]

$$W \approx 2\sqrt{\gamma_a^d \gamma_s^d} + 2\sqrt{\gamma_a^p \gamma_s^p}, \tag{2.13}$$

where γ^d and γ^p are the dispersive and polar contributions to the surface energy, respectively. Although both the assumptions in **Eqn. 2.13**, that dispersive and polar contributions to surface energy can be separated and that the whole interaction energy can be estimated through a geometric mean, are incorrect, this approach captures general trends in adhesive behavior for polar and non-polar materials.[29]

Further complications arise in the fact that adhesive bonds are not static and have a finite rate of self-dissociation.[53] Each bond exists within a potential well, and to dissociate must pass through energetically unfavorable transition state with an associated barrier height referred to as the activation energy E_a.[54] At any given time, the thermal energy of molecules could be sufficient for the bond to dissociate.[45] The Eyring equation relates E_a to the average lifetime of the bond τ, showing that the probability of thermal dissociation decreases dramatically with increased bond strength.[55]

$$\tau = \frac{h}{k_B T} \exp\left(\frac{E_a}{k_B T}\right), \tag{2.14}$$

where h is Planck's constant, k_B is Boltzmann's constant, and T is the temperature. As a consequence of the thermal dissociation of bonds, the timescale over which debonding occurs influences the number of bonds participating in the adhesive interaction.[56] For slow debonding, thermal dissociation leads to an equilibrium number of bound molecules at the interface, while if an adhesive is rapidly debonded more bonds will remain bound to increase the overall adhesive interaction.

It is commonly recognized that transition state theory, and consequently **Eqn. 2.14**, can significantly overestimate the attempt frequency for dissociation of a bond by assuming thermal equilibrium between the ground and transition states.[56] Instead, Kramer's theory models the dissociation as a friction-driven diffusive process, which has proven to be more accurate.[54, 55] Through this, the lifetime can be estimated through[55]

$$\tau = \frac{l_c l_{ts}}{D} \exp\left(\frac{E_a}{k_B T}\right), \tag{2.15}$$

where l_c, l_{ts}, and D are bond-dependent constants associated with the width of the energy minimum, the width of the transition state energy barrier, and the molecular damping, respectively.

When a force is applied to the bond, it takes less energy to reach the transition state for dissociation and the activation barrier height is diminished in relation to the strength of the force applied.[53] This effectively decreases the bond lifetime, so the average bond will break more rapidly when a force is applied. This relationship can be expressed by the Bell-Evans model, where the average force to break a bond is logarithmically related to the velocity u at which the bond is stretched:[55]

$$F_{break} = \frac{k_B T}{\lambda} \ln\left(\frac{Mu\lambda\tau}{k_B T}\right), \tag{2.16}$$

where λ is the bond activation length and M is the polymer spring constant. Single molecule force spectroscopy measurements have successfully used **Eqn. 2.16** to estimate τ and E_a for a chemical bond by measuring the bond breaking force at various loading rates.[31, 57] These experiments have also revealed a characteristic onset velocity, defined by the point at which the energy stored in the bond over its average lifetime exceeds thermal energy.

2.2.2 Polymer deformation

For a force to be applied to a bond, the polymer molecule involved in the bond must have the same force acting upon it. Consequently, the polymer will stretch, and energy will be stored in the elastic deformation of the polymer.[58] Lake and Thomas were some of the first to recognize this principle, proposing a model where the polymer acts like a spring and each constituent monomer unit will store an equal amount of energy U_{bond} as the ill-fated bond before rupture.[59] Therefore, the total energy stored in the polymer chain is nU_{bond}, where n is the number of monomer units, and the fracture energy $U_{rupture}$ is given by:[58]

$$U_{rupture} = nU_{bond}. \tag{2.17}$$

Importantly, **Eqn. 2.17** predicts that the fracture energy, or relatedly adhesion, will increase with increasing polymer molecular weight.

However, the stretching of a polymer molecule itself is highly nonlinear. When a polymer is stretched, energy is stored in the bending of bond angles as well as the stretching of the bonds themselves.[60] A common model for polymer stretching is the Freely Jointed Chain model, which treats the polymer as a chain of n rigid segments of length l_k (Kuhn length).[61]

$$\Delta x = L_c\left[\coth\left(\frac{Fl_k}{k_B T}\right) - \frac{k_B T}{Fl_k}\right]. \tag{2.18}$$

Here Δx is the extension of the chain, and L_c is the contour length of the chain ($L_c = nl_k$). **Eqn. 2.18** works well for small, entropic deformations, but at large strain the bonds themselves will deform.[62] To account for segment deformation, one can use the modified Freely Jointed Chain model, where each segment is treated as an elastic spring of spring constant $K_{segment}$. This yields the equation:[63]

$$\Delta x = \left[\coth\left(\frac{Fl_k}{k_B T}\right) - \frac{k_B T}{Fl_k}\right]\left(L_c + \frac{nF}{K_{segment}}\right), \tag{2.19}$$

which more accurately models the enthalpic deformation of polymers.[62] More recent progress has seen the development of models that directly describe bond stretching and bending potentials, providing a more detailed picture of polymer deformation.[64]

2.2.3 Multiscale adhesion models

Contact mechanics models can relate experimentally measured parameters (force, crack length, contact area) to the energy release rate of a material. **Sections 2.2.1** and **2.2.2** presented models for the strength of individual molecular bonds and individual polymer deformation. The challenge now lies in connecting phenomena across these two length scales and finding methods of calculating a continuum energy release rate from discrete molecular forces. An early method, proposed by Griffith in 1921, estimated the fracture energy of glass by dividing the molecular bonding energy (covalent bond strength) by the area occupied by each atom, giving an effective surface energy of the crack.[65] As noted by Griffith, this approximation neglects the fact that bonding energy is function of separation, and assumes that all molecules are participating in bonding. Lake and Thomas made a similar argument in 1967, extending Griffith's approach to a polymer system with N polymer chains per unit volume, that each fracture at energy nU_{bond} according to **Eqn. 2.17**.[59] By estimating the number of chains that are active across the fracture plane as $\Sigma = \frac{1}{2}NL$, where L is the average end-to-end distance of the polymer chain, one obtains:[58]

$$G_{fracture} = \Sigma n U_{bond}. \tag{2.20}$$

This relationship has been validated numerous times in literature,[56, 58, 66, 67] although since Σ itself is related to n the scaling is suggested be closer to $G_{fracture} \propto \sqrt{n}$.[68, 69] While Lake-Thomas theory (**Eqn. 2.20**) was originally devised for cohesive fracture through the bulk of a polymer, its principles can be generalized for an adhesive interface, although $G_{fracture} \not\equiv G$ due to the influence of the opposing material at the interface in G. However, at an adhesive interface it is often difficult to know Σ, especially when dealing with dynamic interactions, limiting the ability to estimate G *a priori* from **Eqn. 2.20** without further knowledge of the surface bond density.

Another important feature of adhesion measurements is that adhesion is often shown to increase with the velocity at which testing occurs.[56, 70, 71] At higher velocities (> 1 $\mu\text{m/s}$), this can often be attributed to viscoelastic effects,[72] but the amplification of adhesion with velocity occurs even at extremely slow velocities of around 1 nm/s or in cases where viscoelasticity cannot explain the observed phenomena.[25] Schallamach noted this fact in 1953 through the study of the temperature dependence of sliding friction velocity, and inferred that the breaking of adhesive bonds occurs through an activated process, such as that described in **Eqn. 2.14**.[73] In contrast to a static bond model that only depends on the distance between the two molecules, the activated bond failure process leads to an average bond rupture force that increases with velocity (Bell-Evans theory, **Eqn. 2.16**),[55] and consequently at higher velocities more bonds will participate in the adhesive interaction at any given time.[25]

To take this into account, Chaudhury estimated the average survival time, $\bar{t}$, of each bond as a function of loading rate Mu:[69]

$$\bar{t} = \left(\frac{k_B T}{Mu\lambda}\right) \ln\left(\frac{Mu\lambda\tau}{k_B T}\right). \tag{2.21}$$

By then calculating the average energy required to break each bond ($U = \frac{1}{2}M(u\bar{t})^2$) and multiplying by the number of bonds per unit area (Σ) one obtains:[56, 69]

$$G = \left(\frac{\Sigma}{2M}\right)\left[\left(\frac{k_B T}{\lambda}\right) \ln\left(\frac{Mu\lambda\tau}{k_B T}\right)\right]^2. \tag{2.22}$$

Eqn. 2.22 provides an explicit and experimentally useful method of relating strain energy release rate as a function of testing velocity to the bond lifetime (and therefore activation energy) and density of bonds, and the scaling predicted by **Eqn. 2.22** has been experimentally validated with a variety of chemistries and measurement schemes.[48, 69, 74] However, the use of a Hookean polymer spring constant complicates the use of this model, as the unphysical constant value precludes estimation from known polymer stretching models and M must therefore be fitted from experimental data to obtain the highest accuracy in the other fitted parameter. Attempts to include more realistic polymers stretching models yield equations without discrete solutions,[25] and have yet to be widely adopted.

Further attempts to address this shortcoming have been aided by simulations and finite element analysis, where systems of equations incorporating widely accepted models for chemical bond, polymer chain, and elastic body deformation can be solved to track adhesive failure.[45, 75, 76] Of note is the work by Yang, Huang, and Liechti, who combined a Lennard-Jones potential of chemical bond stretching, modified Freely-Jointed Chain model for polymer chain deformation, and nonlinear model for the distortion of the energy barrier by applied force to track damage evolution at an epoxy/silica interface and relate it to experimental measurements.[24, 77] The predictions of Yang *et al.* are broadly similar to those of **Eqn. 2.22**.

2.2.4 Complicating factors

2.2.4.1 Surface roughness

Surface roughness is a hidden factor in every adhesion measurement.[8] Most adhesive interactions rely upon intimate contact to form any attraction, and thus any change to contact area will affect adhesive strength.[34] Model surfaces are generally assumed to be perfectly smooth, thus leading to molecular contact at every point within the contact region. Surface roughness alters this – changing the true contact area from the macroscopically apparent area.[23] For hard surfaces, roughness will often decrease the contact area, resulting in lower adhesion than expected (**Fig 2.4, top**).[34] However, soft surfaces (or adhesives applied as liquids) can fill in the gaps created by asperities, leading to an increase in true contact area as shown in **Fig 2.4, bottom**.[8]

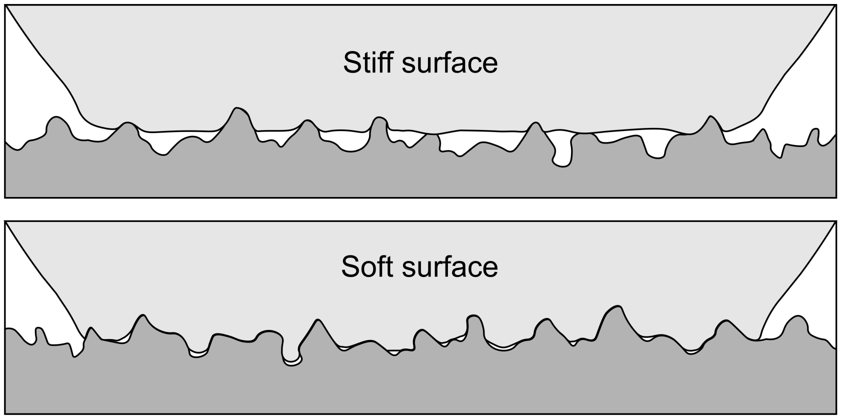

Figure 2.4 Effect of roughness on contact area. Schematic demonstrating how roughness can alter the true contact area between stiff (top) and soft (bottom) surfaces. Roughness will tend to decrease the contact area between stiff surfaces, but increase the true contact area for soft surfaces.

For wetting equilibria, the effect of roughness on the apparent (macroscopic) contact angle of a liquid on a rough solid surface can be accounted for through the use of the Wenzel equation:[28]

$$\left(1 + \cos\theta_{apparent}\right) = \phi(1 + \cos\theta_{true}), \tag{2.23}$$

where $\theta_{apparent}$ and θ_{true} are the macroscale and microscale contact angles, respectively, and ϕ is the ratio between the true and the apparent contact areas. The contact angle θ itself can be related to the surface energy of the liquid (γ_l) and solid (γ_s) through the Young equation:[28]

$$\gamma_{sl} + \gamma_l\cos\theta = \gamma_s, \tag{2.24}$$

where γ_{sl} is the interaction energy between the solid and liquid phases. While the Wenzel and Young equations are useful in considering the effect of roughness,[8] it is difficult to measure the true contact area of each sample. Attempts have been made to quantify the roughness factors ϕ for common substrates, but they're naturally highly sensitive to the exact preparation of the specimen.[78]

More elegant attempts to quantify the effects of roughness have come by attempting to ascertain the true contact area by modeling asperities on the surface.[79] Notably, the groups of Robbins and Persson leveraged the idea that many surfaces exhibit roughness in a self-affine manner over several length scales to predict a load-indentation relationship that accounts for surface roughness. [80, 81] Through this, the applied force was found to scale exponentially with indentation depth $F \propto \exp\left(\frac{\delta}{\delta_0}\right)$, where δ_0 is a reference length on the order of the surface roughness.[34, 82]

Due to the complications inherent in accounting for surface roughness, it's generally considered prudent to control surface roughness when measuring adhesion to reduce variability. This can be done by either deliberately roughening the samples through sanding or chemical treatment,[78, 83] or by fabricating samples to minimize roughness.[26] Minimizing surface roughness is particularly crucial when trying to measure short-range molecular interactions or relate molecular interactions to macroscopic forces, as roughness can alter or obscure the molecular forces one is trying to examine.[51, 84] Furthermore, multiscale adhesion models do not currently account for surface roughness effects, and so minimizing surface roughness is a crucial step towards validating those models.[85]

Surface roughness is often characterized through rms (root-mean-square) average deviation value over a line profile, essentially giving the average peak and valley height over the profile. The gold standard for low-roughness surfaces is muscovite mica, which cleaves into atomically flat surfaces of < 0.1 nm rms roughness, but is chemically inert.[86, 87] Graphene can also naturally present an ultraflat surface, with films reported with roughness as low as 0.19 nm rms.[84] Mechanical polishing and annealing can produce silicon wafers with roughness nearing 0.5 nm rms over macroscale areas.[88] Polymer films can be readily spincoated to 0.2 – 1 nm rms roughness, with optimized coating conditions on a flat substrate.[27] Metallic films are routinely evaporated to give rms roughness values of 0.6 – 1.8 nm, but recent advancements in the technique of template stripping have enabled the production of metallic films down to 0.2 nm rms.[89, 90] The template stripping technique will be discussed at length in **Chapter 3**.

2.2.4.2 Viscoelasticity

Polymers are dynamic molecules – relaxations are frequently observed for polymeric materials, leading to time-dependent changes in adhesion. Viscoelasticity is by far the most well-studied. Viscoelastic dissipation arises from viscous fluid-like flow over long time scales, which causes energy loss during loading and unloading of the material.[91] Viscoelasticity is commonly modeled by the empirical equation:[32, 92]

$$\mathrm{G} = \mathrm{G}_0\left(1 + \left(\frac{v}{v^*}\right)^n\right). \qquad (2.25)$$

Here v^* and n are empirical parameters describing the intrinsic velocity due to material relaxation and the scaling constant, respectively. Viscoelastic effects tend to amplify the adhesion of a system, leading to much higher adhesion than would be expected from surface effects alone.[72, 93] Given that viscoelasticity leads to an increase in adhesion with testing velocity, it can easily convolute effects driven by activated bond rupture at an interface. It can help to disentangle these separate phenomena by measuring at slower speeds (< 1μm/s) where viscoelasticity is small.[72] Viscoelastic dissipation can be minimized by using thin films and stiff materials, reducing the amount the material can stretch overall.[70, 93]

2.2.4.3 Poroelasticity

Time dependent changes in adhesion can also arise from fluid flow into or out of a material, known as poroelasticity.[94, 95] Many polymers absorb some amount of fluid when submerged, which causes them to expand and swell in relation to the amount of absorbed fluid. When a force compresses the swollen material, the fluid is pushed out of the compressed region. However, the confined pores the fluid must travel through slows down the fluid's movement, leading to a resistance to drainage that dissipates over time.[96] For thin polymers this resistance can be modeled by assuming a Hertzian relationship between contact radius a and indentation depth δ:[95]

$$F = \frac{\pi}{8H}\left(E^*\left(8\delta a^2 - \frac{a^4}{R}\right) + \frac{\dot{\delta}\eta a^4}{\kappa}\right). \tag{2.26}$$

Here $\dot{\delta} \equiv \frac{d\delta}{dt}$ is the indentation rate, H is the film thickness, η is the dynamic viscosity of the solvent, and κ is the permeability of the film. **Eqn. 2.26** can be broken up into two terms, where the former represents the elastic contribution to the force and the latter is the contribution due to fluid flow. This model has been validated for the indentation (compression) of thin hydrogels,[95, 97] but a similar phenomenon exists during adhesion, where a suction-like force is generated when fluid returns to the dehydrated region as the samples are put under tension.[96] While only a handful of studies have probed the relationship between poroelasticity and adhesion,[96, 98-100] logically the adhesive force due to fluid infusion could be (simplistically) modeled by inverting the sign on the second term in **Eqn. 2.26**:[27]

$$F_{fluid\ infusion} = -\frac{\pi}{8H}\left(\frac{\dot{\delta}\eta a^4}{\kappa}\right), \tag{2.27}$$

where a negative force indicates adhesion (tension). **Eqn. 2.27** predicts that poroelastic suction forces would increase with retraction velocity but would decrease sharply as contact area approaches zero, which can help distinguish it from other time-dependent effects.

2.2.4.4 Contact aging

Contact aging refers to the improvement in solid-solid adhesion that occurs as surfaces are left in contact for longer periods. The adhesive strength of soft materials is often observed to increase with contact (dwell) time.[101] While there is still debate over the mechanisms involved, it is often believed to occur through rearrangement of the polymer molecules near the interface to improve the contact area and chemical interactions that are formed.[102-104] Contact aging is challenging to study mechanistically, since it is difficult to observe what occurs in a buried interface. It is well-known that contact aging can be related to the molecular mobility of the material,[102] and contact aging is usually modeled as a power-law dependence of adhesive strength with time, where the fitted exponent can be compared to other systems for insight.[96, 105] A related phenomenon involves diffusion of polymer chains across a polymer-polymer interface,[101] but is beyond the scope of this thesis.

3 Template-Stripped Ultra-Smooth Aluminum Films (0.2 nm RMS) for the Surface Forces Apparatus [‡]

3.1 Abstract

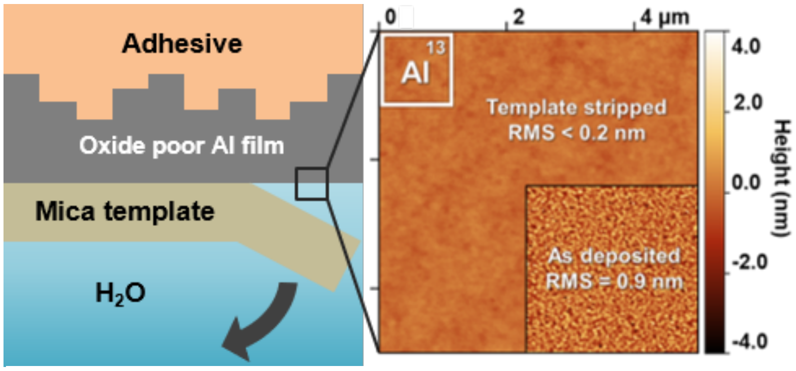

Figure 3.1. **Schematic depicting a summary of Chapter 3**: Peeling of evaporated aluminum film from mica in water reveals an ultra-smooth surface. Right: Atomic Force Microscopy images of template-stripped and as-evaporated (inset) films.

We present a method for the fabrication of ultra-smooth (0.2 nm RMS), aluminum substrates through template stripping (TS). The method relies on the use of mica as a template in combination with thermal evaporation of Al at high (> 10 nm/s) rates under vacuum (≤ 1×10^{-7} Torr). As a reactive metal, Al is usually not considered a viable option for TS off oxide templates. However, under these conditions the adhesion between the Al film and mica is poor, enabling the removal of the template without any mica residue. We verify the absence of mica using atomic force microscopy, X-ray photoelectron spectroscopy, and contact angle measurements. We establish the suitability of these films for surface forces measurements. The multiple bean interferometry in transmission yields high quality fringes allowing for the measurement of force-distance curves. The adhesion the films to mica is significantly higher than the adhesion of thermally evaporated Al (0.9 nm RMS). Preliminary results suggest that the TS-Al surface display higher corrosion resistance. The fabrication method will enable important experiments on this widely used material.

[‡] This chapter was previously published as "van Engers, C. D.; Lamberty, Z. D.; McGuiggan, P. M.; Frechette, J., Template-Stripped Ultra-Smooth Aluminum Films (0.2 nm RMS) for the Surface Forces Apparatus. *Langmuir* **2021**, *37*, 6556-6565" and is adapted with permission from all co-authors.

3.2 Introduction

Muscovite mica has been widely used to study surface forces at the solid-liquid/solid-air interface due to its atomically smooth surface.[87] Mica, however, sees limited use in real-world applications, and it is therefore important to extend the number of substrates viable for roughness-sensitive surface forces studies. A range of alternative systems have been investigated, including Au, Pt, Fe, SiO_2 and SiN_x.[89, 106-111] For example, Au has been used as a conductive substrate to study charging dynamics of nanopores.[112] Here, we address the ongoing need for ultra-smooth, contamination-free aluminum for surface forces measurements.

Measurements of adhesion, friction, and other surface forces such as structural forces in liquids can be obscured by surface roughness, particularly when surface features are close in size to the length scale of the interactions of interest.[85, 113-116] For example, adhesive interactions may be completely negated by surface topography, hampering correct interpretation of adhesion or surface energies of different materials.[113, 117] Fabricating sufficiently smooth substrates to perform such measurements becomes particularly challenging when the roughness features required approach the molecular limit (~ 0.28 nm, the diameter of a water molecule).[28]

Template stripping has been widely used to fabricate ultra-smooth substrates with sub-nm RMS (root mean square)-roughness, and has enabled surface forces studies on conducting substrates.[118] For example, Au surfaces with an RMS roughness of 0.2 nm (10 x 10 μm^2) have been fabricated through template stripping after thermal evaporation of Au at low rate (0.01 nm/s) on a heated mica substrate (100 – 150 °C, 4 x 10^{-6} torr).[119] Such low RMS roughness values enabled surface forces measurements, such as first the direct measurement of confinement induced charge inversion between a dielectric and a conductor.[120]

Aluminum (Al) is one of the most widely-used metals, finding uses in transportation, construction, packaging, and in many every-day house-hold items and electronics, with an estimated global production of 60 million metric tons in 2018.[121] Al substrates with sub-nm roughness (down to 0.6 nm RMS) have been developed through direct physical vapor deposition techniques, however RMS roughness values on the order of molecular dimensions have yet to be achieved.[122-125] The combination of state-of-the-art deposition techniques with template stripping could yield substrates with roughness on the order of the size of small molecules, suitable for surface forces measurements.

Template stripping is a multi-step process involving: (1) the deposition of a metal on a smooth template, (2) the application of an adhesive backing layer to the exposed side of the metal surface, and (3) the removal of the metal from the template (see illustration in **Figure 3.2**). The success of template stripping relies on a balance between poor adhesion and good wetting of the metal to the substrate, and has thus been mostly used to fabricate noble metal surfaces (Ag, Au), using oxide substrates (mica, Si/SiO_2), since noble metals adhere poorly to the commonly used oxide substrates.[89] Recently, McPeak *et al.* reported template stripping of Al from native-oxide covered Si(100), resulting in films with RMS roughness down to 0.6 nm, using high evaporation rates (15 nm/s) at low pressure ($\leq$ 1 x 10^{-6} torr).[126] They hypothesized that the use of high rates during evaporation creates a dense Al-plume that depletes reactive gas-phase oxide species (mainly H_2O) in the chamber. As a result, the metallic Al-film exhibits greatly reduced adhesion to the oxide substrate and can be template-stripped.

Because it is smoother, mica is often preferred over native-oxide-covered silicon for preparing smooth thin films via template stripping. Mica has a layered structure with strong, covalent in-plane bonds, while inter-plane interactions are governed by van der Waals forces.[87] The structure allows cleavage of atomically smooth samples that are monocrystalline over large (> 1 cm^2) areas. However, due to its cleavable nature, Rossetti *et al.* found that flakes of mica remain on the surface when template stripping titanium from mica substrates.[127] The presence of mica residue would greatly hamper any surface forces measurements and it is therefore important to ensure all of the mica template is removed.

Here we present a method to fabricate ultra-smooth (~ 0.2 nm RMS) Al thin films through template stripping from a mica substrate. The method is suitable for highly sensitive surfaces force measurements with techniques such as the surface forces apparatus (SFA) or colloid probe atomic force microscope (CP-AFM). The fabrication method relies on the use of freshly cleaved, single crystal mica in combination with thermal evaporation of the Al at a high rate ($\geq$ 10 nm/s) under high vacuum ($\leq 1 \times 10^{-7}$ torr). The use of mica as an atomically smooth template allows for the fabrication of a featureless Al surface, whilst the high evaporation rates ensure complete removal of the mica (see **Figure 3.2**). We also studied the aluminum films directly deposited on mica via thermal evaporation (R-Al). Measurements on the exposed Al side served as a point for comparison and control experiments for the template stripped Al (TS-Al) surfaces.

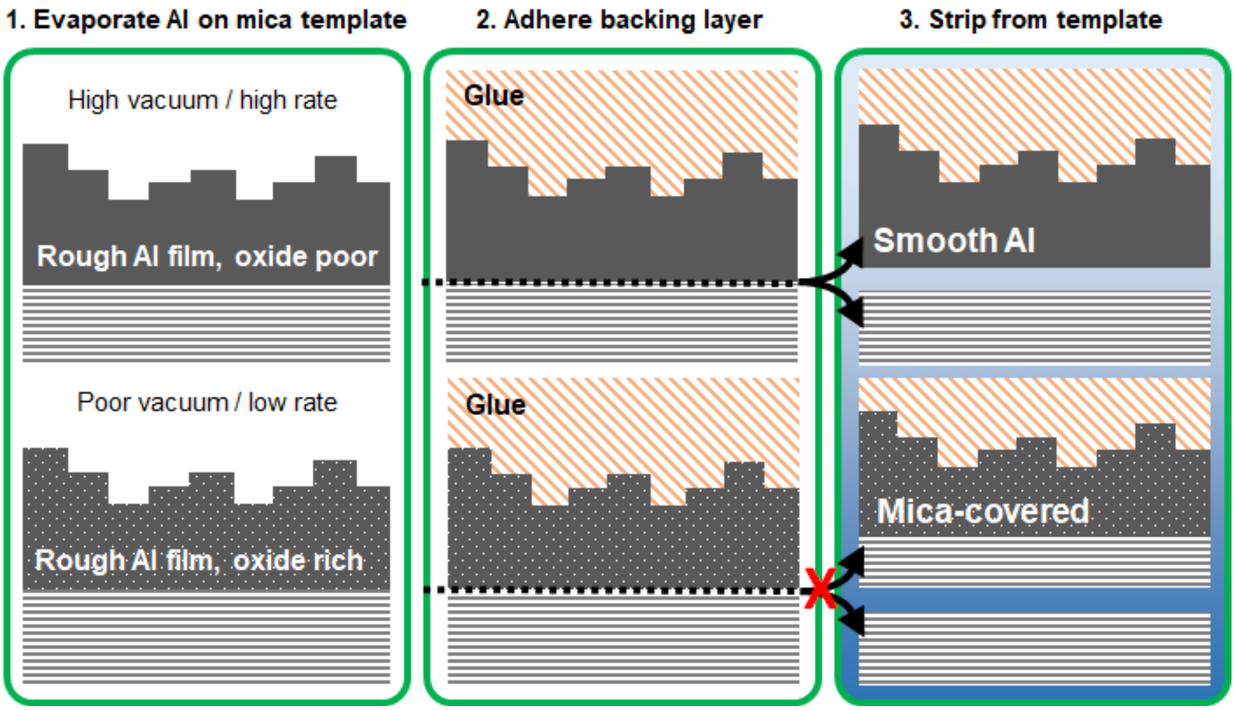

Figure 3.2. Workflow for template stripping. (1) Al is evaporated onto freshly cleaved mica templates. (2) The Al|mica stack is removed from the evaporation chamber and glued down onto a substrate. (3) The mica is peeled from the Al|glue|substrate stack under water, revealing a smooth surface. Bottom: when the pressure during evaporation is high/the rate is low, the Al film adheres strongly to the mica surface, shifting the cleavage plane away from the Al|mica interface.

We use tapping mode AFM to characterize the Al surfaces. The template-stripped side of the film (TS-Al) has an RMS roughness of 0.2 nm (over 2 x 2 μm^2 and 5 x 5 μm^2), approaching molecular dimensions, whereas the opposite as-deposited "rough" side (R-Al) has an RMS roughness of 0.9 nm over the same area. We use X-ray photoelectron spectroscopy (XPS) and contact angle measurements to show that no mica remains on the surface of the template-stripped Al samples and provide an *in situ* optical validation method for determining the same. In addition, we validate the use of our Al films for surface forces measurements with the SFA. We show that the films are of sufficient optical quality such that the fringes of equal chromatic order (FECO) in the SFA can be analyzed using state-of-the-art 4x4 optical transfer matrixes and we rely on the FECO to measure force-distance curves in a salt solution. Finally, we use adhesion measurements (vs mica) and preliminary corrosion measurements in aqueous 5 mM NaCl solution to highlight the quality of our template stripped films (TS-Al) compared to as-deposited ones (R-Al).

3.3 Experimental Methods

3.3.1 Materials

HNO_3 (68%, BDH), ethanol (200 proof, Pharmco), H_2O_2 (30%, Fisher), H_2SO_4 (95.0%, J. T. Baker), phenyl phosphonic acid (PPA, 98%, Sigma Aldrich), NaCl (99.0%, Fisher), muscovite mica (Ruby, ASTM V-1/V-2, S&J Trading), and EPON Resin 1004F (Miller-Stephenson) were purchased and used as is. For evaporation materials, we use Al pellets (99.999%, Kurt J. Lesker), Cr plated Tungsten rods (99.9%, Kurt J. Lesker), and Ag shot (99.999%, Alfa Aesar) as received. We use tungsten (W) evaporation boats (0.015” and 0.010” deep, Kurt J. Kesker) for Al and Ag, respectively.

3.3.2 Sample Preparation

We use a Kurt J. Lesker Nano 38 resistive heating thermal evaporator, equipped in its standard configuration with a quartz crystal microbalance (QCM, 6 MHz Cr/Au, Inficon) for measuring evaporation rate and film thickness. We prepare samples in a low-particulate environment (ESCO laminar flow cabinet, ISO Class 4 cleanroom environment). Unless noted otherwise tools and glassware are cleaned using the following protocols. Tools (stainless steel) are treated with $CHCl_3$, IPA, and nitric acid (1:10 HNO_3:H_2O). Glassware is cleaned by immersion in piranha solution (1:3 = H_2O_2:H_2SO_4).

3.3.3 Thermal Evaporation

We prepare template stripped Al (TS-Al) samples on hemi-cylindrical quartz lenses (diameter ~ 10 mm, radius of curvature 10 mm – 25 mm), following the general template stripping scheme laid out by Chai and Klein.[119] First, we cleaved mica until thin (3 – 6 μm), monocrystalline sheets are obtained.[128] We kept the time between cleaving the first mica sheet and loading the sheet-covered base plate into the evaporation chamber as short as possible, usually ~ 45 minutes. Al is evaporated (using a new boat for each evaporation) at a base pressure of $\leq 1 \times 10^{-7}$ torr, evaporation rate of $\geq$ 13 nm/s under continuous rotation of the substrate holder at ~ 40 rpm. Typically, a layer of 30 – 45 nm Al is evaporated by quickly opening/closing the shutter. Note that upon exposure to the lab atmosphere, a thin layer of amorphous Al_2O_3 immediately forms on the exposed surface due to its reactivity with O_2. The TS-Al and R-Al originate from the same batch, that is an Al-covered mica substrate is either used as-is Al-side up (R-Al) or glued Al-side down and stripped (TS-Al). Ag was evaporated at a base pressure of $\leq 1 \times 10^{-7}$ torr, evaporation rate of $\sim 2 - 4$ nm/s under continuous rotation of the substrate holder at ~ 40 rpm.

3.3.4 Imaging

AFM data was recorded using a Bruker Dimension 3100 atomic force microscope (Bruker Nano, Santa Barbara, CA) in tapping mode and analyzed using Gwyddion 2.52.[129] For processing the AFM data we align the line profiles using a 1st degree polynomial (linear slope) and subtract the background using a 3rd degree polynomial for both the x and y directions.

3.3.5 X-ray photoelectron spectroscopy (XPS)

XPS data were obtained using a PHI 5600 instrument equipped with a Mg Kα flood source (1253.6 eV). Scans were taken at a source power of 300 W, with a pass energy of 23.5 eV, and 0.025 eV/step. Spectra were deconvoluted using commercial software (CASA XPS) and processed using a Shirley background. The binding energies for the Al(2p) and Si(2p) peaks were calibrated by aligning the C(1s) peak to 284.8 eV.

3.3.6 Contact angle measurements

Contact angle measurements were performed using a FTA125 goniometer (First Ten Angstroms) using 2 μL sessile drop of water. Contact angles on mica- and on Al-covered quartz lenses were measured before and after functionalization with phenyl phosphonic acid (PPA). The surfaces were functionalized through immersion in 1 mM aqueous PPA solution overnight, followed by rinsing with water and drying in a stream of N_2.

3.3.7 TS-Al (Template stripping of Al)

To fabricate the template stripped samples (TS-Al), we remove the Al-covered mica sheets from the base plate and glue them onto hemi-cylindrical quartz lenses using a thermoplastic resin, EPON 1004-F at ~ 180 °C. After reaching room temperature, we immerse the sample in water in a glass petri-dish. Water facilitates the removal of hydrophilic substrates during template stripping.[84] After peeling off the mica template we observe the temporary appearance of an opaque haze on the Al surface. The samples are removed from the dish and carefully dried under a steam of N_2. Finally, the samples are heated on a hotplate at 90 °C for 10 minutes to remove surface-bound water and grow the native oxide.

3.3.8 Rough Al surfaces (R-Al)

We prepare the R-Al samples by gluing an Al-coated mica sheet onto a hemi-cylindrical lens using EPON 1004-F so that the Al-side faces upward. We performed adhesion and corrosion measurements between a mica-coated sample and either an TS-Al-coated sample or an Al sample exposing the as-deposited ("rough") side of the Al film (R-Al).

3.3.9 SFA measurements.

We use an SFA 2000 (SurForce LLC) equipped with a CCD camera (Andor Zyla 5.5 sCMOS),[130] using a spring constant of 2076 ± 33 Nm^{-1}. We analyze the interference data using home-written code based on both Heuberger's and Schwenzfeier's methods.[131, 132] The latter uses 4x4 optical transfer matrixes and incorporates the birefringence, absorbance, and thickness of films (*e.g.* metals) within the interferometer. For an experiment using TS-Al and mica, the interferometer consists of: [*Glue* | Al | medium | mica | Ag | *Glue*] and for the R-Al and mica experiment, the interferometer consists of: [*Glue* | mica | Al | medium | mica | Ag | *Glue*]. Here the italic notation denotes the semi-infinite layers and the medium is either water, air or is omitted when in contact. In all experiments, the thickness of the Al layer were 30 – 45 nm. The fringe number and spacing is largely determined by the optical thickness of the mica, whereas the fringe shape is determined by the complex refractive index and thickness of the metal layers. For optical dispersions of the metal layers we used the values reported by Rakic *et al.*.[133] For the mica we used the value reported by Kienle *et al.*[134]

For adhesion experiments we followed the procedures by Christenson.[86] We employed JKR contact mechanics using $W_{adh} = 2F_{adh}/3\pi R_{eff}$ to obtain the work of adhesion.[40] F_{adh} is the pull-off force, and $R_{eff} = (R_1R_2)^{1/2}$ is the effective radius of curvature for which R_i is the radius at the surface of each of the lens assemblies at the contact spot and is measured *in situ* from the FECO with the surfaces out of contact. We repeated the adhesion measurement three times per contact spot and probed multiple spots. We did not control for thickness of the EPON 1004-F layer supporting the Al, which may affect the governing contact mechanics.[135]

Surface forces between TS-Al and mica surfaces were measured in a ~2 mM aqueous LiCl solution. 40 μL of the solution was injected while the surfaces were in contact to form a large droplet between the surfaces. The surfaces were then separated and left to equilibrate for 1 hour before any measurements. Surfaces forces were measured quasi-statically using a micrometer motor. Typically, five FECO images were taken prior to the next motor step and averaged for analysis. Forces are calculated by multiplying the difference between the measured displacement and the motor displacement by the cantilever spring constant. The same protocol was followed for separate surface forces measurements between two mica surfaces in the same salt solution to determine the mica surface potential.

Corrosion measurements were performed as follows. First, the SFA chamber was purged with dry N_2 for 1 hour. Next, the surfaces were brought into contact and the (compressive) force was increased to ~5 mN. Subsequently, the N_2 source was closed, and 35 μL of 5 mM aqueous NaCl solution was injected between the surfaces. To reduce evaporation of the NaCl solution, we injected 3 mL water into the bottom of the SFA chamber. We then recorded the interference fringes to monitor the corrosion of the Al film.

Comparison to Derjaguin-Landau-Verwey-Overbeek theory.[136, 137]

We modeled the force-distance curve as a superposition of a long-range repulsion caused by the overlap of the electrical double layer and a short range van der Waals attraction. We followed our prior method for the prediction for the double layer repulsion.[138, 139] Briefly, we solved numerically the non-linear Poisson-Boltzmann equation between flat plates for either the constant charge or constant potential boundary conditions to obtain the pressure in the gap between the surfaces, followed by an integration to obtain the interaction energy at a given separation. The non-retarded van der Waals interaction energy were calculated for flat plates using a Hamaker constant (3.1×10^{-10} J) obtained from the pull-off measurements. The Derjaguin approximation was then used to convert the calculated interactions (electrostatic and van der Waals) between flat plates to the one between crossed-cylinders.[16] In comparing to DLVO theory, the measured forces were fitted for the Debye length and surface potentials.

3.4 Results & Discussion

3.4.1 Surface Characterization

The results from the AFM height measurements demonstrate the reduction in roughness due to the template stripping process (**Figure 3.3**). The RMS roughness of the TS-Al sample is 0.17 nm (measured over 5 x 5 μm^2, with a peak-to-valley distance of 1.44 nm, see **Figure 3.3A**), is much lower than what has been reported previously, and is similar to RMS roughness values reported for template stripped Au employed.[116, 120, 122-125] The RMS roughness of the R-Al samples is higher at 0.91 nm, indicating similar improvement in the decrease in surface roughness to those reported by others (see **Figure 3.3B**).[118] For reference, Levine *et al.* prepared films using a similar method to what we use for R-Al here.[124] They reported 0.8 nm RMS for as-prepared Al films on mica evaporated at high rate (> 10 nm/s). In addition, the AFM height profile for the TS-Al sample shows no indication of the presence of any mica left on the surface, in contrast from reports of Rosetti *et al.* for template stripping of Ti using mica substrates.[127] However, even though we inspected multiple locations on multiple samples, AFM only shows a small area of the entire sample surface (here 5 x 5 μm^2). Further investigation is necessary to assess if mica is

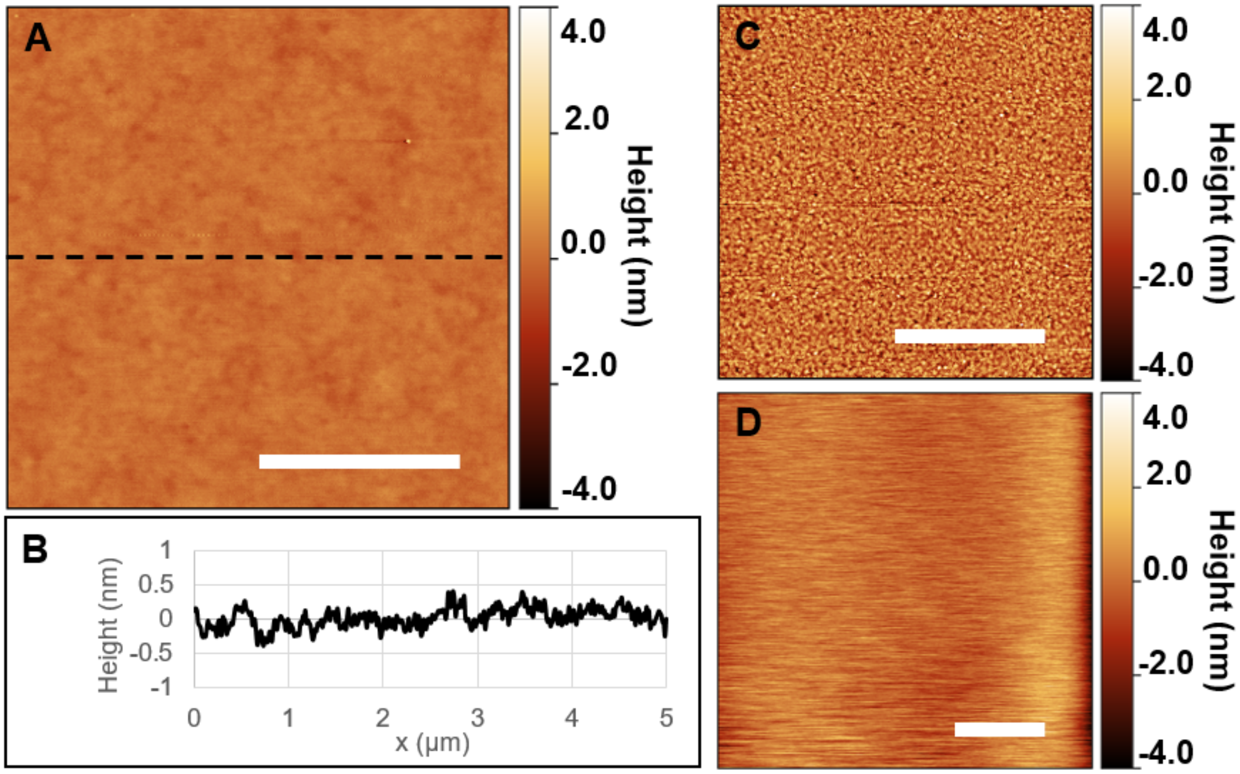

Figure 3.3. AFM height measurement showing the surface profile of the Al surfaces. (A) Template stripped side (TS-Al), RMS = 0.17 nm (5 x 5 μm^2). (B) Line profile of black dashed line in A. (C) As-prepared "rough" side (R-Al), RMS = 0.91 nm (5 x 5 μm^2). (D) Mica reference, where due to the atomically smooth surface of the mica basal plane, the AFM does not pick up any features. Scale bars are all 2 µm.

absent from the TS-Al samples.

XPS of a TS-Al sample also does not show any indication of the presence of mica on the Al surface. We compare the Al(2p) and Si(2p) XPS spectra for both a TS-Al sample (red crosses) and a mica reference (blue dots) in **Figure 3.4**. Muscovite mica is a layered aluminosilicate with the chemical formula $KSi_3Al_3O_{10}(OH)_2$,[87] and thus the mica reference shows a prominent Al(2p) peak corresponding to Al^{3+} at a binding energy of ~ 75 eV and a Si(2p) peak corresponding to Si^{4+} at ~ 103 eV. Using the same scan parameters, we do not detect any Si(2p) signal on the TS-Al sample, confirming the absence of mica. For the TS-Al sample the Al(2p) signal is split into two peaks corresponding to the metallic Al^0 and oxidized Al^{3+} states. This split is expected since exposure of the Al to ambient laboratory air causes the formation of a native oxide layer.

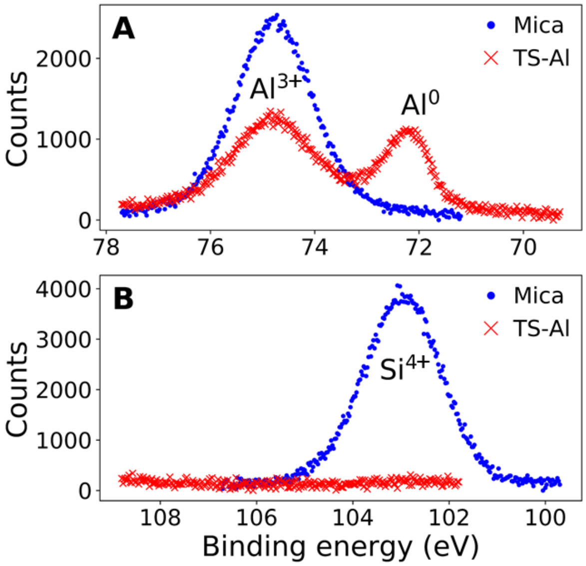

Figure 3.4. XPS spectra of TS-Al (red crosses) and mica reference (blue dots). (A) Spectrum of the Al 2p region, showing the Al^{3+} oxidation state at ~ 75 eV and the Al^0 state at ~ 72 eV. Mica shows only the expected Al^{3+} peak, whereas TS-Al shows the metallic state as well. (B) Spectrum of the Si 2p region. Mica shows the expected Si^{4+} peak, whereas no Si is detected for the template stripped TS-Al sample.

Removing the mica template under water facilitates the template stripping step. Water lowers the interfacial energy at both the mica-medium and Al-medium interfaces. Upon exposure to water the Al surface immediately oxidizes, liberating H_2 gas which is visible as an opaque haze on top of the Al surface. If the adhesion between Al and mica is too high (if the evaporation rate is too low, < 10 nm/s in our experiments), the separation during the underwater template stripping step occurs not at the Al-mica interface, but between two mica crystal planes. In these cases, the resulting samples will be (partially) covered with mica, rather than Al, and no opaque surface haze is observed. Therefore, we suspect that H_2 generation serves as an *in situ* indicator of the successful removal of the mica template. In some cases, we even observe that the generation of H_2 gas generates sufficient pressure to drive the lifting of the mica sheet during template stripping. However, in most cases, we find it necessary to gently lift the edge of the mica template until it separates from the Al. Note that we were also able to remove the mica template in air. However, this resulted in a lower template stripping success rate. Since stripping in water has the added benefit of providing an immediate *in situ* indicator of success, all TS-Al samples were prepared by template stripping in water.

We use surface functionalization with phenyl phosphonic acid (PPA) to confirm that H_2 generation during stripping is an indicator of the presence of a TS-Al film (**Figure 3.4**). Phosphonic acids are known to be stable towards hydrolysis on Al/Al_2O_3, but not on Si/SiO_2.[140, 141] We thus expect PPA to bind to the TS-Al surface but not to the mica. We first measure the contact angle of water on freshly cleaved mica sheets and on solvent-cleaned Al pellets before and after an overnight immersion in 1 mM PPA. We measure a contact angle of < 5° on both samples prior to functionalization. After functionalization, the contact angle on mica remains at < 5°, whilst it increases to 40 – 60° on the Al pellets. On partially stripped TS-Al/mica samples the contact angle is initially < 5° across the entire sample. After functionalization, the areas which showed the haze due to H_2 generation have a contact area of $45 \pm 6°$, whereas on the haze-free areas contact angles remain unchanged (< 5°), see **Figure 3.5**. Selective contact angle modification provides strong evidence for the opaque haze being correlated to oxidation of the Al surface and an *in situ* indicator for successful removal of the mica template.

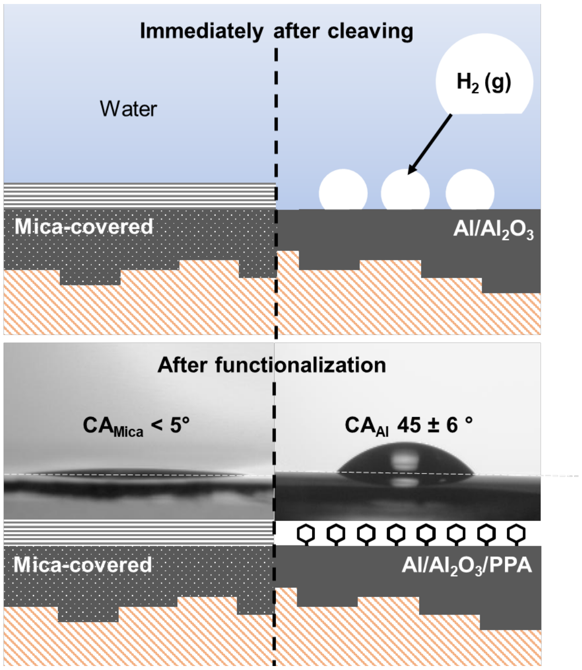

Figure 3.5. Macroscopic *in situ* verification of the presence of TS-Al on the sample surface. (Top) A simple way to determine whether the mica template is successfully removed, is through the observation of bubbles on the surface. H_2 evolution is visible due to the oxidation of the Al upon removal of mica in water. (Bottom) Successful template stripping is confirmed through selective functionalization of Al/Al_2O_3. After overnight immersion in an aqueous solution of 1 mM phenylphosphonic acid (PPA) the contact angle (CA) of water on the template stripped surface has increased due to the formation of a self-assembled monolayer. On the mica-covered Al surface the CA remains < 5°, the same as for both surfaces prior to functionalization (not shown).

Several factors contribute to reducing the adhesion of the Al film to the mica substrate. These are (1) the evaporation rate (≥ 13 nm/s); (2) the time between cleaving of the mica templates and their loading into the evaporator (≤ 45 minutes); (3) the chamber pressure ($< 1 \times 10^{-7}$ torr); (4) the thicknesses of the glue layer and mica template. The latter likely relates to mechanical stresses in the system, whereas the first three factors all relate to the relative amount of impurities - which we expect to be mainly H_2O, O_2, and surface K_2CO_3 (from reaction of K on the mica surface with atmospheric CO_2). In reaction with metallic Al, these impurities likely form metal-oxides, which we believe cause higher adhesion to the mica substrate through interactions between permanent dipoles. In the case of a purely metallic film we expect only dispersion and induced-pole interactions, as is the case when template stripping noble metals using mica as template.

Increasing the evaporation rate reduces the number of impurities in the film by leaving less time for wall-adsorbed species (in equilibrium with gas-phase species) such as O_2 and H_2O to desorb and react with the film. This is a well-known phenomenon known as “gettering”, where the evaporation of a reactive metal causes a significant drop in chamber pressure (we observe this as well). Limiting the time between cleaving the mica substrates and loading these into the chamber similarly reduces the time for airborne species from the laboratory environment to adsorb to the mica. By using at the lowest chamber pressure possible we limit the number of impurities present prior to evaporation.

We therefore recommend low melting point metals (such as Al, Pb, Zn) to be template stripped using this technique, since they can be evaporated at high rates. Au can be evaporated at low rates, since it does not react with chamber impurities. However, even when template stripping Ag, higher evaporation rates have been recommended[126]. For high melting point metals such as Fe, Kurihara's group has shown sputtering directly onto mica can be used to fabricate smooth substrates, likely owing to the small grain sizes obtained at low homologous temperatures (the ratio $T_{substrate}/T_{melt}$)[111, 142].

It is necessary to heat the TS-Al surface after template stripping to prevent corrosion of the samples. Oxidation of the freshly exposed Al surface by water creates a low density oxide layer which renders the Al film labile to corrosion.[143, 144] AFM data recorded on a TS-Al surface that was not heated after template stripping shows many small holes, which we associate with etch pits. The presence of these pits suggests that the surface oxide formed in water does not prevent further detrimental surface oxidation (corrosion). Heating the sample facilitates drying and forms a denser/more stable surface oxide layer absent of etch pits, as shown in **Figure 3.3**. Annealing of the R-Al samples occurs during the gluing step on the lens, we do not observe pits on the R-Al samples (**Figure 3.3**). We note that McPeak *et al.* used UV-Ozone for this purpose after removal of the Si/SiO_2 template in air.[145]

On occasion we observe that after removal from the evaporation chamber our Al films become less reflective and show a corrugated surface. We believe that this is due to de-wetting of the film, caused in part by the poor adhesion of the Al film to the mica and in part by the stress caused by the volume change of the Al-surface upon oxidation due to exposure to the ambient atmosphere. This loss in reflectivity and corrugation is most pronounced for our thinnest ~ 30 nm Al films and occurs slowly over time, prompting us to glue the Al-coated mica sheets on the hemi-cylindrical lenses immediately after removal from the evaporation chamber. Corrugation can be easily prevented by depositing thicker (*e.g.* 100 nm) films or adding thin layer of a noble metal after the Al deposition. Al films showing a corrugated surface were not used for further experiments.

3.4.2 Surface forces measurements

3.4.2.1 Interferometry

In the SFA, the separation between surfaces is calculated from multiple beam interferometry. As a result, high quality FECO that are well-described by theory are usually necessary to acquire and interpret most data with the SFA. In particular, when replacing an Ag mirror with Al the intensity of the FECO decreases. Therefore, in addition to requiring smooth Al films, most experiments with the SFA require a narrow range of Al thicknesses to obtain high quality FECO. Some SFA-studies also require a precise and *in situ* knowledge of the thickness of the TS-Al, for example in corrosion studies.

We first demonstrate that the TS-Al films lead to high quality transmission FECO, that is, FECO with good signal-to-noise ratio that are in good agreement with predictions from 4x4 optical transfer matrixes. The experimental FECO for a TS-Al film are shown in **Figure 3.6A**. We use the 4x4 matrix method to extract the layer thicknesses of the optical stack. **Figure 3.6B** and **3.6C** show the best fit to the interference spectrum at the center point. The birefringence of the mica layer causes splitting of the interference fringes, captured by the model. For the FECO in **Figure 3.6**, the optimal fit for the Al thickness is 41.6 nm. When using the SFA in transmission mode with Al, this thickness represents an upper limit that can be used, the transmitted intensity from thicker films is too low and the data cannot be analyzed. We note that this limitation does not exist for setups in reflection. For the Ag layer we obtain an optimal fit for a thickness of 25 nm, which is 10 nm lower than the thickness reported by the QCM on the thermal evaporator, where the difference may be due to the placement of the sample in the evaporator (sample position with respect to the QCM), oxidation during storage, or gluing. In addition, Schwenzfeier *et al*. report a thickness reduction of the Ag layer of ~20%, likely due to oxidation.[132] The mica is birefringent with a reported birefringence of $\Delta n = 0.0035$-0.0052 and we used 0.0035 for the fit.[146] The mica thickness used in the fit was obtained through separately measuring the thickness of symmetric mica sheets from the same crystal. We did not attempt to model the oxide layer thickness. Overall, the good agreement between the calculation and experimental data shows that the optics of the TS-Al layer are well-described by state-of-the-art optical models for multiple beam interferometry. Therefore, the TS-Al films are suitable even for experiments where the Al thickness needs to be determined *in situ*.

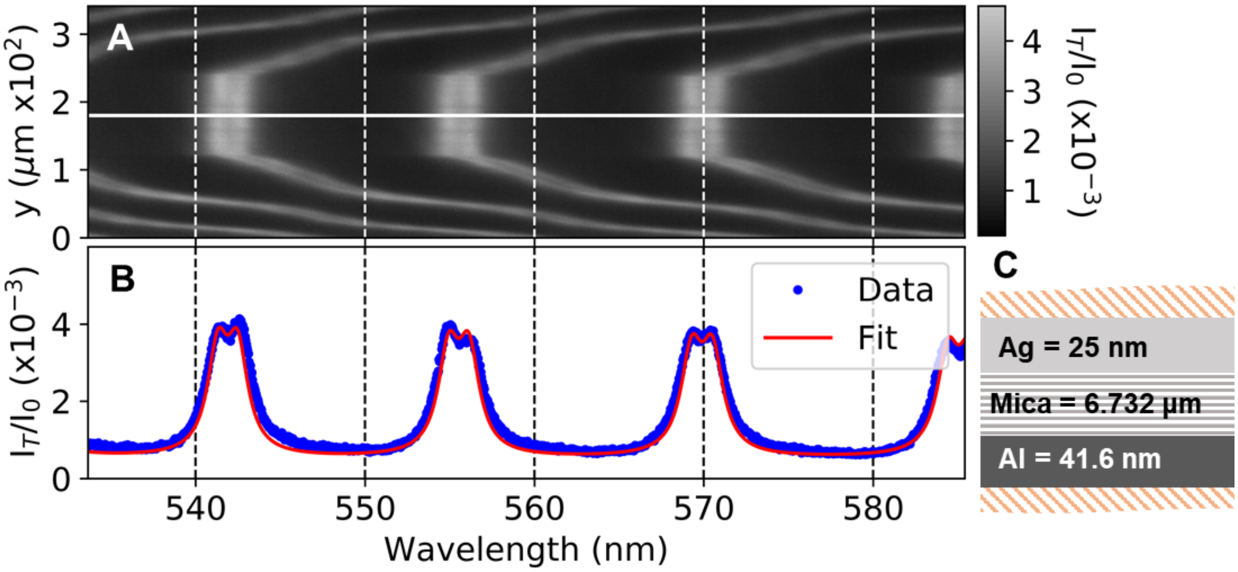

Figure 3.6. Interferometric data recorded in the Surface Forces Apparatus, and results from fitting the interference spectrum. (A) Fringes of equal chromatic order (FECO) resulting from light passing through an interferometric filter consisting of: template stripped Al | mica | Ag. (B) Profile (blue dots) and fit (red line) corresponding to the white line in A. (C) Filter composition corresponding to the fit in B.

3.4.2.2 Force-distance curves.

We measured the interaction between the TS-Al surfaces and mica in 2 mM LiCl to demonstrate that the TS-Al surfaces are suitable for force measurements in the SFA. **Figure 3.7** shows the force as a function of surface separation where multiple experimental curves are overlaid. As expected, we observe a long-range electrostatic repulsion followed by a jump-in instability at a separation of 2 – 3 nm. After jump-in, the FECO shows flattening of the surfaces in the contact region (lower inset of **Figure 3.7**). We compare our measurements to predictions from DLVO theory, as shown as lines in **Figure 3.7**. The measured Debye length of 6.1 nm correspond to a concentration of 2.25 mM LiCl which is in good agreement with our experiments. We obtain a surface potential for the TS-Al of $\psi_{Al} = -90\, mV$ when using a mica surface potential of $\psi_{mica} = -150$ mV obtained from separate mica-mica experiments. For comparison, under similar conditions the surface potential of sapphire surfaces is between $\psi_{saph} = -13$ and -43 mV.[147, 148] The measured potential here is significantly more negative than our values. Reports for the surface potential of alumina surface is also significantly less negative (reaching positive values for alumina particles).[149, 150] It is important to note that our TS-Al films are not sapphire surfaces nor pure alumina. Based on the fit to the predicted FECO intensity (**Figure 3.6**) we suspect that the oxide layer is quite thin and perhaps the metallic nature of the underlying Al surface leads to more negative surface potentials.

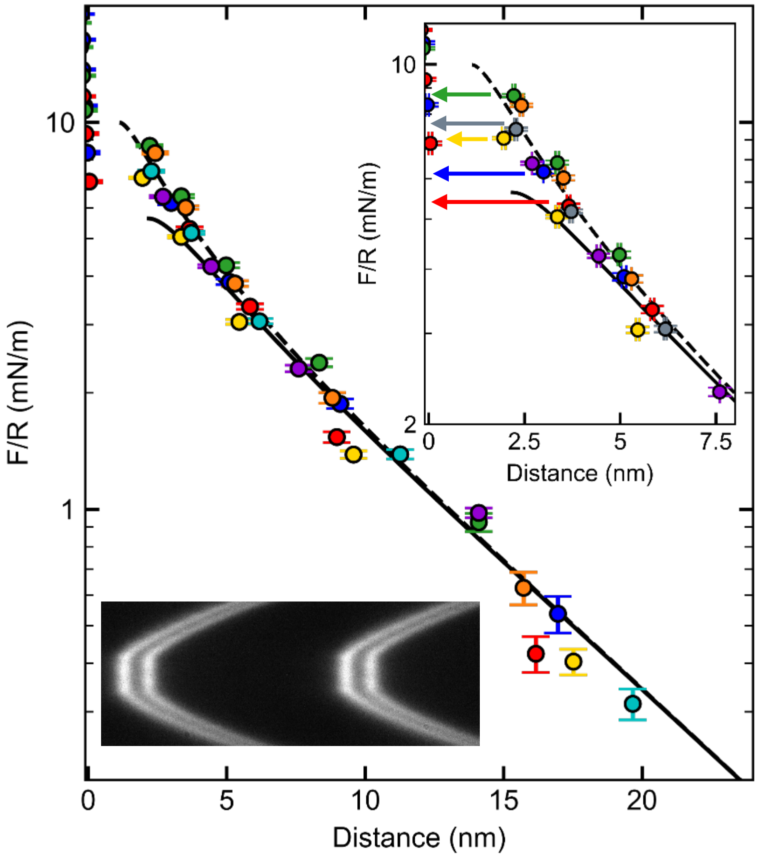

Figure 3.7. **Force vs surface separation measured between TS-Al and mica surfaces.** Black lines show DLVO predictions for 2.25 mM LiCl salt with $\psi_{Mica} = -150\,\text{mV}$ and $\psi_{Al} = -90\,\text{mV}$. The Hamaker constant used is (3.1×10^{-10} J) and was determined from the pull-out forces (121 ± 9 mN/m). The solid and dashed curves correspond to solutions to the Poisson-Boltzmann equation for constant potential (solid line) and constant charge (dashed line) boundary conditions for both surfaces, respectively. The upper-right inset shows forces near contact, where attractive jumps into contact are denoted by arrows. Different colored points correspond to individual approaches. Representative FECO for this TS-Al/mica contact after the jump in is shown in the bottom left inset.

3.4.2.3 Adhesion

Adhesion is governed by both the interfacial energy and contact area between two surfaces.[28] We thus expect to measure a higher adhesion for the TS-Al films with mica based on its lower RMS roughness. In addition, the TS-Al films are exposed to the ambient atmosphere only after stripping, just prior to the experiment. We therefore expect the interfacial energy to be equal or higher than that of the R-Al films, which are exposed to the ambient atmosphere from the moment the samples are removed from the evaporation chamber.

Adhesion measurements were performed between the two different Al samples and acid-treated mica in dry N_2. The TS-Al and R-Al samples are always coated with aluminum at the same time to minimize any coating differences which might occur during evaporation. For the work of adhesion between TS-Al and mica we measure 325 ± 64 mJm^{-2}, whereas for the work of adhesion between R-Al and mica we measure 56 ± 8 mJm^{-2}. For comparison, Christenson measured 260 - 340 mJm^{-2} for the work of adhesion between two acid treated mica surfaces using the same method.[86] We attribute the large difference between TS-Al and R-Al mainly to the difference in surface topography and slight differences in preparation procedure. The low roughness of the TS-Al samples we expect the measured work of adhesion to be approaching the (theoretical) limit for contact in air between two atomically smooth surfaces composed of these materials.[85, 113] However, more experiments are needed to determine the adhesion force between these surfaces, in particular the role played by the native oxide layer. These experiments highlight an additional advantage of the TS process: the formation of metal films that are less prone to contamination. The values of adhesion energy measured are more illustrative of the difference in quality between the TS-Al and R-Al samples, rather than representing thermodynamic measures of the work of adhesion between Al and mica. In addition, these measurements were performed on rather thin, ~ 30 nm Al films, which started to show cracks after repeated measurements on the same contact spot (visible as 1 – 3 thin dark lines in the FECO).

3.4.2.4 Corrosion Experiments

Crevice corrosion is a form of corrosion that may occur in confined regions where lowered transport rates result in the formation of aggressive media.[151] Recently, Valtiner's group used the SFA to directly visualize crevice corrosion and corrosion inhibition of Al in 5 mM aqueous NaCl solution in real-time and with high resolution.[152] Their work shows that the SFA technique is uniquely suited to study crevice corrosion due to the ability to monitor film thickness changes in the region where the two surfaces are in contact in real-time.

Using the SFA, we performed preliminary measurements of crevice corrosion by monitoring the FECO intensity over time of TS-Al and R-Al samples that are in contact with mica and immersed in 5 mM aqueous NaCl solution. **Figure 3.8** shows the FECO intensity of both experiments over time. The results for TS-Al are shown on the left and the results for R-Al are shown on the right. The panels **B** and **C** show the FECO at different time points. Initially ($t = 0h$), the surfaces are in contact in dry N_2 after which we apply a compressive force of ~ 5 mN followed by the injection of a 5 mM aqueous NaCl solution. We monitor the corrosion process through the change in intensity of the FECO, and in **Figure 3.8** we show images of the same FECO taken 1 h and 6 h after the injection of the aqueous solution. Through the flattened area of the left-most fringe on each of the FECO images a line has been drawn which corresponds to the position of the line profile on the right panel. The area shown in red, normalized by the average intensity of the reference band (in blue) at the bottom of the FECO images, is used to generate the contour plots at the bottom (**Figure 3.8** D-E). The bottom contour maps (**D** and **E**) show the FECO intensity of the line profile as a function of time. The reference band is a direct measure of the intensity of the lamp and does not pass through the interferometer.

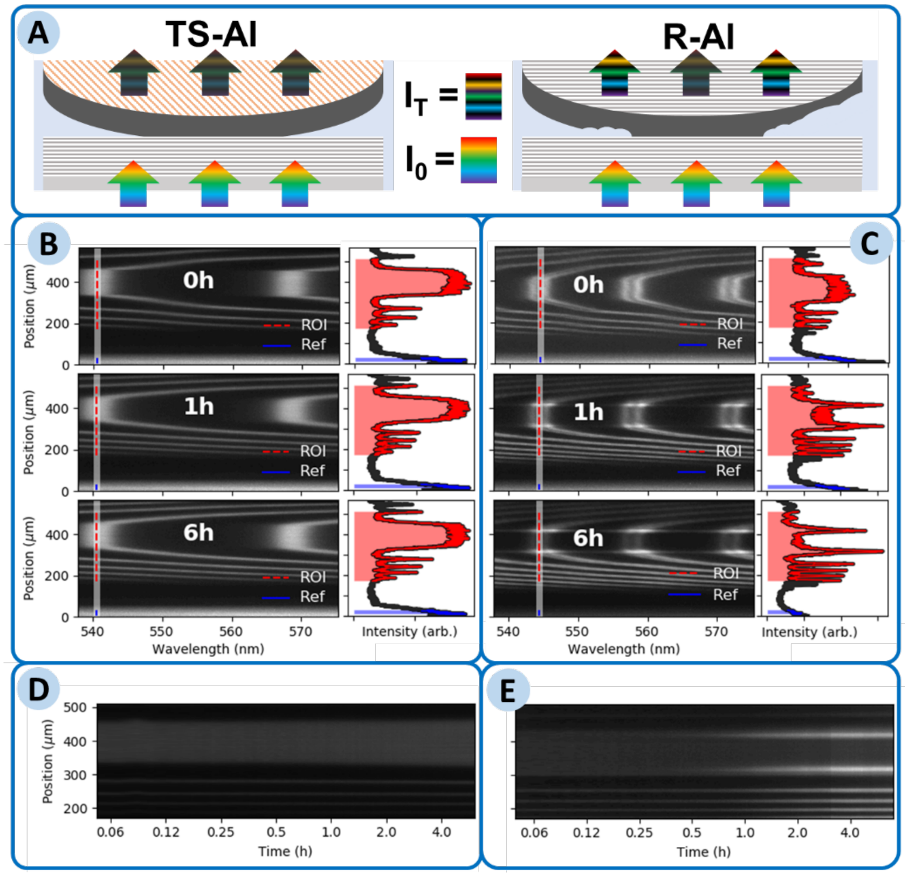

Figure 3.8. Interferometric study of corrosion of Al surfaces immersed in 5 mM NaCl of template stripped (left, TS-Al) and as-prepared Al (right, R-Al). (A) Schematic showing the incoming (I_0) and transmitted (I_T) light through the interferometric filter. As the Al layer corrodes and thins, the transmitted intensity increases. (B,C) FECO spectra taken at different time points. At t = 0 h, the surfaces are in dry N_2. Subsequently, 5 mM NaCl has been injected between the surfaces and has been left for t = 1 h and t = 6 h, respectively. As time progresses etch pits appear in the R-Al film and the film starts to thin, causing the FECO intensity to increase. The side panels at each FECO spectrum show an intensity plot taken across the vertical line in the figure. (D,E) FECO intensity across the red dashed line normalized by the reference intensity band in blue is shown as function of time. Plot intensity has been internally normalized to facilitate viewing. The intensity of TS-Al film remains nearly constant, whereas for the R-Al film it strongly increases over time.

An increase in intensity corresponds to a decrease in film thickness, which we attribute to the corrosion of the Al films. Both TS-Al and R-Al samples show some increase in intensity in the entire contact region over time (**Figure 3.8** D-E), but the R-Al films exhibit sharp increases at the edge of the contact zone. **Figure 3.8** shows less change in intensity of the TS-Al samples than of the R-Al, implying that the TS-Al samples are more stable towards corrosion than the R-Al samples. We studied multiple sample sets and found that the TS-Al always corrode slower (if at all) than the R-Al samples. However, the corrosion rate and location where the film thinned varied, sometimes starting at the edge of the contact region, and other times further outside of the contact. With both TS-Al and R-Al, we observed corrosion largely outside the region of contact, in contrast to what has been reported by Valtiner's group for Al, but not for Ni.[152, 153] The reason for this difference is not clear and will require further study. However it is possible that the films used in Valtiner's study were rougher as they evaporated their films at slow (< 0.3 nm/s) rates and the reported roughness for such films can be higher than reported here (*e.g.* 1.1 ± 0.2 nm RMS for 0.2 nm/s).[125] It is also possible that there are differences in the native oxide layer of the TS-Al and R-Al, or that differences in the grain sizes on the smooth side (TS-Al) and as-deposited side (R-Al) due to mica templating. More detailed investigations of the effect of roughness on corrosion will be the subject of future studies.

3.5 Summary

In summary, we introduced a novel method for the fabrication of ultra-smooth (0.2 nm RMS) aluminum thin films that are suitable for the measurement of surface forces with molecular length scales. The method relies on the use of high vacuum ($\leq 1 \times 10^{-7}$ torr), high deposition rates ($\geq$ 13 nm/s), and limiting the pre-deposition exposure time of the mica templates to ambient atmosphere. The surfaces are free of mica residues, which can be determined *in situ* when the mica template is removed under water due to the generation of H_2 gas at the Al surface. We demonstrate the suitability of the TS-Al for measurements in the SFA.

In particular, these measurements demonstrate that reducing the roughness of Al film from a RMS of 0.9 nm to a RMS of 0.2 nm has an important effect on the surface and interfacial properties. The lowered roughness could enable unambiguous interpretation of surface forces and adhesion, and could enable the measurement of short-range forces such as those electrostatic forces at high salt concentration, or forces due to liquid structure. The preparation procedure also ensures that samples can be prepared and safely stored while minimizing risks of contamination of the Al surface.

The observation that R-Al samples corrode faster than TS-Al samples implicates sub-nm roughness as an important factor which needs to be controlled against when studying the corrosion of Al. When compared to thermally evaporated (and rougher, RMS = 0.9 nm) Al films, the adhesion of the template stripped films in contact with acid-treated muscovite mica is up to six times higher. Finally, measurements of the surface forces between TS-Al and mica showed good agreement with DLVO theory for a surface potential of the TS-Al films in 2mM LiCl of -90mV and a Hamaker constant of 3.1×10^{-20} J, demonstrating the suitability of TS-Al for surface forces measurements.

Throughout we performed measurements in the SFA in transmission mode, using Al films of 30 – 45 nm in thickness, which requires stringent control over the deposition times at the high deposition rates used here. However, SFA experiments can easily be performed in reflection mode which allows for thicker films (*e.g.* 100 nm). Our fabrication method provides a route for force measurements on a substrate that is widely used both in multiple technologies.

4 Cooperative Tridentate Hydrogen-Bonding Interactions Enable Strong Underwater Adhesion[‡]

4.1 Abstract

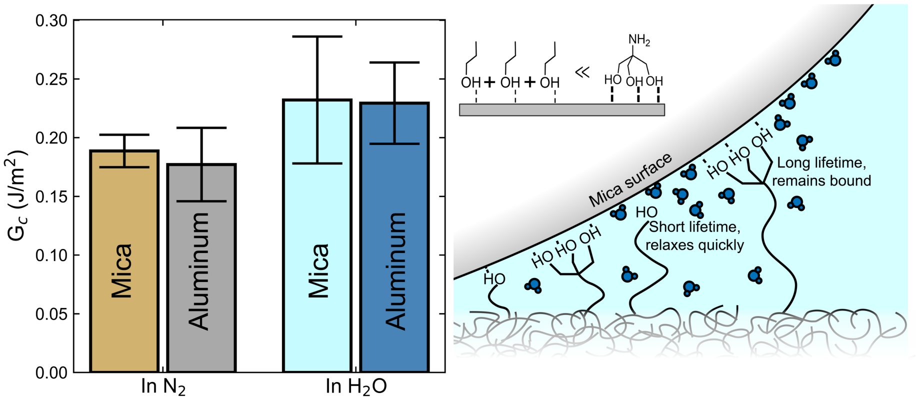

Figure 4.1. Schematic depicting a summary of Chapter 4: Left: adhesion of DGEBA-Tris with mica or aluminum in N_2 and in water. Right: proposed cooperative hydrogen bonding mechanism behind the strong underwater adhesion of DGEBA-Tris.

Multidentate hydrogen-bonding interactions are a promising strategy to improve underwater adhesion. Molecular and macroscale experiments have revealed an increase in underwater adhesion by incorporating multidentate H-bonding groups, but quantitatively relating the macroscale adhesive strength to cooperative hydrogen-bonding interactions remains challenging. Here, we investigate whether tridentate alcohol moieties incorporated in a model epoxy act cooperatively to enhance adhesion. We first demonstrate that incorporation of tridentate alcohol moieties leads to comparable adhesive strength with mica and aluminum in air and in water. We then show that the presence of tridentate groups leads to energy release rates that increase with an increase in crack velocity in air and in water, while materials lacking these groups do not display rate-dependent adhesion. We model the rate-dependent adhesion to estimate the activation energy of the interfacial bonds. Based on our data, we estimate the lifetime of these bonds to be between 2 ms and 6 s, corresponding to an equilibrium activation energy between $23k_BT$ and $31k_BT$. These values are consistent with tridentate hydrogen bonding, suggesting that the three alcohol groups in the Tris moiety bond cooperatively form a robust adhesive interaction underwater.

[‡] This chapter was previously published as "Lamberty, Z. D.; Tran, N. T.; van Engers, C. D.; Karnal, P.; Knorr Jr., D. B.; Frechette, J., Cooperative Tridentate Hydrogen-Bonding Interactions Enable Strong Underwater Adhesion. *ACS App. Mater. Interfaces,* **2023**, *15* (29), 35720-35731." and is adapted with permission from all co-authors.

4.2 Introduction

Multidentate hydrogen-bonding moieties are promising functional groups for strong and water-resistant adhesives.[21] Multidentate bonds are thought to be more stable than their monodentate counterparts, as multidentate interactions are kinetically and entropically favored due to the coordination between multiple adjacent binding groups.[154] Well-studied multiple adjacent hydrogen-bonding groups in adhesion include catechols (Dopa)[155] and ureido-pyrimidinone (UPy),[156] both of which were proven to maintain strong interactions underwater. Multidentate hydrogen-bonding moieties also interact strongly with a wide range of surface chemistries.[57] Single-molecule[31, 157] and macroscale[13, 156] measurements support the hypothesis that adjacent alcohol groups work cooperatively to stabilize and strengthen adhesive contact, helping to resist displacement by interfacial water.[158] Yet, a quantitative relationship linking the cooperative bonding dynamics to strong macroscale adhesion remains elusive.[158]

Recent work with the tri-alcohol molecule tris(hydroxymethyl)amino methane (Tris) shows the potential of these moieties for enabling strong underwater adhesion.[83, 159] These tridentate groups are particularly well-suited for epoxies as they can be readily reacted into the polymer backbone through the amine linkage. Stronger-bonded and water-tolerant epoxies are essential for structural adhesive and composite applications.[5, 160, 161] Tran and co-workers showed that a simple surface pretreatment with Tris buffer improved dry and hot/wet aged lap shear strength of diglycidyl ether of bisphenol A (DGEBA) epoxy-bonded aluminum to a level comparable with their best polydopamine surface treatments.[83] DGEBA is a well-studied and commonly used epoxy adhesive[159] and thus serves as a suitable model backbone. Next, they incorporated Tris groups directly in the backbone of DGEBA (Tris–DGEBA, see **Figure 4.2**) and demonstrated lap shear strength after water aging that rivaled the strength of a silane pretreatment benchmark but without the need for the extensive surface pretreatment.[159] Furthermore, they demonstrated that this improvement was not seen in epoxies functionalized with monodentate or bidentate alcohol groups, even when accounting for the hydroxyl concentration within the epoxy.[159] These prior studies motivate the need to uncover the importance of cooperative hydrogen bonding in adhesion generally, and due to its industrial importance as a structural adhesive, of Tris-containing epoxies specifically.

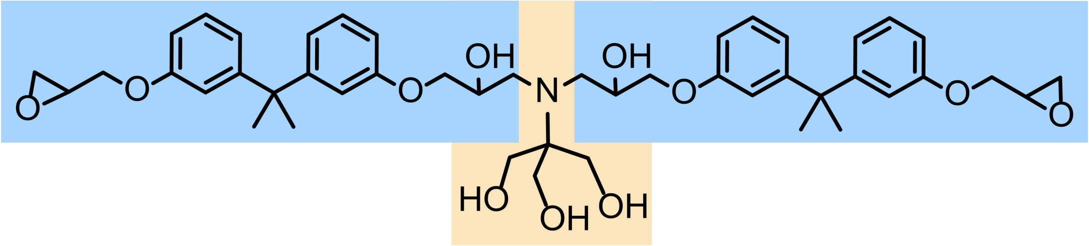

Figure 4.2. Oligomer structure. Structure of the Tris-modified DGEBA (DGEBA–Tris) oligomer. DGEBA sections are shaded in blue, and the Tris moiety is marked in yellow.

Relating macroscopic adhesion measurements to intermolecular forces can be both experimentally and theoretically challenging, even in the limit where adhesive contact is caused by breaking interfacial bonds (and not bulk viscoelasticity). One approach that has been successful involves quantifying the rate dependence of crack propagation on the strength and stretch of chemical bonds in adhesive contact. The finite bond lifetime from chemical kinetics leads to a bond dissociation force that increases with the loading rate on an individual bond, described through the Bell–Evans model.[55] Macroscopically, the process is averaged over many bonds throughout the contact region, leading to rate-dependent adhesion that scales with $[\ln(u)]^2$, where u is the stretching velocity of the interfacial bonds during crack propagation.[69] Moreover, the equilibrium bond lifetime τ, which itself is related to the bond activation energy E_a through Eyring's equation, leads to a transition from a rate-independent to a rate-dependent debonding force as the detachment velocity increases. By determining this characteristic transition velocity, it is then possible to determine τ (and thus E_a) for bonds formed in adhesive contact. This general methodology has been employed to characterize the adhesion of covalent bonds in a PDMS-silanized glass interface,[69] the role of electrostatic interactions in hydrogel–hydrogel adhesion,[48] and highly entangled hydrogen-bonding networks between oxidized PDMS and silicon.[56, 74] In this work, we hypothesize that we can determine if cooperative hydrogen bonding is present in DGEBA–Tris by characterizing and modeling how adhesive strength depends on the rate of crack propagation.

Here, we investigate the mechanism by which the incorporation of Tris groups in the backbone of DGEBA epoxies improves underwater adhesion. We use a model epoxy adhesive consisting of two DGEBA groups joined by a single Tris moiety, DGEBA–Tris (**Figure 4.2**). We first report on the dependence of the strength of DGEBA–Tris/mica contact on the rate of crack propagation[47] in air. We compare the adhesion of cured and uncured DGEBA–Tris to mica to other DGEBA epoxies that do not contain the Tris group. We then measure adhesion between thin films of DGEBA–Tris oligomers to mica in air and water using the surface forces apparatus (SFA).[130] We further test the adhesion of DGEBA–Tris to aluminum in air and water to demonstrate the application to industrially relevant substrates. Finally, we model[69] the dependence of the adhesive energy on the rate of crack propagation to obtain the threshold velocity above which adhesion is rate-dependent. From this critical velocity, we obtain estimates of interfacial bond lifetimes that we can use to test the hypothesis that cooperative hydrogen bonding is responsible for the strong adhesion in air and in water of DGEBA–Tris epoxies.

4.3 Connecting Crack Propagation Velocity to Chemical Bond Kinetics

Consider the interaction between two macroscopic surfaces, as illustrated in **Figure 4.3a**, where adhesion is dominated by bonds formed between the interacting surfaces in contact. A crack of length ℓ exists between the two interacting bodies at the edge of the contact region. As a tensile force F is applied, the bodies are pulled apart and the crack propagates at the interface between the materials, while adhesive forces act to hold the bodies together and resist crack motion. The location of the crack is determined by the balance between elastic energy and the energy release rate G, which comprises interfacial bonds and dissipative phenomena that oppose the crack motion.[37] If we zoom in around the crack tip (**Figure 4.3b**), individual chemical bonds of activation energy E_a and number density Σ act to hold the surfaces together. These bonds must be broken for the crack to advance. If each bond is attached to the bottom surface by a polymer of spring constant M and stretched at a velocity V_{stretch}, the loading rate on each bond is $\frac{dF}{dt} = MV_{stretch}$. We approximate $V_{stretch} \approx u = \frac{d\ell}{dt}$, where u is the velocity of the crack. The Bell–Evans theory tells us that the energy dissipated in breaking each bond depends on the loading rate,[55] and many such bonds must be broken simultaneously to extend the crack. Chaudhury extended the Bell–Evans theory to macroscale contacts by summing up the energy dissipated during the breaking of a multitude of bonds to obtain the relationship given in **Eqn. 4.1** between G and the crack velocity[69]

$$(G - G_0) = \left(\frac{\Sigma}{2M}\right)\left[\left(\frac{k_BT}{\lambda}\right)\ln\left(\frac{Mu\lambda\tau}{nk_BT}\right)\right]^2. \tag{4.1}$$

In **Eqn. 4.1**, G_0 is the threshold (rate-independent) energy release rate, λ is a characteristic length scale for the bonds, and n is the number of bonds per chain. Note that **Eqn. 4.1** only applies in the limit where the $\frac{Mu\lambda\tau}{nk_BT} \gg 1$ or when the thermal energy of the bonds is lower than the equilibrium energy barrier for bond dissociation.[25] In the slow crack velocity limit ($\frac{Mu\lambda\tau}{nk_BT} \ll 1$), the thermal energy dominates, and the energy release rate is by definition $G = G_0$. Finally, the lifetime of a bond τ in **Eqn. 4.1** can be estimated using Eyring's equation[69]

$$\tau = \frac{h}{k_BT} exp\left(\frac{E_a}{k_BT}\right), \tag{4.2}$$

where h is Planck's constant, k_B is Boltzmann's constant, and T is the temperature. Recently, more rigorous models have been developed that are in qualitative agreement with **Eqn. 4.1**, but require additional details for their implementation.[24] While **Eqn. 4.1** can be applied to any type of interfacial bond, the onset of rate dependence is highly dependent on τ and, by extension, E_a. For an individual hydrogen bond, $E_a \approx 10k_BT$.[28, 48] As a first-order approximation, for cooperative hydrogen bonds, we expect E_a to scale with the number of hydrogen bonds, N, acting cooperatively such that $E_a \approx N * 10k_BT$. In the case of Tris and tridentate bonds, $N = 3$ and $E_a \approx 30k_BT$, which leads to a bond lifetime of $\tau \approx 1$ s and the onset of rate dependence of adhesion at a threshold velocity of $u \sim 0.5$ nm/s. Therefore, we expect rate-dependent behavior in the nm/s regime to correspond to cooperative tridentate hydrogen bonding. In contrast, for monodentate hydrogen bonding, the threshold velocity would be $u \sim 1$ m/s. This rate dependence should occur in both air and in water if cooperative bonds can be formed but should be absent in epoxy analogs that lack Tris groups. **Figure 4.3c** demonstrates the expected dependence of G with the crack velocity obtained from **Eqn. 4.1** for two nominally identical materials (same number of sites and polymer spring constant). While the threshold velocity occurs at ~0.5 nm/s for tridentate hydrogen bonds ($E_a = 30k_BT$ and $\tau \approx 1$ s), this transition would not occur until 1 m/s for a monodentate bond ($E_a = 10k_BT$ and $\tau \approx 10^{-9}$ s). For all but the fastest measurements, adhesion from single hydrogen bonds will be rate-independent.

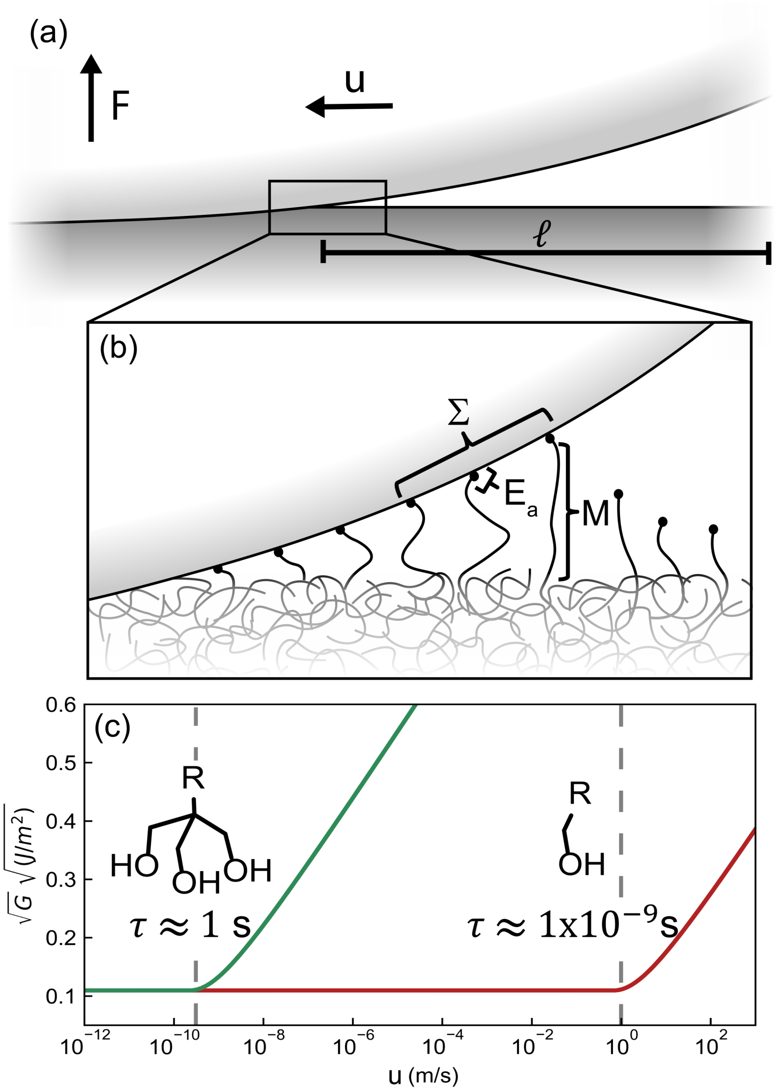

Figure 4.3 Relationship between interfacial bonds and adhesion. (a) Diagram of two adhesive surfaces in contact. F is the force on the two bodies, ℓ is the length of the crack, and $u = d\ell/dt$ is the velocity of the crack. (b) Enlarged schematic of the interface near the crack tip illustrating the interfacial bonds between the two surfaces. Σ is the surface density of bonds, E_a is the bond activation energy, and M is the polymer spring constant. (c) Predictions from **Eqn. 4.1** for the dependence of G vs crack velocity contrasting individual and multidentate hydrogen bonds. For τ = 1 s (green), the rate-dependent transition occurs at ~0.5 nm/s, while for τ = 1 s (red), the transition occurs at ~1 m/s.

4.4 Materials and Methods

4.4.1 Materials

HNO_3 (68%, BDH), ethanol (200 proof, Pharmco), H_2O_2 (30%, Fisher), H_2SO_4 (95.0%, J. T. Baker), tetrahydrofuran (THF, >99.5%, Supelco), ethyl acetate (99.9%, Fisher), muscovite mica (Ruby, ASTM V-1/V-2, S&J Trading), silver pellets (99.999%, Alfa Aesar), aluminum pellets (99.999%, Kurt J. Lesker), DGEBA (Hexion Inc. EPON Resin 825), EPON Resin 1004 F (Hexion Inc.), and 2-amino-2-(hydroxymethyl)-1,3-propanediol (Tris, >99.9%, Sigma-Aldrich) were purchased and used as received. Deionized (DI) water (>18.2 MΩ cm resistivity) was obtained from an EMD Milli-Q Integral Water Purification System.

4.4.2 Synthesis of DGEBA–Tris Oligomers

2-(Bis(1-hydroxy-2-(4-(2-(4-(oxiran-2-ylmethoxy)phenyl)propan-2-yl)phenoxy)ethyl)amino)-2-(hydroxymethyl)propane-1,3-diol diglycidyl ether of bisphenol A–tris(hydroxymethyl)amino methane, DGEBA–Tris) oligomers were synthesized through nucleophilic epoxide ring opening of the epoxy DGEBA oligomers by Tris amine groups, as reported previously.[159] In brief, DGEBA monomers and Tris (2:1 stoichiometric ratio) were dissolved in ethanol (5.6 M DGEBA, 2.8 M Tris) at 78 °C under constant stirring for 18 h to allow the Tris molecules to bind two DGEBA groups through the amine linkage, forming the DGEBA–Tris oligomer. Afterward, the oligomers were diluted to 180 mM in ethanol for storage.

4.4.3 Preparation of Self-Arresting Crack Samples

Large muscovite mica sheets (∼2 cm × 6 cm, 10–30 μm thickness) were cleaved in a laminar flow cabinet and cut into rectangles comprising mostly of a single crystal. The sheets were then rinsed with 5 mL of an 8 μL HNO_3/50 mL H_2O solution to exchange K^+ ions from the mica surface with H^+ and then blow-dried with N_2. Oligomer or polymer solutions were created that had an equal concentration of 34 mM DGEBA units in THF (e.g., 17 mM DGEBA–Tris with 2 DGEBA units per oligomer). Then, 500 μL of solution was spin-coated onto the HNO_3-treated mica sheets, followed by heating for 1–2 h at 100 °C under vacuum to remove residual solvent. Meanwhile, thick mica base sheets (∼150 cm^2 area, ∼1 mm thick) were freshly cleaved and rinsed with 20 mL of HNO_3 solution before drying as before. After the oven-drying was complete, the oligomer-/polymer-coated mica sheets were placed polymer-side down on the mica base sheets and the two sheets were firmly pressed together. Multiple epoxy-coated sheets were affixed to the same base sheet and then cut apart to size. A steel block was placed on each sample to provide additional weight during annealing in an oven for 1 h at 80 °C under vacuum. Afterward, uncured samples were removed to be tested, while samples to be cured remained in the oven as the temperature was ramped over a period of 2 h to 150 °C under a gentle flow of N_2, followed by curing at 150 °C for the requisite curing time (6 or 18 h).

4.4.4 Preparation of Surfaces for SFA Experiments

The preparation of mica surfaces is described in detail in our prior work.[26] Details are mentioned here for clarity. Single-crystal muscovite mica sheets (3–8 μm) were cleaved in a laminar flow cabinet and placed on a larger mica backing sheet. A thin layer of silver (~50 nm) was then thermally evaporated onto the exposed side of the mica sheets (using a Kurt J. Lesker Nano 38 thermal evaporator). The mica surfaces were then glued to the SFA disks using a uniform layer of EPON epoxy (~5 μm) deposited onto the hemi-cylindrical quartz lenses (radii of curvature ~ 2 cm). To obtain a uniform EPON layer, the glue was first dissolved in an ethyl acetate solution that was then spin-coated on a disk. After spin-coating, the glue was melted by heating the lenses on a hotplate at 225 °C and a cleaved sheet of mica was placed silver-side down on the lens. After cooling, the mica lenses were immersed in a weak HNO_3 solution (8 μL HNO_3/100 mL H_2O) to exchange K^+ ions from the mica surface with H^+. In all SFA experiments, one of the mica surfaces was coated with the DGEBA–Tris oligomer. For oligomer-coated lenses, a solution of 17 mM DGEBA–Tris oligomer in ethanol was spin-coated onto the H^+ mica lenses and then annealed in a vacuum oven at 80 °C for 6 h to remove excess solvent. Ultra-smooth aluminum surfaces were fabricated according to our previously published procedure[26] by templating thermally evaporated aluminum films with mica and then removing the mica template in water.

4.4.5 Atomic Force Microscopy Imaging

Atomic force microscopy (AFM) data were recorded using a Bruker Dimension 3100 atomic force microscope (Bruker Nano, Santa Barbara, CA) in tapping mode and analyzed using Gwyddion 2.52. For processing the AFM data, we align the line profiles using a first-degree polynomial (linear slope) and subtract the background using a third-degree polynomial for both the x- and y-directions. Root-mean-square (rms) roughness values were calculated over a 5 μm × 5 μm area using Gwyddion's built-in statistical functions. AFM imaging was performed on both as-prepared (dry) samples and samples that had been soaked in DI water overnight, to reproduce the conditions in SFA experiments.

4.4.6 Ellipsometry

Ellipsometry measurements were performed with an Accurion Nanofilm EP3 single-wavelength (532 nm) variable-angle imaging ellipsometer with a 20× objective. DGEBA–Tris oligomer films were deposited onto clean silicon wafers using the same procedure as for SFA samples, except for the K^+ ion exchange step. We assume that the oligomer thickness is (on average) identical to that of the films deposited on the mica sheet for SFA experiments. For each sample, first, the angle of incidence was varied to find the Brewster's angle and then the reflectance of the sample was measured at angles around the Brewster's angle. Accurion's EP4 software was then used to analyze the measured data, and both the refractive index and thickness of oligomer films were varied to fit the reflectance data. A film thickness of 115.4 ± 1.5 nm with a refractive index of n_D = 1.582 was obtained from ellipsometry. The refractive index value for the DGEBA–Tris oligomer was then used for the analysis of the SFA interferometric data.

4.4.7 Surface Tension

Surface tension measurements were conducted with a Dataphysics OCA 15EC contact angle goniometer. The fluids investigated were 18.2 MΩ cm H_2O that was either in contact with DGEBA–Tris films or only in a glass beaker (control) for 24 h. A 25 µL drop was hung from a clean stainless-steel needle with an OD of 0.51 mm. Measurements were performed in laboratory air. Images were taken continuously over 100 s, during which no noticeable change in surface tension occurred. Image analysis and surface tension calculations were performed by Dataphysics' SCA software.

4.4.8 Adhesion Measurements through Self-Arresting Crack Propagation

Peeling by crack propagation and arrest was performed with a procedure inspired by previously reported methods[46, 47] on a modified Zeiss Axiovert 135 inverted microscope equipped with a translating stage. The method relies on peeling apart two adhered surfaces by bending the upper (more flexible) sheet and monitoring the subsequent propagation of the peeling front (crack). The crack will advance and eventually arrest once mechanical equilibrium is reached between the elastic bending of the sheet and the adhesive forces resisting separation. All the self-arresting crack measurements were conducted between two mica base sheets adhered together with a thin layer of epoxy prepared as described above. Adhesion measurements started by prying apart the two mica sheets at one end with a needle, followed by inserting a 1 mm diameter glass rod as a spacer in the gap created by the needle. The glass rod creates a crack at the epoxy–mica interface that grows and arrests once equilibrium between the bending and surface forces is achieved. Then, we advanced the glass rod and monitored the associated crack propagation. As the glass rod moved to peel the mica sheet, the crack length was imaged using a 5× objective and a 555–565 nm band-pass filter to observe the interference patterns produced by the crack opening. Acquisition time began at 10 fps for each measurement but gradually slowed to 1 frame per 5 min over the course of an experiment as the rate of crack propagation slows down. To quantify the crack length, the edge of the crack was assumed to be approximately the location of the first visible constructive interference fringe. For each measurement, a location ~3 mm from the previous crack front was located with the camera and then the spacer was rapidly pushed by 3 mm to move the crack into view. Each time the glass rod was moved to advance the crack, the crack length was measured for several hours as it advanced and returned to its steady-state length. This process was repeated several times on each sample by continuing to advance the crack further. The crack velocity was calculated by first smoothing the raw crack length as a function of time over using a first-degree Savitzky–Golay filter and then interpolating the data to a continuous function to eliminate the effects of the variable sampling rate. Dividing the interpolated function into 1000 logarithmically spaced points allows for fitting crack position vs time to a line using the 60 nearest neighbor points in time and calculation of the instantaneous crack velocity as the fitted slope. The thicknesses of the mica top sheets are measured through multiple-beam interferometry[162] by evaporating ~50 nm films of Ag onto both sides. Measurements were repeated at least five times on each sample and with at least two separate samples.

4.4.9 SFA Measurements

Surface force measurements were performed with an SFA 2000 (SurForce LLC, see Supplementary Information **Figure S4.11**) with an Andor Shamrock spectrometer and CCD camera (Andor Zyla 5.5 sCMOS). Technical aspects of the SFA are given elsewhere, and only the aspects specific to our experiments are described here.[26] SFA measurements were performed between disks arranged in a cross-cylindrical configuration, which is equivalent to a sphere-plane geometry. One of the surfaces is mica, and the other is mica coated with a DGEBA–Tris oligomer. The separation between the surfaces was obtained using multiple-beam interferometry.[162] Spectral data are converted into surface separation using the fast spectral correlation algorithm.[26, 131] A microstepping motor was used to control the motion of the lower surface, which was mounted on a cantilever spring with a spring constant of 2238 ± 44 N/m. The optical constants of the mica and silver were taken from the literature,[133, 134] while the refractive index of the DGEBA–Tris oligomer was measured using ellipsometry. Mica thickness was measured by conducting separate calibration experiments with mica pieces of the same thickness. Because of reswelling and minor stretching in the film during retraction, the film thickness changes when the surfaces are in contact with an applied load (tension or compression). Therefore, to determine the contact radius, we converted the shape of interference fringes at any given time and extract the edge of the flattened region of the profile. The edge of contact is defined by the slope of the profile, with any slope below 0.5 nm vertical change per 1 μm horizontal change in the profile designating contact between the surfaces. The radial velocity u_r was then found by analyzing the rate of change of contact radius over time. The instantaneous value of u_r was estimated by calculating the slope of a vs t for the 10 nearest neighbor points at the time of interest.

After assembling the disks in the SFA, the system was allowed to equilibrate under a gentle flow of dry nitrogen for at least 1 h with all equipment running prior to any measurements. For each adhesion measurement, the surfaces were brought into contact quasi-statically using individual steps with a drive velocity of ~28 nm/s for 0.5 s followed by a 4.5 s pause. Once contact between the surfaces was made (D = 0, visually seen as a sudden slowing of fringe movement), the samples were compressed at the same quasi-static velocity for an additional 800 s to reach a dwell force of 5 mN ($F/R \sim 0.3$ N/m). Afterward, the surfaces relaxed while in contact for a dwell time of 5–20 min. After dwell, a constant pre-determined motor velocity (between 5 and 75 nm/s) was used to separate the surfaces until detachment (jump out). For each experiment, adhesion between the DGEBA–Tris oligomer-coated surface and mica was first measured in air twice before adding water. Water was then introduced by injecting 50 μL of DI water between the surfaces to form a capillary meniscus. To reduce the effect of evaporation, an additional 3 mL of water was injected into the bottom of the SFA chamber. After injection, the samples were left to equilibrate in water for at least 1 h before further measurements. Depending on the motor velocity, it took between 5 and 30 min to separate the surfaces. After each contact, the radii of curvature of the surfaces were measured at two orthogonal orientations and the geometrical mean was reported, $R = (R_1 R_2)^{1/2}$. Then, the relative position of the two disks was changed to be able to repeat the measurements on a new spot. Three different samples were investigated, with 8–17 independent spots per sample. Motor velocity was calculated for each retraction by calibrating the sample movement to the applied voltage on the motor when the samples reached a force-free regime.

4.5 Results & Discussion

4.5.1 Characterization of the DGEBA–Tris Oligomer Films

We characterized the surface roughness of the DGEBA–Tris films using AFM after the annealing step (as-deposited), as well as after the samples were submerged in water overnight (**Figure 4.4**). AFM imaging of the annealed films reveals a featureless surface with a low rms roughness of 0.27 nm (2.21 nm peak-to-valley) over a 1 µm × 1 µm area. Similarly, imaging of DGEBA–Tris films that were soaked in DI water overnight showed a surface that remains smooth and featureless but with an rms roughness of 1 nm (9.23 nm peak-to-valley). The increase in rms roughness is consistent with the small degree of swelling observed in SFA experiments.

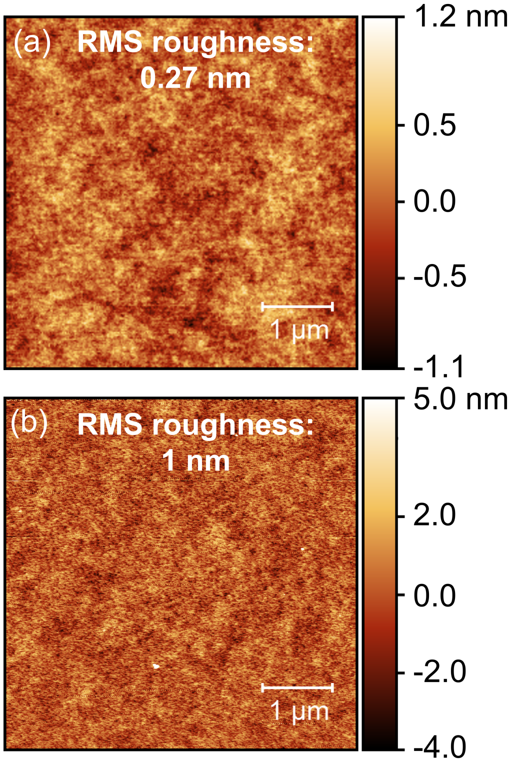

Figure 4.4 Characterization of DGEBA–Tris using AFM. (a) AFM image of a representative area on the surface of an as-deposited DGEBA–Tris film, showing an rms roughness of 0.27 nm. (b) AFM image of the surface of a DGEBA–Tris film that has been soaked in water overnight. The surface is featureless with a roughness of 1.0 nm rms.

Bulk DGEBA–Tris films are insoluble in water. We also investigated if some small amount of DGEBA–Tris might dissolve in water and become surface active, which in turn could affect adhesion. To do so, we immersed 4 cm × 4 cm sheets of mica coated with the DGEBA–Tris oligomer films in a small amount of DI water for 24 h at room temperature. We then measured the surface tension of the water using a pendant drop tensiometer and obtained 72.5 ± 0.08 mN/m, indistinguishable from that of clean water.

4.5.2 Tridentate and Monodentate Adhesion in Air

To determine if cooperative bonding is important in the adhesion of DGEBA–Tris, we compare its adhesion with mica to analogs without the Tris moiety. The first control is the primarily monomeric DGEBA of an average molecular weight (MW) of 355 g/mol, hereafter referred to as DGEBA-355. Since DGEBA-355 is a liquid at room temperature, it is cured for 18 h at 150 °C to form a solid film. The second control is a glassy DGEBA polymer with an average of 5.5–6 repeat units per chain; this material has an average MW of 1750 g/mol and is referred to as DGEBA-1750. DGEBA-1750 samples were also further cured at 150 °C for 18 h. The last control is a test of the experimental protocol itself; here, we do not employ any adhesive and characterize the interfacial crack propagation during the separation of two mica sheets (no intervening oligomer or polymer layers). As none of these materials contain Tris groups, we do not anticipate them to exhibit rate-dependent adhesion.

Our primary tridentate material is oligomeric DGEBA–Tris (**Figure 4.2**), where each molecule contains exactly one Tris group. Oligomeric DGEBA–Tris is a glassy solid with a T_g of 31.7 °C. To better compare with our control materials, we also investigate DGEBA–Tris that has been cured at 150 °C for 18 h. Curing DGEBA–Tris will also increase the average chain length, leading to a higher polymer spring constant.

For all experiments, the thin mica top sheet is coated with a thin (∼100 nm) oligomer/polymer film and then bonded to a thick mica base sheet (**Figure 4.5**). We propagate a crack through the epoxy/mica base sheet interface and monitor the crack growth and velocity over time as the crack returns to its equilibrium length ℓ_0. We choose to use self-arresting crack propagation to characterize the probe adhesion across orders of magnitude in crack velocities in a single experiment. Representative crack length versus time curves for each epoxy is shown in **Figure 4.6a**. When peeling mica from mica, DGEBA-355, and DGEBA-1750, the crack rapidly extends and reaches its equilibrium length within 1–2 s. That first second of motion, indicated by the gray shaded area, is dominated by dynamic effects including air resistance, but afterward, the crack length remains nearly constant. In contrast, for oligomeric DGEBA–Tris samples, we observe continual crack motion over several hours, which gradually slows down as the crack nears its final length. Similar long-term crack movement is observed for cured DGEBA–Tris samples, although extension halts after about an hour.

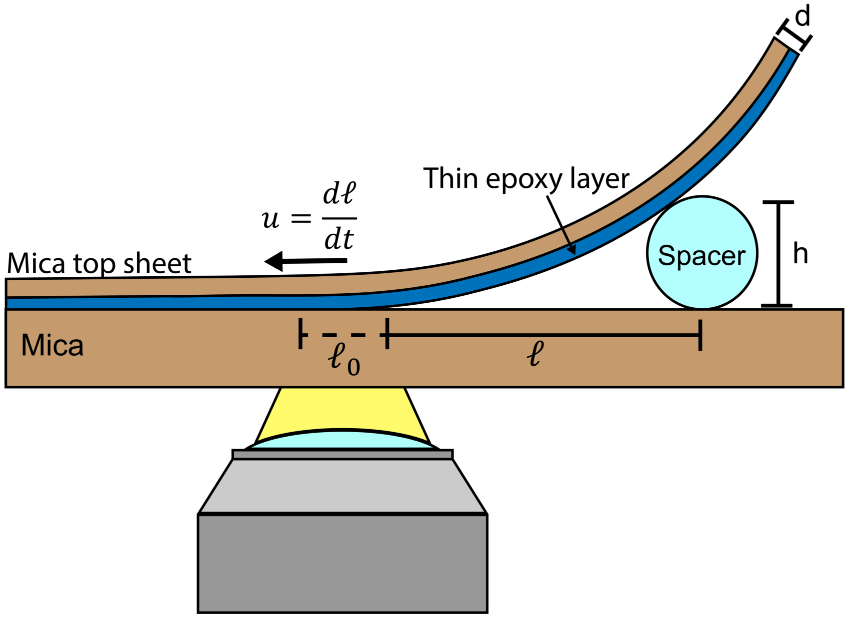

Figure 4.5 Diagram of interfacial crack propagation measurements. Schematic of the geometrical configuration for interfacial crack measurements, where ℓ is the crack length, h is the height of the spacer, and d is the thickness of the mica top sheet. Note that the thin epoxy layer (blue) is ∼100 nm thick and is extremely thin relative to the mica top sheet thickness (10–30 μm) (not to scale).

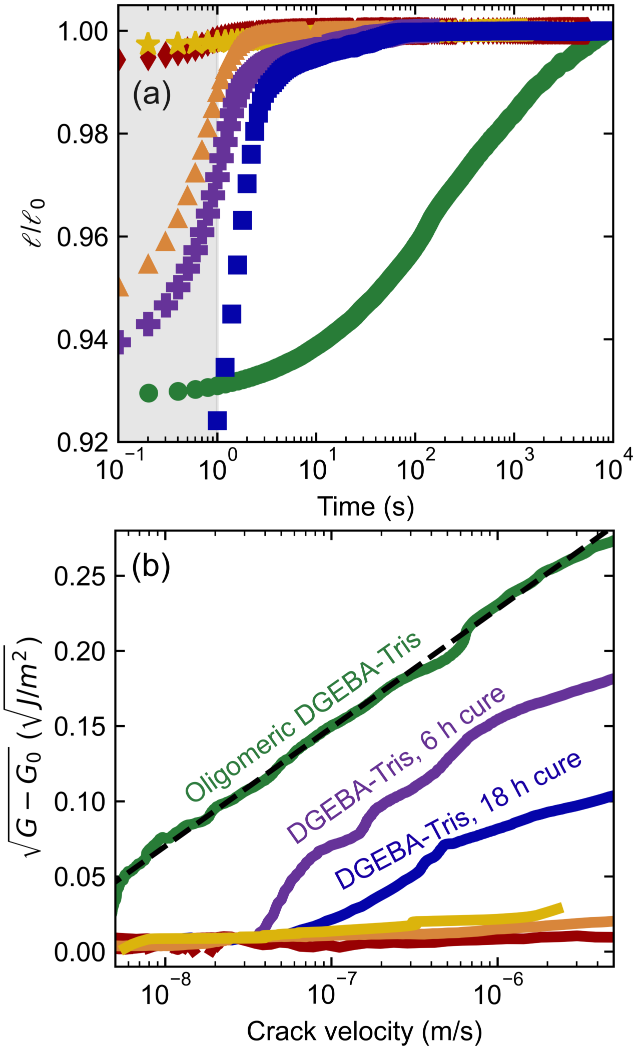

Figure 4.6 Crack growth and adhesion dynamics. The materials shown are bare H$^+$ mica (orange triangles), oligomeric DGEBA–Tris (green circles), DGEBA–Tris cured for 6 h (purple crosses) or 18 h at 150 °C (blue squares), and DGEBA-355 (yellow stars) and DGEBA-1750 (red diamonds), both cured for 18 h at 150 °C. The opposing surface for all materials is a thick H$^+$ mica sheet. (a) Crack length normalized by the final measured crack length value (ℓ_0, dashed line) as a function of time after the movement of the spacer. The crack propagation in the first second (shaded region) is dominated by air resistance. (b) Scaled rate-enhanced adhesion vs crack velocity on a logarithmic scale. The black dotted line shows fit to oligomeric DGEBA–Tris data ($R^2 = 0.997$)

The length of the crack is controlled by the force balance between the bending moment on the mica top sheet and the adhesive forces holding the materials together. For rigid materials, this force balance can be expressed by the equation[47]

$$G(u) = \frac{9\mu d^3 h^2}{6\ell^4}. \qquad (4.3)$$

Here, μ is the shear modulus of the top mica sheet ($\mu = 25$ GPa, Poisson ratio $\nu = 0.21$),[135] d is the thickness of the top mica sheet (measured independently, ~10–30 μm), and h is the fixed height of the spacer. We then used the measured crack length as a function of time to calculate the crack velocity $u = \frac{d\ell}{dt}$ and the corresponding $G(u)$ for each sample. Once we reach a crack velocity of < 1 nm/s, we consider the crack to have stopped and measure the final value of $\ell = \ell_0$ at least 1 h after this point. The value of $\ell_0$is taken to correspond to G_0, the threshold energy release rate. For most samples, the crack stops within 15 min. However, oligomeric DGEBA–Tris samples required us to wait longer (several hours) to reach an equilibrium crack length, and even then, small changes in the crack length continued for at least one day.

We investigated if the energy release rate increases with crack velocity and if the rate dependence for DGEBA–Tris follows the scaling expected for the breaking of interfacial bonds described by **Eqn. 4.3**. Specifically, **Eqn. 4.3** predicts a linear relationship between $(G - G_0)^{1/2}$ and $\ln(u)$. As illustrated by **Figure 4.6b**, oligomeric DGEBA–Tris films have a strong enhancement in adhesion with crack velocity, for a crack velocity above 5 nm/s. Moreover, the increase in energy release rate with crack velocity follows the scaling predicted by **Eqn. 4.1**. Similarly, adhesion of cured DGEBA–Tris films also increases with crack velocity but only for u > 50 nm/s. Cured DGEBA–Tris films reliably show an increase in the onset velocity for adhesion-enhancement but have higher variability than oligomeric DGEBA–Tris samples (Supplementary Information **Figure S4.12**). In contrast, the adhesion of mica, DGEBA-355, and DGEBA-1750 does not increase with an increase in crack velocity after the first second of motion (<10 μm/s).

The fact that adhesion of DGEBA–Tris films increases with crack velocity but none of the controls do strongly suggests that the increase in the energy release rate is due to the presence of Tris groups. Moreover, the linear relationship between $(G - G_0)^{1/2}$ and $\ln\left(\frac{d\ell}{dt}\right)$, as predicted by **Eqn. 4.1**, supports the hypothesis that the increase in adhesion is due to the breaking of interfacial bonds. Finally, the shift to higher threshold velocity between oligomeric and cured DGEBA–Tris suggests an increase in the effective polymer spring constant, *M*, with curing.[68]

We extract an estimate of the interfacial bond lifetime, τ, from the dependence of the energy release rate on the crack velocity for oligomeric DGEBA–Tris using **Eqn. 4.1**. In addition to the bond lifetime, the spring constant of the oligomer (*M*) and the surface bond density (Σ) are also unknown, but only two of the three parameters can be obtained independently from **Eqn. 4.1**. All the other constants are known and displayed in **Table 4.1**. Once Σ and *M* are known, we can obtain τ from the intercept of the data shown in **Figure 4.6b** (R^2 is between 0.96 and 0.997 for each curve). Fortunately, an upper limit on Σ and a lower limit on *M* will bound τ. To obtain a lower bound for *M*, we estimate the force–extension relationship of a single DGEBA–Tris oligomer using the modified freely jointed chain model combined with literature values for similar materials (see Supplementary Information **Section 4.7.3**).[58, 62, 163-165] The stretching caused by entropic forces is a lower bound, with $M_{\text{entropic}} \geq 0.008$ N/m. The upper bound would be a high extension limit dominated by the segment elasticity of the carbon backbone, giving $M_{\text{elastic}} = 5$ N/m. While these two numerical values are limiting cases, we suspect that the majority of the energy stored in the chain occurs in the high extension regime. To determine an upper bound for Σ, we rely on the known structure of mica. For the upper bound, we can assume that all the surface oxide groups on mica are taken by the −OH in the DEGBA–Tris oligomer, leading to a density of $\sim 1.4 \times 10^{19}$ #/m^2.[87, 166, 167] The lower theoretical bound for the number density of bonds with the mica surface is zero.

Table 4.1. Parameters used in Eqn. (4.11) and values obtained from fitting the data in Fig. 4.6b and Fig. 4.10.

	T	λ	G_0		Σ	M	τ	E_a
	°C	nm	J/m^2		#/m^2	mN/m	s	k_BT
Dry	20	0.18 (a)	0.23 ± 0.04	Bounding limits	$\leq 1.4\text{x}10^{19}$ (b)	≥ 8 (c)	$0.002 - 0.6$	$23 - 29$
				Lake-Thomas	$5.0\text{x}10^{17}$	73.0 ± 0.8 (d)	0.060 ± 0.002	26.6 ± 0.03
Underwater	20	0.18 (a)	0.012 (e)	Bounding limits	$\leq 1.4\text{x}10^{19}$ (b)	≥ 8 (c)	0.08 – 6	27 – 31
				Lake-Thomas	$5.0\text{x}10^{17}$	19 ± 4 (d)	3 ± 1	30.3 ± 0.6

(a) From [28, 168, 169], (b) from[87, 166, 167], (c) from [58, 62, 163-165], (d) fitted, and (e) calculated in **SI section 4.7.7**.

Based on the upper limit on Σ and the lower limit on M, the bond lifetime is between 0.002 s ≤ τ ≤ 0.6 s. A bond lifetime on the order of milliseconds to seconds is orders of magnitude higher than what would be expected for individual hydrogen bonds. As a comparison, the lifetime of a single hydrogen bond is estimated to be O(ps – ns).[158, 170] The long bond lifetime is consistent with cooperative hydrogen bonding. Using Eyring's equation (**Eqn. 4.2**), the equilibrium activation energy of the bond is estimated to be $23k_BT \leq E_a \leq 29k_BT$. We refine these bounds further using the Lake–Thomas theory to obtain an estimate of $\Sigma \approx 5.0 \times 10^{17}$ #/m^2 (see Supplementary Information **Section 4.7.4**). [59] Using the Lake–Thomas value for Σ gives $\tau = 0.060 \pm 0.002$ s and $E_a = 26.6 \pm 0.03k_BT$, with error bounds calculated through the standard error of the data.

To put these values for E_a in context, if the three Tris alcohols acted independently of each other during debonding, the number of bonds per unit area would increase threefold as a single Tris group will have three individual bonds with the mica surface. However, the lifetime would be that of a single hydrogen bond, of O(ns), corresponding to activation energies of $\sim 10k_BT$. In contrast, if the three hydroxyls act cooperatively and must debond from the surface at once, a simple addition of the individual activation energies for each −OH group will give $E_a = 3k_BT$

corresponding to τ = 1.7 s. These estimates for the simultaneous (cooperative) detachment of three hydrogen bonds are very close to the values we obtained in our experiments.

4.5.3 Underwater Adhesion Measurements

We then characterize the adhesion of films of DGEBA–Tris oligomer in water using the SFA. The geometry of these measurements approximates a sphere-on-flat contact, as shown in **Figure 4.7**. With this technique, we simultaneously measure the surface separation D (or indentation depth δ), contact radius a, crack velocity (u), and force F. Force values are normalized by the radius of curvature R to obtain an interaction energy. The geometry at the crack tip is analogous to the one in the self-arrested crack measurements. We focus on interactions between oligomeric DGEBA–Tris and mica or aluminum due to the pronounced increase in adhesion with crack velocity measured in air. In contrast to previous work with DGEBA–Tris that studied the water-induced degradation of adhesive bonds that were formed in air,[159] here we both form and break the adhesive bonds underwater.

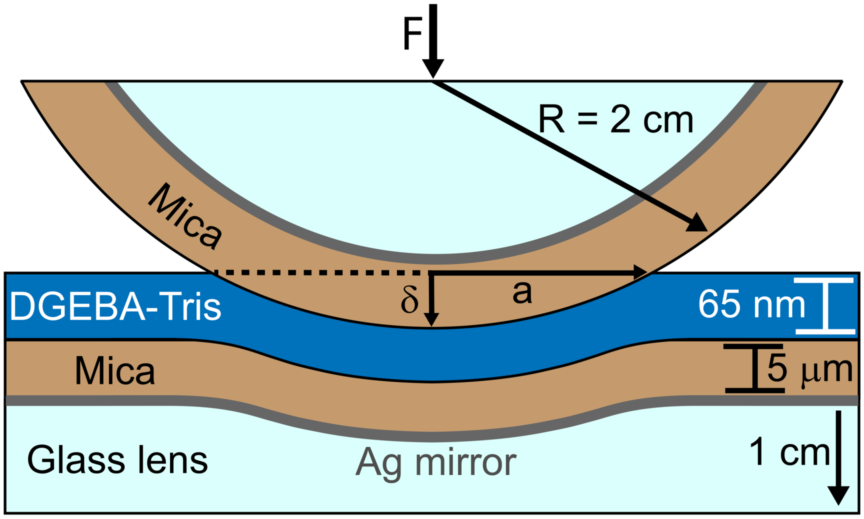

Figure 4.7 Diagram of SFA configuration. Schematic of the geometrical configuration for SFA adhesion measurements, where F is the force between the disks, a is the contact radius, and δ is the indentation depth. Not to scale.

We first characterize the interactions between the DGEBA–Tris film and mica as the surfaces approach and make contact. For samples in a dry N_2 atmosphere, no forces are measured until attractive forces cause a spring instability and jump into contact. In contact, the DGEBA–Tris film thickness is measured to be 61–75 nm, the variability coming from different experiments. During the approach in water, we first observe a long-range repulsive force starting at ~80 nm away from contact (**Figure 4.8a**), attributable to electrostatic double-layer repulsion (see Supplementary Information **Section 4.7.5**).[28] This is followed by a steep repulsion, which we ascribe to contact (and compression) with the swollen DGEBA–Tris film. The surfaces are compressed until we reach the set point of $F/R = 0.3$ N/m (~5 mN), and use the separation at this set point to define contact in water (zero separation). By convention, we assign positive signs for compressive forces and negative signs for tension (adhesion). In water, the first contact with the swollen DGEBA–Tris occurs 5–15 nm away from contact in dry N_2. Based on these values and the thickness of the dry films obtained from interferometry measurements before water was added to the system, we estimate the degree of swelling in water to be 17 ± 10%. Once the force set point of 0.3 N/m is reached, the films return to their initial dry thickness. We attribute this change in film thickness to the removal of most of the water in the film within the contact region during compression. Prior to detachment, the surfaces are kept at $F/R = 0.3$ N/m for 5 min. During this dwell period, the thickness of the DGEBA–Tris changes only by 0–2 nm, and the final thickness is reached within 200 s of dwell.

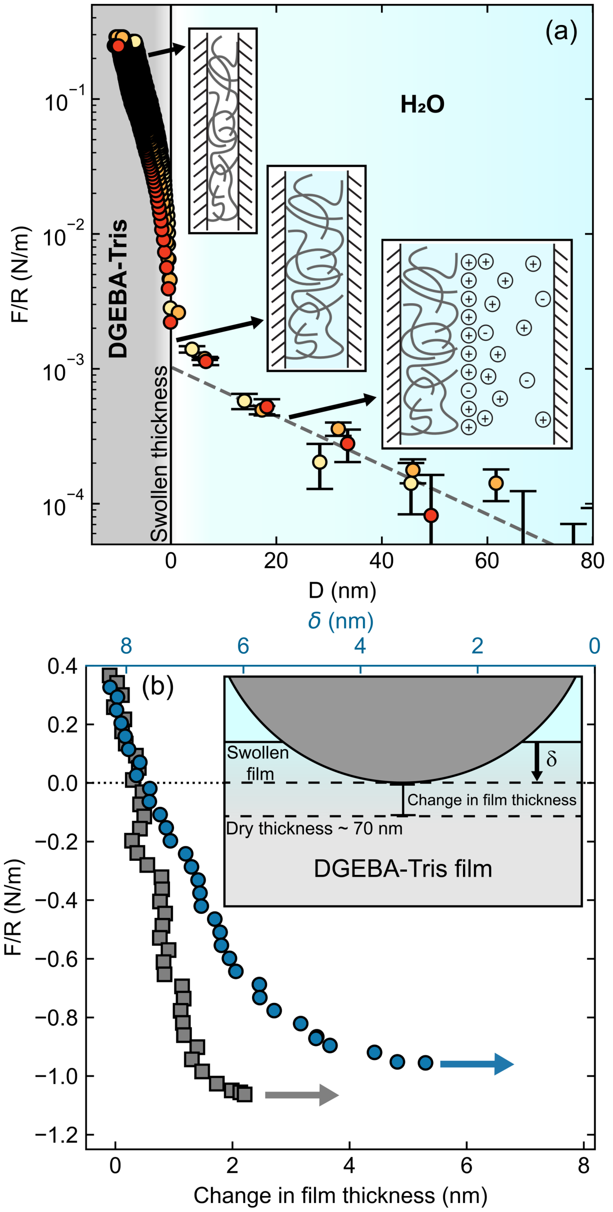

Figure 4.8 Forces during approach and retraction in adhesion measurements. (a) Measured force (normalized by the radius of curvature) vs surface separation *D* for three different samples approaching contact in water. Zero separation is set at the onset of the steric repulsion. Cartoons indicate the processes that occur during the approach, from right to left: electrostatic double-layer repulsion; contact with swollen film; deswelling and elastic compression of film. (b) Retraction force (normalized by the radius of curvature) vs change in film thickness in dry nitrogen (gray squares) and water (blue circles) at comparable velocities (23–26 nm/s). The top *x*-axis is added to show the underwater film indentation depth (δ) for swollen films (blue circles only), where zero is defined as the swollen film thickness as was done in the *x*-axis in (a).

Adhesion between the surfaces builds up in contact during compression and dwell. During dwell, the contact area increases continuously, consistent with a buildup of adhesive interactions. After 5 min of dwell, the surfaces are pulled apart at a constant drive velocity until detachment, which occurs through a jump-out instability. In N_2, adhesive failure occurs at less than 3% strain, while in water, the film does not stretch beyond the equilibrium swollen thickness during retraction. Failure appears to be adhesive, but we cannot rule out the possibility of some small transfer to the other surface.[171] After detachment, we do not observe significant changes either in the surface profile or in the contact region if we make subsequent contact at the same spot, consistent with adhesive failure. We did, however, notice that the pull-off force would decrease if we measured adhesion multiple times at the same spot, likely due to some damage or changes in the surface. Therefore, contact spots were changed for each measurement.

Adhesion in dry N_2 and water, as characterized by the adhesive strength (F_C, pull-off force), is surprisingly similar (**Figure 4.8b**). We utilize the JKR relationship in the limit of an elastic half-space (see Supplementary Information **Section 4.7.6** for applicability) to relate the critical strain energy release rate G_c to the pull-off force through[32, 40]

$$\frac{F_C}{R} = \frac{3}{2}\pi G_C. \tag{4.4}$$

Eqn. 4.4 is only valid at the point of adhesive failure where $G = G_c$ by definition. The DGEBA–Tris films investigated here are highly confined, $a/h \sim 90$, and in this limit, **Eqn. 4.4** can lead to errors of up to 30%.[135, 172] We assume that the error is similar across samples because they all have relatively the same degree of confinement as well as comparable glue and mica thicknesses. A complex analysis of the multilayered system compliance would be necessary to precisely correct for confinement in the SFA.[135, 172]

The adhesion of DGEBA–Tris oligomers in water is as strong as that in dry N_2 (**Figure 4.9**). In N_2, G_c = 0.19 ± 0.01 J/m^2 for contact between DGEBA–Tris and mica, while in water, it is G_c = 0.23 ± 0.05 J/m^2. This is remarkable since, typically, underwater adhesion is much weaker than that in air because of lower van der Waals interactions.[86, 173] Surface enrichment of Tris groups in water could help make up for the weakened van der Waals forces, and swelling of the film could facilitate contact area in water. We further investigate the adhesion of DGEBA–Tris oligomers with ultra-smooth aluminum films.[26] These films have a natural Al_2O_3 layer on the surface, which should give them a higher density of hydrogen-bond-accepting groups than mica.[174] Adhesion of DGEBA–Tris films with aluminum also remains strong underwater with G_c = 0.18 ± 0.03 J/m^2 in N_2 and G_c = 0.23 ± 0.03 J/m^2 in water. The similarity in adhesion may indicate that we are more limited by the density of Tris moieties than by hydrogen-bond-accepting groups on the opposing surface.

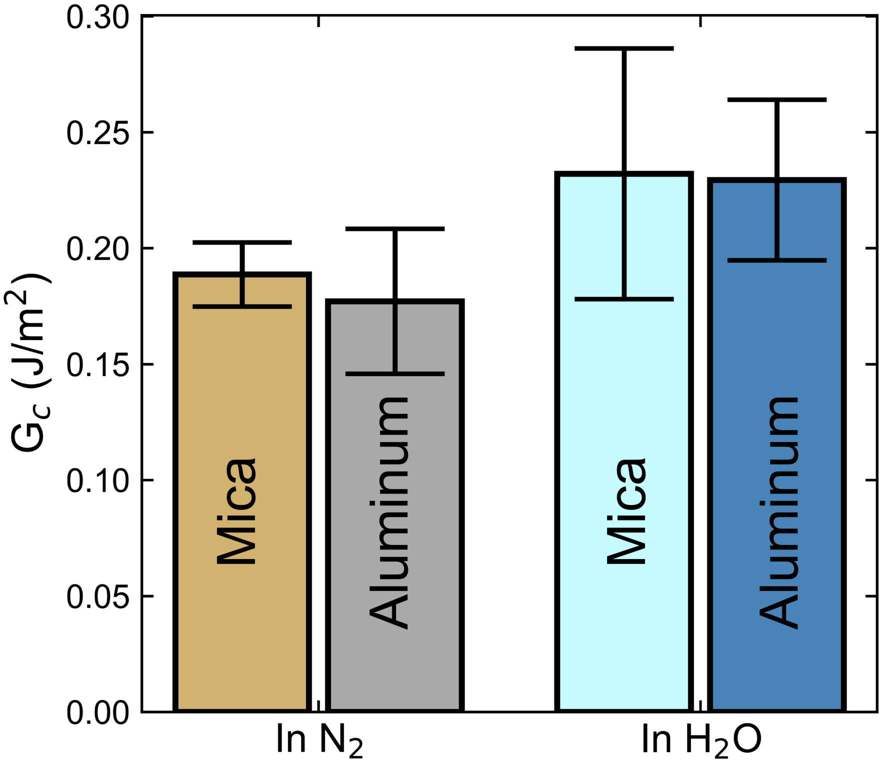

Figure 4.9 Adhesion of DGEBA–Tris with mica or aluminum in N_2 and in water. Average critical energy release rate for the adhesion of DGEBA–Tris oligomers to mica or aluminum surfaces in dry N_2 or in water. No loss of adhesion is seen when contact is made in water. Retraction velocities were 23–35 nm/s for contact with mica and 5–10 nm/s for contact with aluminum.

To investigate the rate-dependent adhesion in water, we extract the instantaneous radial velocity during debonding from the interference fringes. The radial velocity $u_r = -\mathrm{d}a/\mathrm{d}t$ is nearly constant during most of the retraction; then, as we approach the pull-off force, the radial velocity increases rapidly until the surfaces jump out of contact. To obtain $u_{r,c}$ at pull-off, we rely on $\mathrm{d}a/\mathrm{d}t$ calculated over the last 1 μm change in contact radius. We then obtain an estimate for G_0 by assuming that the only rate-independent interactions are those caused by van der Waals forces (see Supplementary Information **Section 4.7.7**). By using the Lifshitz method for estimating non-retarded Hamaker constants,[28] known parameters for mica and water,[28, 86] and refractive index and dielectric permittivity for the oligomer from ellipsometry measurements and literature,[175] respectively, we estimate the van der Waals adhesion of DGEBA–Tris oligomer and mica in water to be 12 mJ/m^2. This estimated G_0 is much lower than the smallest measured G_c (79 mJ/m^2). Therefore, an error of $O(1)$ on this estimate will not impact the magnitude of the $G_c - G_0$ term.

As for measurements in air, adhesion between DGEBA–Tris oligomers and mica is stronger as the crack velocity increases (**Figure 4.10a**) and follows the scaling expected for the breaking of interfacial bonds (**Eqn. 4.1**). The values of $\sqrt{G - G_0}$ are larger in water than in air, partially because the weaker van der Waals contributions in water render G_0 an order of magnitude weaker in water. The slope of $\sqrt{G - G_0}$ vs $\ln(u)$ is slightly higher in water than in air, and the intercept occurs at a slower velocity. The discrepancy in geometry and errors, for example, due to confinement, in the measurement of $u_{r,c}$ and G_c in the SFA could explain this difference. Given the critical nature of the failure in the SFA, it is more challenging to capture $u_{r,c}$ than the stable u measured through self-arresting crack propagation. It is also possible that swelling of the epoxy film and surface enrichment of Tris groups could enhance adhesion compared to the dry case and will be the subject of future investigations.

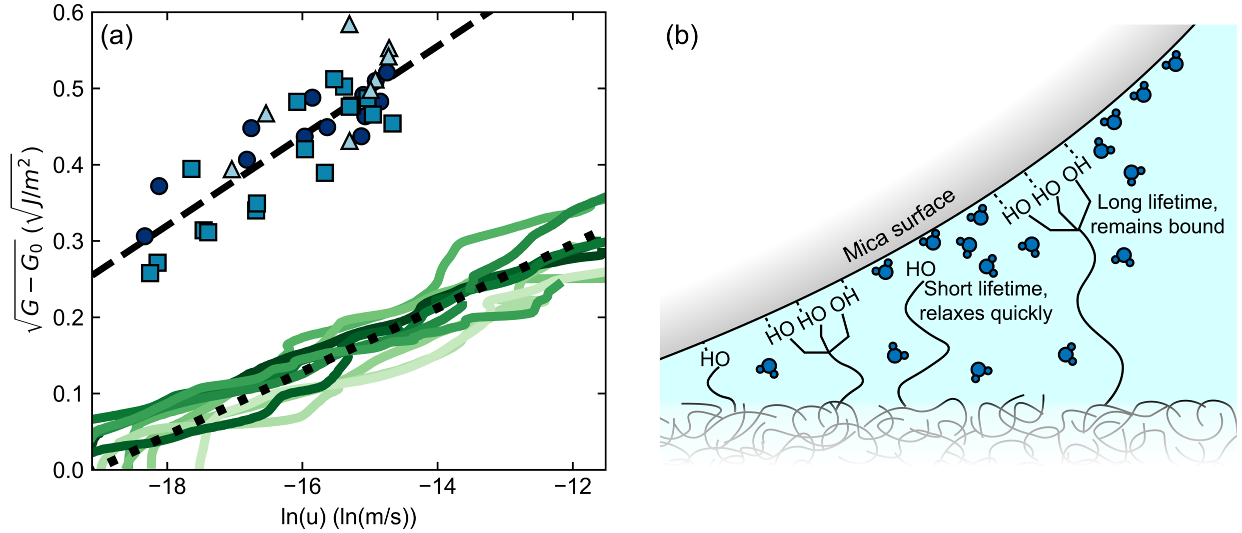

Figure 4.10 Rate dependence of energy release rate reveals cooperative H-bonding in air and water. (a) Difference between the measured critical strain energy release rate, G, and the energy release rate G_0 as a function of the crack velocity (u). Interfacial crack propagation water with the SFA is shown as blue symbols (different colors/shapes indicating separate samples), where $G = G_c$ and $u = u_{r,c}$. Self-arresting crack measurements in air are shown as green lines. The dashed line indicates a fit of measurements in water ($R^2 = 0.72$) to **Eqn. 4.1**, while the dotted line shows the aggregated fit to self-arresting crack measurements in air. (b) Schematic illustrating the proposed cooperative debonding mechanism where cooperative hydrogen bonds have a significantly longer bond lifetime and contribute strongly to underwater adhesion where the adhesive strength depends strongly on crack velocity.

We follow the same approach as for the measurements in air to obtain estimates of the bond lifetime for the adhesion measurements between DGEBA–Tris and mica in water. Using the same limiting values of Σ and M listed in **Table 4.1**, we estimate the bond lifetime in water to be between $0.08\ \text{s} \leq \tau \leq 6\ \text{s}$, leading to an equilibrium activation energy of $27k_BT \leq E_a \leq 31k_BT$. Using the Lake–Thomas value of Σ yields, $\tau = 3 \pm 1$ s and $E_a = 30.3 \pm 0.6k_BT$. These values, while higher, are remarkably similar to the measurements in air, especially given differences in geometry, environment, and experimental protocol. We thus conclude that similar binding kinetics occur in water and in air, and the values suggest that tridentate H-bonding contributes to adhesion in both cases.

Our observations are in qualitative agreement with prior work on cooperative debonding in adhesion. In particular, several single-molecule studies have obtained lifetimes of O(ms) for multidentate hydrogen bonding in Dopa and between UPy groups.[57, 157, 169] These force microscopy experiments showed stronger hydrogen-bonding interactions when multiple −OH groups are involved, and that cooperativity substantially increases the lifetime of the bond. Here, we see an analogous effect but in macroscale adhesion measurements.

The proposed cooperative debonding mechanism is illustrated in **Figure 4.10b**. The measured adhesive strength and its dependence on crack velocity cannot be obtained by the debonding of a larger number of individual (and independent) hydrogen bonds. One possible explanation as to why the Tris moieties lead to cooperativity could be that anchoring of an individual (or two) −OH group(s) in the Tris moiety restricts the movement of the third group on the surface. The hindered mobility on the surface could encourage rapid rebinding and longer effective bond lifetimes for the whole moiety. A similar mechanism has been suggested by molecular dynamics simulations of Dopa molecules interacting with alumina surfaces in water.[176] This enhanced binding affinity could help explain the ability of Tris-modified epoxies to maintain their adhesion strength in the presence of water.[83] For individual hydrogen bonds, interfacial water will compete for surface binding sites and interact with hydroxyl groups in the adhesive,[17, 177, 178] shifting the binding equilibrium and drastically lowering the number of adhesive hydrogen-bonding interactions and thus the total adhesive force of the system.[17, 179] However, if the tridentate bonds are more strongly anchored to the opposing surface, the binding equilibrium would be less disrupted by interfacial water, allowing a higher number of Tris groups to remain bound and maintaining the adhesive strength.[158] Additionally, computational studies have shown that the adsorption of catechols to a hydrated interface and subsequent displacement of interfacial water is energetically favorable.[180, 181] A similar mechanism could allow Tris groups to form adhesive bonds even in the presence of interfacial water. However, the ability to form tridentate interactions could be strongly dependent on the density of hydrogen-bonding sites on the opposing surface, with less dense surfaces not allowing for three interactions within the reach of the three arms of the Tris moiety.[158]

4.5.4 Alternative Mechanisms

We also rule out bulk dissipation in the form of viscoelasticity or film stretching as a possible cause for the increase in adhesion with crack velocity. The observed rate dependence occurs at velocities that are slower than those typically observed for bulk viscoelastic dissipation. The widely used semi-empirical model for viscoelastic rate dependence, $G = G_0\left(1 + \left(\frac{v}{v^*}\right)^n\right)$, attributes an increase in adhesion to dissipation during extension, and thus higher values of G are typically correlated with increased extension during detachment.[43, 70] Instead, the opposite trend occurs in our SFA measurements: at higher loading rates, lower extension is seen, even though G

increases. Overall, we see minimal extension (<8 nm) in our films and therefore expect that bulk dissipation in the film is negligible. The SFA measurements also allow us to confirm the validity of **Eqn. 4.3** for our peeling measurements. **Eqn. 4.3** assumes that there is minimal deformation in the film during detachment and that the substrate is rigid. With a similar film thickness, our SFA measurements reveal <8 nm of stretching in all cases, and the fracture appears to be interfacial. Any deformation in the film is clearly minimal in comparison to the bending of the top sheet, and thus the bending can be modeled as the flexure of an elastic plate.

4.6 Summary

Adhesion of model epoxy oligomers modified with tridentate hydroxyl groups (DGEBA–Tris) with mica was investigated in air and in water. We showed that the critical strain energy release rate of DGEBA–Tris epoxies scales with the crack velocity according to Chaudhury's rate-dependent fracture model,[69] and that control experiments with epoxies that do not contain the Tris moiety showed no dependence on adhesion with crack velocity. Our data suggests that adhesion involving DGEBA–Tris films is due to long-lived interfacial interactions by Tris groups. We also found that the pull-off force of DGEBA–Tris and mica was maintained in the presence of water (F/R = 0.94 ± 0.3 N/m in water vs 0.89 ± 0.16 N/m in N_2 for comparable detachment velocity). DGEBA–Tris also showed sustained adhesion with aluminum films in air and water. In addition, adhesion in water also increases with an increase in detachment velocity. By placing conservative limits on molecular parameters, we estimate that the lifetime of these interfacial bonds is between 0.002 and 0.6 s in air and between 0.08 and 6 s in water, corresponding to a bond activation energy of between 23 and 29 k_BT in air and between 27 and $31k_BT$ in water. These lifetimes and activation energies are consistent with three hydrogen bonds working cooperatively to form a single, robustly bonded group that resists displacement by interfacial water. We propose that the enhanced lifetime of this bond is responsible for its strong underwater adhesion. These findings provide quantitative insight into the connection between the molecular physics and macroscale adhesion of epoxy adhesives containing multidentate hydrogen-bonding moieties and suggest a mechanism via which the use of such groups could be used to overcome the detrimental impacts of interfacial water on adhesion in real-world applications.

4.7 Supplementary Information

4.7.1 Diagram of Surface Forces Apparatus (SFA)

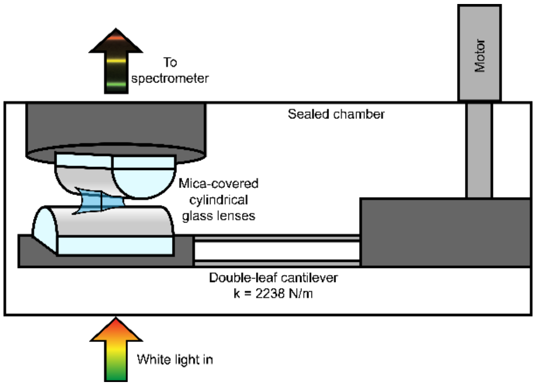

Figure S4.11. Diagram of SFA. Diagram detailing the configuration of the SFA used for these measurements. One hemi-cylindrical lens is mounted on a double-leaf cantilever, while the other is fixed to a stationary top mount. A microstepping motor allows for positioning of the bottom lens to apply forces. A water drop is injected between the surface to form a capillary and submerge the contact region. Extensive diagrams of the SFA can be found elsewhere in literature.[130] Diagram is not to scale.

4.7.2 Variabilty in adhesion of cured DGEBA-Tris

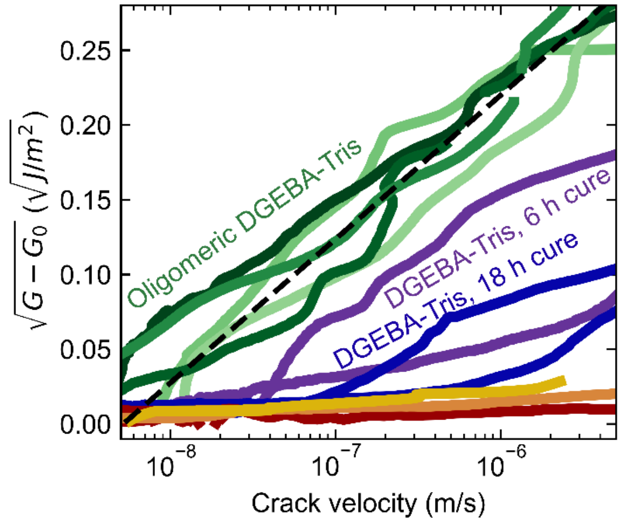

Figure S4.12. Variability in adhesion dynamics. Scaled energy release rate vs crack velocity for bare H^+ mica (orange), oligomeric DGEBA-Tris (green), DGEBA-Tris cured for 6 h (purple) or 18 h at 150 °C (blue), and DGEBA-355 (yellow) and DGEBA-1750 (red), both cured for 18 h at 150 °C. Cured DGEBA-Tris reliably exhibits enhancement of adhesion with crack velocity with a higher onset velocity than for oligomeric DGEBA-Tris.

4.7.3 Calculation of oligomeric spring constant

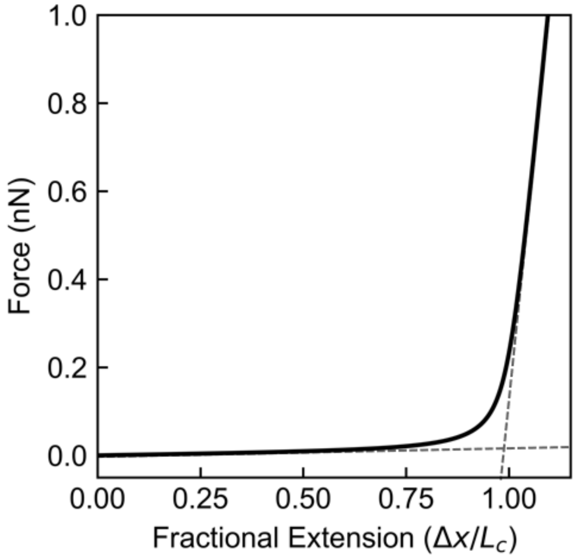

Figure S4.13. Estimated force-extension relationship for a DGEBA-Tris oligomer. Force vs estimated fractional extension ($\Delta x/L_c$) for a DGEBA-Tris oligomer, using **Eqn. S1** with $l_k \approx$ 0.78 nm, n = 2.83, and $K_{total} \approx$ 5 N/m. The lower asymptote corresponds to a minimum entropic spring constant of 8 mN/m, while large extension is dominated by bond deformation, giving an upper limit of K_{total}.

In order to estimate the force-extension relationship for the complex DGEBA-Tris oligomer, we compare segments of the DGEBA-Tris molecule to the stretching behavior of chains in literature. While several models for the force-extension relationship of a polymer exist,[62] we choose to use the modified-Freely Jointed Chain (m-FJC) model due to plethora of literature employing this model and reporting parameters for various polymer chemistries. The m-FJC is given by:[62]

$$\Delta x = \left[\coth\left(\frac{Fl_k}{k_BT}\right) - \frac{k_BT}{Fl_k}\right]\left(L_c + \frac{nF}{K_{segment}}\right). \tag{S4.5}$$

In this model Δx is the extension of the chain, l_k is the Kuhn length of each segment in the chain, L_c is the contour length of the chain, n is the number of Kuhn segments, and $K_{segment}$ is the stiffness of each segment. The aromatic section of the DGEBA molecule can be estimated to have $l_k \approx$ 0.87 nm and $K_{aromatic} \approx$ 960 N/m by comparison to the stretching similar polymers in literature.[163] The linear aliphatic section of the DGEBA-Tris molecule is estimated to have $l_k \approx 0.72$ nm and $K_{aliphatic} \approx 7.6$ N/m by similar comparison to alkane and PEG chains in literature.[58, 157, 164, 165]. A simple weighted average approximates the chain as 2.52 segments of $l_k \approx$ 0.78 nm, giving L_c = 1.97 nm, and adding the stiffness of each segment in series gives $K_{total} \approx$ 5 N/m. Using these values, the estimated force-extension relationship of the oligomer is shown in **Fig. S4.13**. At low extension, the oligomer is predicted to stretch entropically with a minimum spring constant (dF/dx) of 8 mN/m. At large values fractional extension, the deformation of bonds becomes significant with the spring constant asymptotically approaching $K_{total} \approx 5$ N/m. The effective spring constant M of the oligomer must fall between these limiting values. We note that the prediction *a priori* of a force-extension relationship, especially for a complex oligomer, is challenging. However, these limits represent extreme conditions, and the estimates of M from other studies give values on O 0.1 N/m, well within our range.

4.7.4 Estimation of chain density through Lake-Thomas theory

Lake-Thomas theory states that the number of chains crossing a plane can be calculated through[59]

$$\frac{\text{\# of chains}}{\text{unit area}} = \frac{1}{2}\sqrt{\frac{8n}{3\pi}}\, l_k N. \qquad \text{(S4.6)}$$

Here N is the chain number density and l_k and n are the Kuhn length and number of Kuhn segments, respectively, for the chain. We approximate that $\Sigma \approx \frac{\text{\# of chains}}{\text{unit area}}$ at the fracture plane, and then use the values of l_k and n found in **Section 4.7.3** with $N \approx 8.72\text{x}10^{26}$ chains/m^3 to obtain $\Sigma \approx 5.0\text{x}10^{17}$ Tris groups/m^2.[182] This assumes that all Tris groups at the interface are bound and thus likely overestimates Σ, which therefore underestimates τ and E_a. As we are attempting to ascertain if E_a is of $\mathcal{O}(10k_BT)$ or of $\mathcal{O}(30k_BT)$, underestimating E_a to be between 23 k_BT - 31 k_BT does not alter our conclusions.

4.7.5 Analysis of double layer repulsion

In SFA experiments when samples are brought together in water a long-range repulsive force is measured before contact is made. These long-range forces measured at separation > 80 nm are consistent with double layer repulsion. The force decays exponentially with an increase in surface separation (**Fig. 4.8a**) and a Debye length of $\kappa^{-1} = 24 \pm 3$ nm. The ionic concentration of the solution can be estimated from the Debye length as $1.6\text{x}10^{-4} \pm 0.2\text{x}10^{-4}$ M, assuming a symmetric 1:1 electrolyte.[28] This is a higher concentration than the ~ 10^{-5} M expected for DI water in equilibrium with atmospheric CO_2, suggesting that there could be additional ionic species from sample preparation steps or the DI water or multivalent ions present. We can also compare our data to the force expected for the interaction between electrostatic double layers using the non-linear superposition and the Derjaguin approximation: [28]

$$\frac{F}{R} = \kappa\left[64\pi\epsilon\epsilon_0\left(\frac{k_BT}{e_c}\right)^2 \tanh\left(\frac{e_c\,\psi_{mica}}{4k_BT}\right)\tanh\left(\frac{e_c\,\psi_{DGEBA-tris}}{4k_BT}\right)\right]\exp(-\kappa D). \qquad \text{(S4.7)}$$

Here F is the force, R is the radius of curvature of the sample, D is the separation between the surfaces, e_c is the elementary charge, $\epsilon\epsilon_0$ is the dielectric permittivity of the medium (i.e. water), and ψ_{mica} and ψ_{tris} are the surface potentials of the mica and DGEBA-Tris surfaces, respectively. By using a previously measured value of $\psi_{mica} = -150$ mV,[26] we estimate the surface potential of the DGEBA-Tris film to be $\psi_{DGEBA-tris} = -31 \pm 5$ mV.

4.7.6 Use of JKR equation

The Johnson-Kendall-Roberts (JKR) equation relates the force to the contact area for in the contact of a sphere-on-flat geometry.[40]

$$a^3 = \frac{3R}{4E^*}(F + 3\pi GR + (6\pi GRF + (3\pi GR)^2)^{\frac{1}{2}}. \qquad \text{(S4.8)}$$

Here a is the contact radius, F is the force, R is the radius of curvature, E^* is the reduced elastic modulus of the sample, and G is the strain energy release rate. The JKR relation is applicable in the limit of soft, large radius of curvature, and highly adhesive materials that don't interact outside of contact. Both Tabor and Maugis developed parameters describing the transition from the JKR limit to the opposing regime, described by the Derjaguin-Muller-Toporov (DMT) equation.[41] The Tabor parameter is given by:[135]

$$\mu \equiv \left(\frac{RG^2}{E^{*2} z_0^3}\right)^{\frac{1}{3}}, \qquad \text{(S4.9)}$$

where z_0 is the equilibrium surface separation. If $\mu \gg 1$, the samples will be in the JKR limit. With z_0 estimated as 0.2 nm, and effective modulus of the system $E^* = 6$ GPa,[135], and our lowest adhesion energy of $G = 79$ mJ/m^2, $\mu = 69$. Even with $z_0 = 1$ nm, the RMS roughness of our DGEBA-Tris films after 24 hours in water, $\mu = 14$ and the condition is still satisfied.

The Maugis parameter is given by:[41]

$$\lambda \equiv \frac{2\sigma_0}{\left(\frac{16\pi G E^{*2}}{9R}\right)^{\frac{1}{3}}}, \qquad \text{(S4.10)}$$

where σ_0 is the yield stress of the material. The JKR limit is reached as $\lambda \to \infty$, but values of $\lambda > 5$ give only small deviations from the JKR equation.[41] If we approximate $\sigma_0 \approx 1.03\frac{G}{z_0}$,[41] the previously used values of z_0 give $\lambda = 80$ and $\lambda = 16$, respectively. Both values are indicative of JKR-like mechanics.

The final assumption of the JKR equation, that there is no interaction outside of the contact region, is violated by the electrostatic repulsive forces that we measure on approach (*c. f.* **Fig. 4.8**). However, as these forces are at a maximum $\frac{F_{electrostatic}}{R} \approx 1$ mN/m, while the adhesive forces are at minimum 370 mN/m at pull-off, we expect deviation from JKR due to electrostatic repulsion to be small.

4.7.7 Estimation of G_0 in water

To estimate the rate-independent strain energy release rate in water we first assume that all rate-independent interactions are due to van der Waals forces. In this system, interactions of DGEBA-Tris with mica across water as well as the interaction of the underlying mica substrate with water across the thin DGEBA-Tris film. The energy of this interaction is given by:[28]

$$G_{vdW} = -\frac{1}{12\pi}\left[\frac{A_{132}}{D^2} - \frac{A_{213}}{(D+H)^2}\right]. \qquad \text{(S4.11)}$$

In this equation, A_{132} is the Hamaker constant of material 1 interacting with material 2 across medium 3, where 1 is DGEBA-Tris, 2 is mica, and 3 is water. D is the separation between the DGEBA-Tris film and the opposing mica surface, while H is the thickness of the DGEBA-Tris film. The Hamaker constants can be estimated using Lifshitz theory.[28]

$$A_{132} \approx \frac{3}{4} k_B T \left(\frac{\varepsilon_1-\varepsilon_3}{\varepsilon_1+\varepsilon_3}\right)\left(\frac{\varepsilon_2-\varepsilon_3}{\varepsilon_2+\varepsilon_3}\right) + \frac{3h\nu_e}{8\sqrt{2}} \frac{(n_1^2-n_3^2)(n_2^2-n_3^2)}{(n_1^2+n_3^2)^{\frac{1}{2}}(n_2^2+n_3^2)^{\frac{1}{2}}\left[(n_1^2+n_3^2)^{\frac{1}{2}}+(n_2^2+n_3^2)^{\frac{1}{2}}\right]} \qquad \text{(S4.12)}$$

In this equation, k_B is Boltzmann's constant, T is the temperature (20 °C), ε_1 is the dielectric permittivity of material 1 (DGEBA-Tris), h is Planck's constant, ν_e is the electronic absorption frequency (assumed to be 3x10^{15} s^{-1}), and n_1 is the refractive index of material 1. We use literature values for the dielectric permittivity of mica and water,[28, 86] the measured value of the refractive index of DGEBA-Tris (see methods section in main text), and an estimate of the dielectric permittivity of DGEBA-Tris from literature.[175] These parameters are summarized in **Table S4.2.** For a contact $D = 0.2$ nm, **Eqns. S4.11** and **S4.12** estimate that $G_{vdW} \approx 12$ mJ/m^2.

Table S4.2. Parameters used in Eqn. S4.11 and S4.12 to calculate G_{vdW}.

T °C	ν_e ^{b} s^{-1}	ε_1 ^{a}	ε_2 ^{b}	ε_3 ^{b}	n_1	n_2 ^{b}	n_3 ^{b}	A_{132} J	A_{213} J	H nm
20	3x10^{15}	16	6.2	80	1.582	1.60	1.333	1.85x10^{-20}	0.23x10^{-20}	70

(a) From [175], (b) from [28].

4.7.8 Poroelastic flow during retraction

Following the procedure of Delavoipiere *et al.,* the force due to fluid flow into or out of a porous material during compression or extension can be modeled as:

$$F_H = \frac{\pi}{8H}\left(\frac{\dot{\delta}\eta a^4}{\kappa}\right) \qquad \text{(S4.13)}$$

Here F is the force on the indenter, a is the contact radius, δ is the indentation depth, $\dot{\delta}$ is the indentation rate, H is the film thickness, η is the dynamic viscosity of the solvent, and κ is the permeability of the film. By using measured values of a and $\dot{\delta}$, we can estimate the force due to fluid infusion for various values of η/κ and compare them to the measured forces at various retraction velocities. **Fig S4.14** shows that for commonly used values of η/κ (purple, $\eta = 8.9\text{x}10^{-4}$ Pa s and $\kappa = 1\ \text{nm}^2$),[97] the estimated force due to fluid infusion is negligible. Only when η/κ is increased by over 6 orders of magnitude (orange, $\frac{\eta}{\kappa} = 1.8\text{x}10^{21}$ Pa s/m^2) is the force significant in comparison to the measured forces (blue, green, and red points), and decreases sharply near pull-off as a decreases. Qualitatively, our measured forces do not agree with this model, and the unreasonable values of η/κ needed to produce forces in the range of our measurements indicates that fluid infusion is unlikely to affect our measured forces significantly.

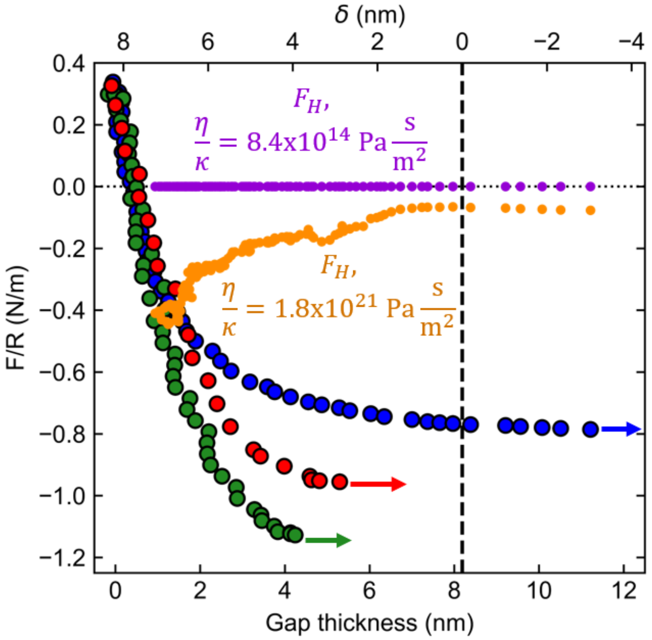

Figure S4.14. Estimated fluid-infusion force during retraction in water. Force normalized by radius of curvature for estimated force due to fluid infusion during retraction using **Eqn. S4.13**, with literature values for $\frac{\eta}{\kappa} = 8.4\text{x}10^{14}$ Pa s/m^2 (purple) and extreme values needed to model indentation curve $\frac{\eta}{\kappa} = 1.8\text{x}10^{21}$ Pa s/m^2 (orange). For $\delta > 7.2$ nm (Gap thickness < 1 nm), $\dot{\delta}$ is below our measurement sensitivity and is therefore not plotted. Data is overlayed onto the measured curves for the three different retraction velocities with $V_{motor} = 11$ nm/s (blue), $V_{motor} = 24$ nm/s (red), and $V_{motor} = 71$ nm/s (green), to facilitate comparison. Even if unreasonable values of η/κ are used, the estimated porous infusion force decays near pull-off due to sharp decreases in a.

5 Temperature, cure, and velocity dependence of adhesion yields insight into interfacial behavior of multidentate hydrogen bonding adhesives.

5.1 Abstract

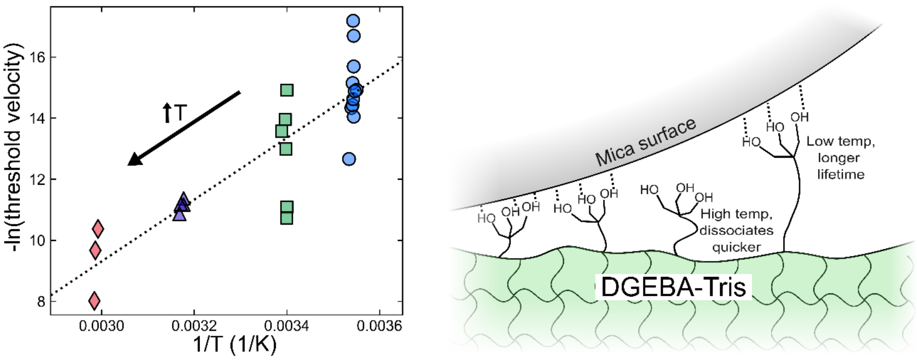

Figure 5.1. **Schematic depicting a summary of Chapter 5:** Left: negative natural logarithm of the threshold velocity for adhesion amplification of DGEBA-Tris vs the reciprocal of temperature, showing the anticipated linear dependence. Right: proposed mechanism by which increased thermal energy leads to more rapid dissociation of cooperative hydrogen bonds.

Adhesives containing multidentate hydrogen bonding moieties are gaining prominence for their ability to adhere strongly underwater. Previous studies attributed their remarkable underwater adhesion to the multiple adjacent attachment points within a moiety stabilizing the bond, enabling more robust adhesion underwater. However, as adhesion involves multiple coupled phenomena, isolating the contribution of individual bonds to the adhesive strength is challenging. Therefore, additional studies are needed to understand the mechanisms behind the strong underwater adhesion of multidentate hydrogen-bonding moieties. Here we investigate adhesion of a model epoxy modified by the addition of tridentate hydrogen bonding moieties (DGEBA-Tris). We report on the effect of curing, debonding temperature, and crack velocity on the adhesive strength of the DGEBA-Tris/mica interface. As expected, at a given temperature the energy release rate increases with crack velocity above a characteristic threshold velocity. We observe very large change in the threshold velocity across the parameter space investigated. The threshold velocity increases by two orders of magnitude upon curing, likely due to a decrease in the polymer stiffness associated with increasing molecular weight. For cured samples, increasing the temperature from 9 – 60 ºC leads to an increase in the threshold velocity by two orders of magnitude. The increase in threshold velocity with an increase in temperature follows an Arrhenius dependence revealing a bond activation energy of 14 ± 2 x10^{-20} J ($35 \pm 4\, k_B T$ at 20 ºC). The bond energy and associated temperature dependence suggest that adhesion is dominated by cooperative tridentate hydrogen bonds, and that adhesive fracture of these bonds proceeds through an activated process.

5.2 Introduction

Structural adhesives are routinely required to operate at extreme temperatures in the aerospace and transportation industries.[83, 183-186] The effect of temperature on fracture strength has been investigated for a wide range of polymer properties – including molecular weight,[51] glass transition temperature,[187] ductility,[8] rheological behavior,[188] shrinkage stress during cure,[189] and even moisture ingress[190]. Additionally, adhesives are commonly tested through accelerated aging at elevated temperatures,[83, 190] thus understanding the behavior of adhesives at increased temperatures is important for the design of stronger and more robust adhesives. Adhesives containing multidentate groups enhance interfacial strength of existing adhesives, particularly in harsh, underwater environments.[156, 159, 191] It is believed that multidentate groups are more energetically and sterically stable at an interface, and therefore are able to bind even in the presence of water.[154, 158, 159] However, relying upon these dynamic interfacial bonds necessitates that we improve our understanding of their interfacial bonding mechanism, especially in connecting the specific multidentate moieties to macroscale adhesive strength.

Recent advances in connecting molecular and macroscale adhesion have come through modeling adhesive fracture as a chemical reaction-like process, where the bonds must pass through an activated transition state to rupture. Schallamach laid the groundwork for this theory, showing that the sliding velocity of rubber follows an Arrhenius-like dependence on temperature.[73] Later innovations by Chaudhury and others came by connecting the strength of an individual bond to the rate at which force is applied to the bond through a polymer chain, and then summing up the individual bond energies to yield an adhesive strength.[24, 56, 69] These theories predict that adhesion should scale with $[\ln(u)]^2$, where u is the velocity at which the bonds are stretched, and that a characteristic threshold velocity u_0 exists, below which adhesion does not depend on the bond stretching velocity. The validity of these models have been demonstrated for covalent,[69] electrostatic,[48] and hydrogen bonds.[74, 77] However, these models necessitate detailed knowledge of polymer stretching potentials or bond density, which can be difficult to obtain experimentally. As a result, researchers have searched for a way to probe chemical bond strength in adhesion while holding bond density and polymer elasticity constant. Investigating adhesion and threshold velocity as a function of temperature is one possible approach, as chemical reaction rates are known to be sensitive to temperature.[192]

We previously investigated adhesion of a model underwater epoxy adhesive, DGEBA-Tris (diglycidyl ether of bisphenol A–tris(hydroxymethyl)amino methane), composed of a commonly used structural epoxy backbone (DGEBA) and a tridentate hydrogen bonding moiety, Tris (**Fig. 5.2**). Our studies demonstrated that Tris groups are capable of maintaining their adhesive strength even when the bond was formed in water. We furthermore showed that the adhesion energy of DGEBA-Tris increased with crack velocity as predicted by Chaudhury's model[69] above a characteristic threshold velocity, and that this dependence was consistent with an activation energy of $23k_BT < E_a < 31k_BT$, where k_B is the Boltzmann constant and T is temperature. Our measured activation energies suggested that DGEBA-Tris forms cooperative tridentate hydrogen bonds with mica in both air and in water and we hypothesized that these cooperative bonds were responsible for the remarkable underwater adhesion of DGEBA-Tris. If cooperative bonding does occur in DGEBA-Tris adhesives, we would expect a shift in adhesion with temperature, similar to that observed by Schallamach. For example, we would expect the threshold velocity u_0, *i.e.* the crack velocity above which adhesion increases, would shift to larger values with an increase in temperature. This threshold velocity is highly sensitive to the adhesive chemistry, molecular weight, and even measurement conditions, and thus measurement of changes in u_0 will provide insight into the behavior of the adhesive near the interface.

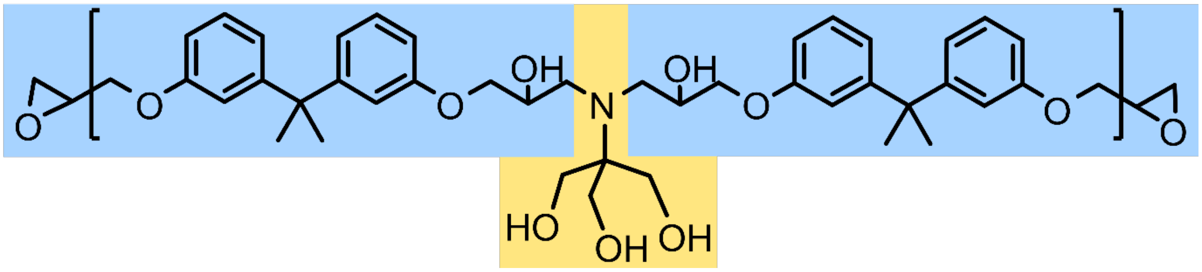

Figure 5.2. Structure of DGEBA-Tris Polymer. Chemical structure of the adhesive, showing the DGEBA units (blue) and the tris moiety (yellow).

Here we investigate the adhesion of cured DGEBA-Tris with mica over a range of debonding temperatures using self-arresting crack propagation measurements. We first cure DGEBA-Tris oligomers to quantify the effect of polymer cure on the magnitude of the adhesive strength to mica surfaces and its dependence on crack velocity. We then control sample temperature between 9 ºC and 60 ºC and repeat the adhesion measurements to mica. From the experimental data we extract the intrinsic energy release rate (G_0) and the threshold velocity. Using these values, we relate the dependence of u_o on temperature to the bond strength, confirming that DGEBA-Tris bonds to mica through cooperative tridentate interactions and that interfacial fracture occurs through an activated process across the temperature range investigated.

5.3 Theoretical Background

Following the derivation in Chapter 4, consider the interaction between an adhesive and an adherend, where chemical bonds at the interface between the two materials act to hold the system together. A crack of length ℓ exists between the two materials. As a tensile force F is applied, the crack will tend to propagate further along the interface, separating the surfaces. However, to do so the chemical bonds at the interface must be broken, leading to an energy that resists detachment G, the strain energy release rate.

The interface is composed of individual chemical bonds of strength E_a and density Σ. In an adhesion measurement the bond can be stretched as the material is loaded, thereby storing energy and resisting detachment, up until the point where the bond dissociates. However, due to random thermal dissociation of the bonds, most bonds will dissociate long before they reach an energy of E_a. If the bond is pulled slowly (relative to the average bond lifetime), the typical bond will randomly dissociate before a substantial amount of force is applied. However, if the bond is rapidly stretched a larger amount of energy can be stored before the bond ruptures.[53]

If we model each bond as being attached to the adhesive by a polymer chain of spring constant M, the average energy U_{avg} stored in each bond before it breaks is $U_{avg} = \frac{1}{2}M\Delta x_{avg}$. The average elongation at rupture, Δx_{avg}, can be further found through $\Delta x_{avg} = V_{stretch}\tau$, where $V_{stretch}$ is the velocity at which the bond is stretched. If we approximate $V_{stretch}$ as the velocity of the crack $u \equiv \frac{dl}{dt}$, the average energy stored in the bond before rupture becomes $U_{avg} = \frac{1}{2}Mu\tau$. Chaudhury modeled this concept by extending the Bell-Evans theory to macroscale adhesion:[69]

$$G - G_0 = \left(\frac{\Sigma}{2M}\right)\left[\left(\frac{k_BT}{\lambda}\right)\ln\left(\frac{M\lambda u\tau}{nk_BT}\right)\right]^2. \tag{5.1}$$

Here G_0 is the threshold (zero velocity) strain energy release rate, k_B is Boltzmann's constant, T is the temperature of the system, λ is the characteristic bond length scale, and n is the Lake-Thomas amplification factor, relating to the length of the polymer chain.

Eqn. 5.1 predicts that G increases beyond the value of G_0 above a threshold velocity defined as[25]

$$u_0 = \frac{nk_BT}{M\lambda\tau}. \tag{5.2}$$

Below $u = u_0$, $G = G_0$ and G does not depend on velocity. The dependence of u_0 on M is theorized to cause upward shifts in u_0 with increasing molecular weight, because the polymer spring constant M decreases as the chain length increases.[62, 63] Furthermore, increasing molecular weight may increase n as more intrachain bonds will be deformed during the stretching process, thereby increasing the energy storage within the chain.[58, 59] These two effects combine to require far greater deformation of a longer polymer chain to obtain the same force on the interfacial bond, thus necessitating higher velocities for adhesion amplification.

The bond lifetime itself can related to E_a through Eyring's equation:[56]

$$\tau = \frac{h}{k_BT}\exp\left(\frac{E_a}{k_BT}\right), \tag{5.3}$$

where h is Planck's constant. In addition to the strong dependence of τ on E_a discussed in Chapter 4, τ is affected by the temperature at which measurements are performed, as shown in **Fig. 5.3** for a bond of $E_a = 1.2\text{x}10^{-19}$ J. At higher temperatures, the bonded atoms have higher thermal energy and are thus more likely to overcome the bond energy barrier and dissociate at any given time, thus the average bond lifetime is lower.

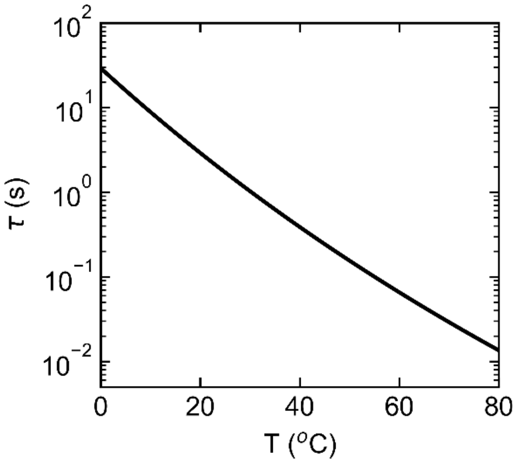

Figure 5.3. Theoretical variation in bond lifetime with temperature. Effect of temperature on the bond lifetime calculated through **Eqn. 5.3** for an activation energy of $E_a = 1.2\text{x}10^{-19}$ J (30 k_BT at 20 °C).

By combining **Eqns. 5.2** and **5.3**, one can determine the temperature dependence of u_0:

$$-\ln(u_0) = \frac{E_a}{k_BT} + \ln\left(\frac{hM\lambda}{n(k_BT)^2}\right). \tag{5.4}$$

Though the final term in **Eqn. 5.4** has a dependence on ln $(\frac{1}{T^2})$, this term varies negligibly over the range of 0 – 60 °C. Therefore, for interfacial fracture involving an activated chemical process, u_0 should vary approximately logarithmically with $1/T$ over this range of temperatures.

5.4 Materials and methods

5.4.1 Materials

HNO_3 (69%, Fisher), ethanol (200 proof, Koptec), tetrahydrofuran (THF, >99.5%, Supelco), RBS-35 detergent (Thermo Fisher), muscovite mica (Ruby, ASTM V-1/V-2, S&J Trading), DGEBA (Hexion Inc. EPON Resin 825), and 2-amino-2-(hydroxymethyl)-1,3-propanediol (Tris, >99.9%, Sigma-Aldrich) were purchased and used as received. Deionized (DI) water (>18.2 MΩ cm resistivity) was obtained from an EMD Milli-Q Integral Water Purification System.

5.4.2 Synthesis of DGEBA–Tris Oligomers

2-(Bis(1-hydroxy-2-(4-(2-(4-(oxiran-2-ylmethoxy)phenyl)propan-2-yl)phenoxy)ethyl)amino)-2-(hydroxymethyl)propane-1,3-diol diglycidyl ether of bisphenol A–tris(hydroxymethyl)amino methane, DGEBA–Tris) oligomers were synthesized as previously reported,[27, 159] by opening of the epoxide ring in DGEBA oligomers through the Tris amine group. A 2:1 stoichiometric ratio of DGEBA:Tris was dissolved in ethanol at 78 °C and stirred for 18 h to allow the reaction to complete. The resulting DGEBA-Tris oligomers were diluted to 180 mM in 4:1 ethanol/THF, then stored at 5 °C until use.

5.4.3 Preparation of Self-Arresting Crack Samples

Specimen preparation begins by cleaving large, thick muscovite mica sheets (~2 cm × 6 cm, 10–30 μm thickness) in a laminar flow hood, then cutting them into a single-crystal rectangle. Each sheet is rinsed with 5 mL of 8 μL HNO_3/50 mL H_2O solution to replace the surface K^+ ions with H^+ ions, then blown off with N_2. For DGEBA-Tris samples, a 67 mM spincoating solution of DGEBA-Tris oligomers is prepared by diluting the storage solution with THF, then sonicating to mix. Oligomer films are spincoated on to mica sheets with 500 μL of the 67 mM spincoating solution at 3000 RPM for 60 s. Oligomer coated mica sheets are then immediately placed in an oven at 80 °C under vacuum for 1 h to remove residual solvent. Meanwhile, a large, thick mica base sheet (~150 cm^2 area, ~1 mm thick) is freshly cleaved, rinsed with 20 mL of 8 μL HNO_3/50 mL H_2O solution, and dried first with nitrogen and then on a hot plate at 150 °C for > 10 min. After annealing the oligomer coated mica sheets, the samples are removed from the oven and gently placed (oligomer side down) on clean sections of the dry mica base sheet, while both mica sheets were warm to facilitate contact. Both sheets are firmly pressed together, and a squeegee was used to remove any remaining air bubbles before cutting the samples to size. One edge of the thinner sheet is lifted up slightly to facilitate opening after cure, then a steel block was placed on the sample and the sample was returned to the oven at 100 °C under constant N_2 flow for 1 h, before a slow ramp up to 200 °C (25 °C / 30 min). DGEBA-Tris samples were cured at 200 °C for 4 hours before removal from the oven to cool. EPON samples were fabricated in an identical manner, except for spincoating with a 47 mM EPON 825 (one DGEBA unit per molecule) in THF/ETOH solution, then curing at 220 °C for 48 h.

5.4.4 Attenuated Total Reflection Fourier Transform Infrared Spectroscopy

ATR-FTIR was performed with a Bruker Vertex 80 spectrometer using a DLaTGS detector and a diamond ATR crystal (Bruker A225). Spectra are collected as an average of 100 scans over 4000 – 400 cm^{-1} with 2 cm^{-1} resolution. A blank (air) background is subtracted from each scan, and an asymmetric least-squares smoothing algorithm is performed to correct for tilted baselines. Samples for FTIR study are fabricated by dropcasting 100 – 400 μL of oligomer stock solution onto a clean silicon wafer, allowing the solution to air dry, then curing in the oven following the same annealing and ramp-up procedure as for self-arresting crack samples, until the desired curing time and temperature is reached. For each sample, spectra are taken at a minimum of two locations, and at least two different samples are tested for each curing time/temperature.

5.4.5 Stylus Profilometry

Stylus profilometry was performed with a Dektak 11A, calibrated with a 0.902 μm step height reference sample. To determine film height, epoxy adhesives are spincoated onto clean silicon wafers with one side masked using adhesive tape, then cured using the same procedure described in **Section 5.4.3**. After curing, the tape is gently removed, revealing a step-edge of epoxy film.

The silicon wafers are taped onto the profilometer stage and the stylus is lowered onto the bare silicon surface. A 1-2 cm scan is performed such that the stylus lifted onto the epoxy film step, recording the step edge height. The data was leveled by extrapolating the tilt of the substrate through the remainder of the profile.

Determining mica sheet thickness through stylus profilometry is only possible for mica sheets glued onto the base sheet. Otherwise air gaps or unwanted bending of the sheet is present. First, the stylus is lowered onto the upper sheet, then a scan was performed in the same manner as above, except for dropping the stylus off of the mica sheet to record the step edge. The mica thickness is determined by subtracting the height of the substrate immediately after the step edge from the height on the innermost measured section of the upper sheet (away from any damage on the sheet edge). Sheet thickness is measured for at least four locations on each sample and averaged for use in calculations.

5.4.6 Self-Arresting Crack Measurements

Peeling through self-arresting crack propagation is performed through a procedure based upon previously reported methods.[46, 47] A homebuilt peeling apparatus is employed (see **Section 5.5.2**) to monitor the crack position via top-view camera (FLIR) affixed to a microstepping motor (Newmark Systems) to allow movement along the axis of crack motion. The sample is illuminated with light passed through a 555 - 565 nm bandpass filter, allowing the crack position to be visualized through crack-opening interferometry. The samples are placed on top of either a hot plate (Thermo Scientific) for tests at $T \geq 20\ ^{\circ}\mathrm{C}$ or onto a steel chamber connected to a recirculating ice water bath for tests at $T < 20\ ^{\circ}\mathrm{C}$. Samples are held down by steel blocks and left to equilibrate at the desired temperature for at least 1 hour before measurements begin. For cooled samples, the apparatus is placed in a sealed chamber under continuous nitrogen purging to keep the humidity under 20%, preventing condensation on the sample. Temperature was measured using a type J thermocouple (McMaster-Carr) glued onto the measurement stage and an associated thermocouple reader (Digi-Sense).

The self-arresting crack measurements are performed on samples consisting of a thin, pliable mica sheet glued on top of a thicker mica base sheet by a thin layer of epoxy adhesive. When a glass capillary (1 mm diameter) is inserted as a spacer between the two sheets, a crack forms as the more flexible sheet is lifted upwards. This crack will advance until mechanical equilibrium between the elastic bending of the upper sheet and the adhesion is reached. Subsequently, we rapidly advance the spacer by 3 mm, which instantaneously shortens the crack length, then monitor the crack position as it returns to its equilibrium length, ending at least 1 hour after visible motion ceases. Image acquisition rate begins at 20 frames per second for each measurement, then gradually and continuously slows by iteratively increasing the delay between images by a factor of 1.01 for each subsequent image. This results in a frame rate of roughly 1 frame per second after an hour of acquisition. This measurement is repeated several times on each sample by repeatedly advancing the crack. The crack velocity is calculated by smoothing the crack length vs time data using a first-degree Savitzky–Golay filter, then locally fitting a line through the 60 nearest neighbor points to determine the instantaneous slope of the curve. Mica top sheet thickness is determined via stylus profilometry (**Section 5.4.5**) where possible, however stylus profilometry proved unreliable for samples that had been entirely removed from the base sheet. In these cases the mica thickness was determined using a digital micrometer, which resulted in a much larger uncertainty in the thickness value and subsequently larger error bounds in G.

5.5 Results and Discussion

5.5.1 Characterization of polymer cure through ATR-FTIR Spectroscopy

The progress of the curing reaction was monitored through ATR-FTIR spectroscopy. As an epoxy cures, nucleophilic groups react with the epoxide rings within the molecule through an esterification reaction, opening up the rings and extending the polymer chain.[193] The epoxide ring has a characteristic asymmetric vibration mode that appears at 915 cm^{-1}, and observing the disappearance of this peak allows one to monitor the curing progress.[194] **Figure 5.4a** shows that the FTIR spectra of uncured DGEBA (yellow) has a strong peak in the vicinity of 915 cm^{-1}, attributed to the epoxide ring vibration. As the polymer is cured at 220 ºC, this peak decreases in prominence (16 h of cure, orange) until it largely disappears by 48 h of cure (red). By this point the polymer has solidified into a rigid film, further confirming its cure. **Figure 5.4b** shows the FTIR spectra of DGEBA-Tris in the same region, where the uncured DGEBA-Tris oligomers (purple) show the same epoxide peak around 915 cm^{-1}. As the film is cured at 200 ºC, this peak decreases in intensity (2 h: blue; 4 h: green). The curves after 4 h of cure are similar to those after 24 h of cure at 220 ºC, suggesting that the curing reaction is largely complete after 4 h. Additionally, there is no visible browning after 4 h of cure at 200 ºC, which becomes problematic during cures at higher temperatures or longer times.

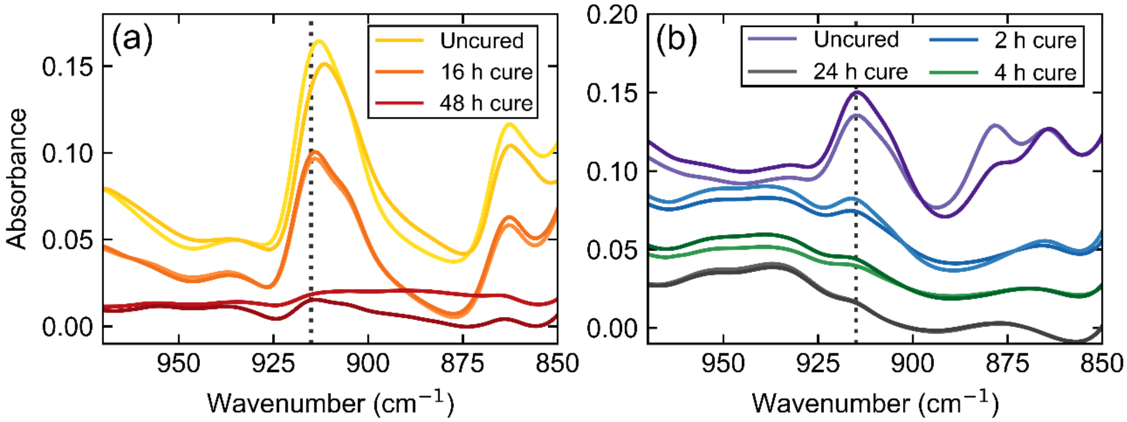

Figure 5.4. **ATR-FTIR spectra in the epoxide stretch region of DGEBA and DGEBA-Tris over varying cure times.** (a) Infrared spectra of uncured DGEBA (yellow) and DGEBA cured for 16 h (orange) and 48 h (red) at 220 ºC. (b) Infrared spectra of uncured DGEBA-Tris (purple), and DGEBA-Tris cured for 2 h (blue) and 4 h (green) at 200 ºC, and 24 h at 220 ºC (grey). Dashed line vertical line indicates the characteristic asymmetric vibration peak of an epoxide ring at 915 cm^{-1}. Spectra are shifted vertically for clarity.

5.5.2 Apparatus for temperature-controlled peeling

Performing self-arresting crack propagation measurements at temperatures other than room temperature requires the development of a experimental set up with temperature control, as previous setups performed tests without temperature control on an inverted microscope.[27, 46] To heat samples reliably, an apparatus was built around a hot plate sample stage (**Fig 5.5a**), allowing for precise control of the sample temperature. Samples were held down using steel blocks to prevent horizontal motion, while a pair of steel rods attached to a micrometer were utilized to move the glass spacer (**Fig 5.5b**). The camera and associated optics were affixed to a microstepping motor, allowing for translation of the camera frame without affecting the sample. Tests revealed that the temperature at the hot plate surface and at the top of a mica sample reliably differed by no more than 1 °C over the range of interest and remained stable for hours once equilibrated.

Cooling of the sample is achieved by replacing the hot-plate sample stage with a water-tight steel chamber (**Fig 5.5c**), which itself is connected to a recirculating ice water bath, providing a constant flow of 0 °C water in and out of the chamber. The samples are then mounted on top of the chamber, allowing for good thermal contact with the reservoir without directly exposing the samples to water. After equilibration, the sample platform surface reliably reached 8 – 9 °C. To prevent condensation, the entire apparatus is then enclosed in a sealed box under a constant purging of N_2. Dishes of desiccant were also placed near the samples and the manipulation of the sample was kept at a minimum to minimize intrusion of ambient humidity. Experiments were only conducted at less than 30% relative humidity (measured at 20 °C), at which point no condensation was observed on (or around) the samples.

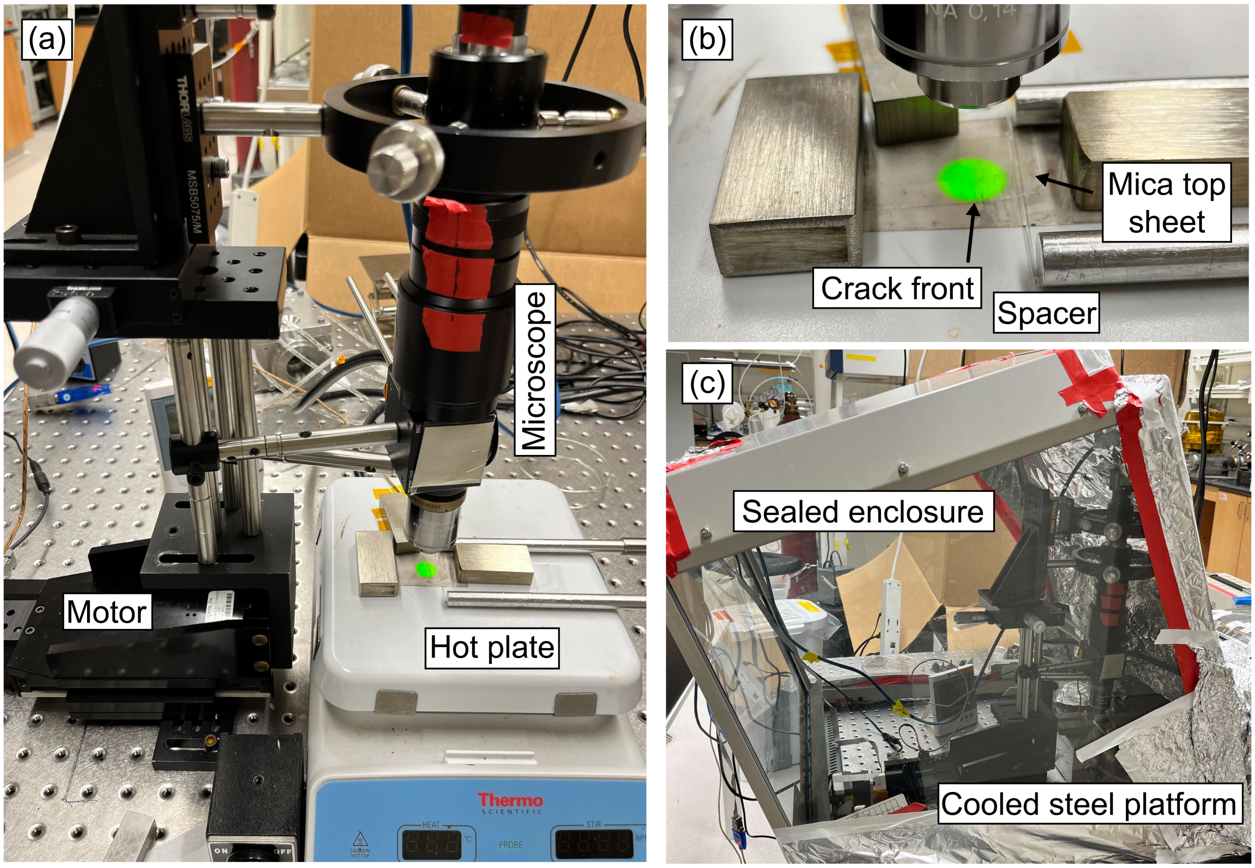

Figure 5.5. Experimental setup. (a) photo of the experimental apparatus for heated tests, showing the translating motor attached to the microscope, camera, and light source, as well as the hot plate and sample. (b) close up photo of the sample, showing the spacer bending the top mica sheet upwards, creating a crack. (c) photo of the setup for cooled experiments, where the sample is placed on a cooled steel platform connected to a recirculating ice water bath (not shown). The entire apparatus is enclosed in a sealed chamber under a constant flow of N_2 to prevent condensation.

5.5.3 Effect of temperature on crack length and adhesion

We rely on self-arresting crack propagation to probe the adhesion of cured DGEBA-Tris to mica sheets. Self-arresting crack propagation enables us to probe adhesion over a wide range of crack velocities and temperatures.[27] As a control, we also characterize the adhesion of cured DGEBA, which does not contain multidentate hydrogen bonding groups. Samples consist of a thin (51.5 ± 5.5 nm) layer of adhesive cured between two mica sheets. A crack of length ℓ is formed at the epoxy/mica interface when the upper (more pliable) mica sheet is lifted by a glass spacer (**Fig. 5.6**). Movement of this spacer causes perturbation of the crack, and the movement of the crack can be observed as the crack returns to its equilibrium length.

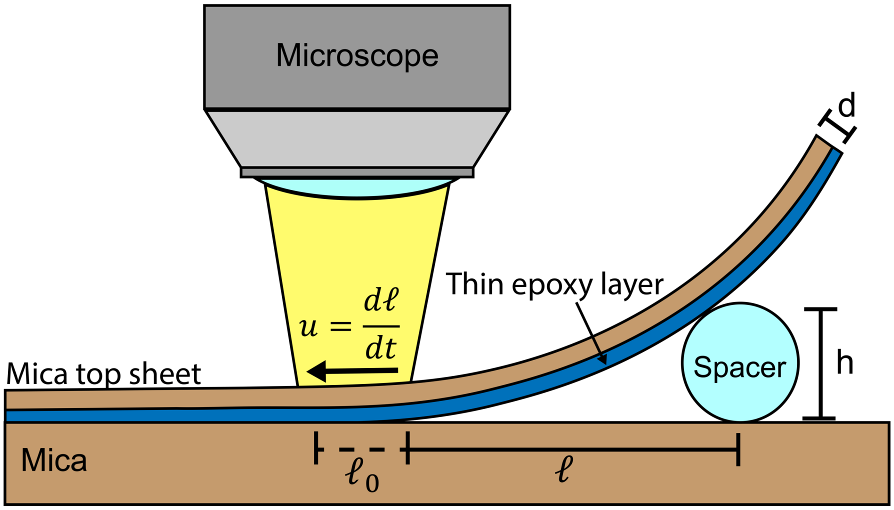

Figure 5.6. Diagram of experimental geometry. Schematic illustrating the key parameters influencing the crack motion. ℓ is the instantaneous crack length, h is the height of the glass spacer rod, d is the thickness of the top mica sheet, and u is the crack velocity. Not to scale.

Figure 5.7a shows representative crack length vs time curves during the debonding of DGEBA-Tris after various cure times in comparison to control materials. For DGEBA and mica/mica (no intervening adhesive), there is significant crack motion within the first second, but the crack quickly reaches its equilibrium length and halts at around 1 s after the initial movement. The short-time rate-dependent adhesion could be due to air resistance as the crack opens. However, for oligomeric DGEBA-Tris the crack continues to move over a significantly longer time, as shown in Chapter 4. Adhesion decreases as the crack velocity decreases, and the crack eventually stops at its equilibrium length. As DGEBA-Tris is cured the crack halts at shorter times, yet crack motion is still observed for longer periods than in control materials.

Figure 5.7b shows that the crack velocity dependence of adhesion charges with debonding temperature for fully cured DGEBA-Tris. At 9 °C, the crack continues to move for 10 - 15 s. As the temperature increases to 21 °C the crack motion halts earlier, at around 2 – 10 s. Further increase in the debonding temperature to 40 °C or 60 °C shows continued decreases in the time it takes for motion to halt. In fact for $T \geq 40\,^{o}C$ it is difficult to visually distinguish the movement of DGEBA-Tris from that of the other rate-independent pairs.

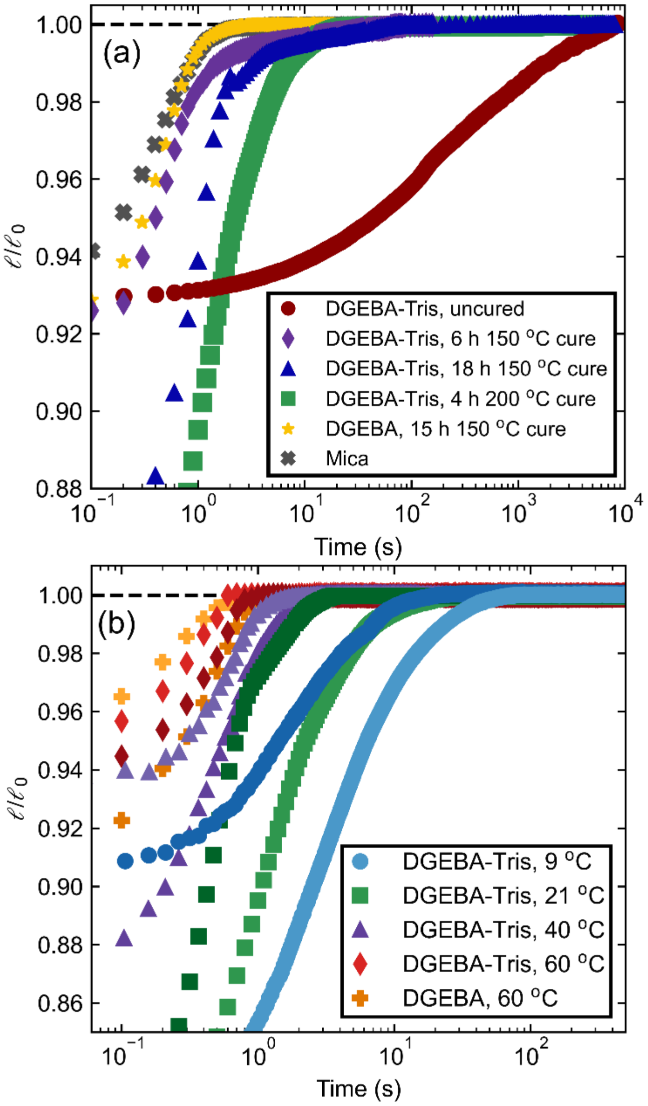

Figure 5.7. Crack propagation dynamics of DGEBA-Tris and DGEBA films. (a) Crack length (normalized by equilibrium crack length) vs time for DGEBA-Tris at 21 °C as a function of cure, ranging from uncured (red circles), 6 h of cure at 150 °C (purple diamonds), 18 h of 150 °C cure (blue triangles), and 4 h of 200 °C cure (green squares). Also shown are controls of DGEBA after 15 h of 150 °C cure (yellow stars) and mica/mica (no intervening adhesive, grey x's). Dashed line indicates $\ell = \ell_0$. All data excepting DGEBA-Tris, 4 h 200 °C cure was originally presented in Chapter 4. (b) Crack length (normalized by equilibrium crack length) vs time for fully cured DGEBA-Tris as a function of measurement temperature, including 9 °C (blue circles), 21 °C (green squares), 40 °C (purple triangles), and 60 °C (red diamonds). Also shown is fully cured DGEBA at 60 °C (orange crosses). Dashed line indicates $\ell = \ell_0$.

The length of the crack is directly controlled by the balance between the bending moment applied to the top mica sheet and the adhesion of the polymer that resists crack opening. This balance can be expressed as:[47]

$$G = \frac{9\mu d^3 h^2}{24\ell^4}, \tag{5.5}$$

where G is the strain energy release rate, μ is the shear modulus of the top mica sheet (taken to be $\mu = 25$ GPa),the Poisson ratio is $\nu = 0.21$[135], h is the spacer height, and d is thickness of the top mica sheet. By knowing the spacer height and mica thickness, G can be determined directly through measurements of ℓ.

After the crack comes to rest, the equilibrium value of the crack length is used to determine the intrinsic strain energy release rate, G_0, through **Eqn. 5.5**. **Figure 5.8** shows the measured values of G_0 for the adhesion of cured DGEBA-Tris to mica as a function of temperature. At ambient temperature (21 ºC, green squares), $G_0 = 0.28 \pm 0.05$ J/m^2, which is slightly higher (p-value =0.06) than the measurement in Chapter 4 of $G_0 = 0.23 \pm 0.04$ J/m^2 for DGEBA-Tris oligomers adhering to mica. This small increase in adhesion may result from improved contact between the adhesive and mica as the polymer melts during the cure process.

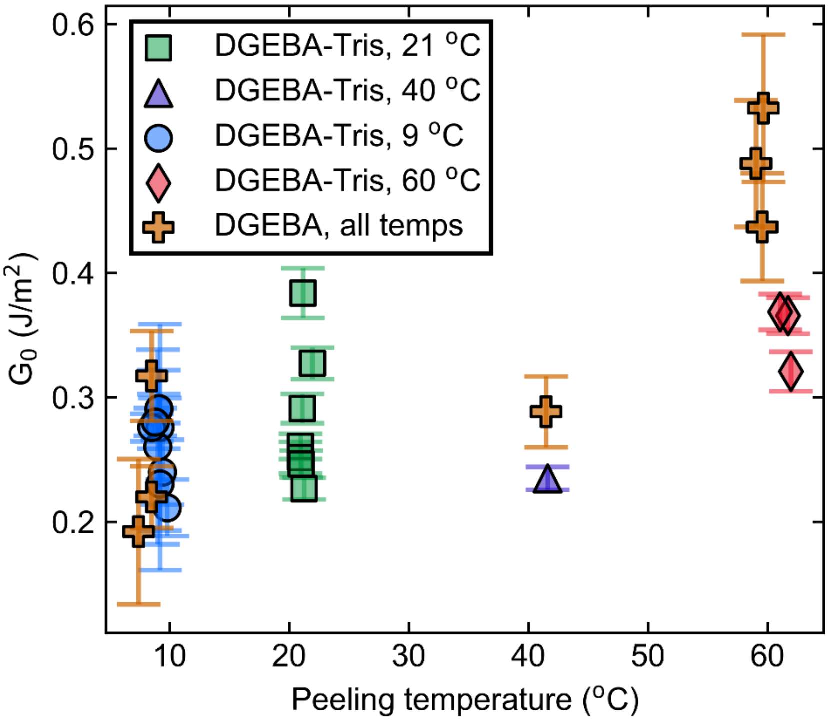

Figure 5.8. Equilibrium adhesion values for DGEBA-Tris and DGEBA films. Equilibrium values of the strain energy release rate vs sample temperature for DGEBA-Tris at 9 ºC (blue circles), 21 ºC (green squares), 40 ºC (purple triangles), and 60 ºC (red diamonds), and for DGEBA control at a range of temperatures (orange crosses).

In addition, G_0 increases with debonding temperature for the cured DGEBA-Tris (p-value = 0.007). For glassy polymers, an increase in adhesion with temperature is common, particularly as a material nears its glass transition temperature. The increase is typically attributed to increased chain mobility as well as dissipation or plasticity within the polymer.[8, 51, 187] Similarly, the elastic modulus of DGEBA decreases by around 25% from 9 – 60 °C.[195] Therefore, softening of the adhesive could contribute to the increase in G_0. Finally, Thermogravimetric Analysis of cured DGEBA-Tris after exposure to laboratory air for > 1 week showed a 14% loss in mass at 60 °C. The loss was attributed to evaporation of absorbed water from the polymer[196, 197] While DGEBA-Tris adheres in the presence of water (see Chapter 4), water will likely lower the van der Waals forces, the main contributor of G_0.[28] Thus G_0 may increase with temperature due to a loss of absorbed water within the polymer.

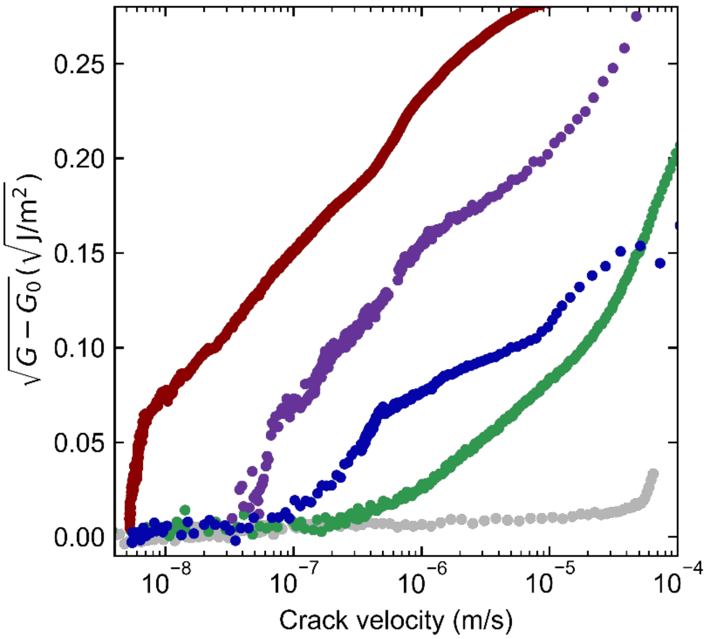

Figure 5.9. **Effect of curing on the dependence of adhesion on crack velocity**. Scaled increase in strain energy release rate vs crack velocity for uncured DGEBA-Tris (red), DGEBA-Tris after 6 h of cure at 150 °C (purple), 18 h of 150 °C cure (blue), and 4 h of 200 °C cure (green). The adhesion of mica to mica (without intervening adhesive) is shown in grey as a control. All measurements performed at 21 °C. Uncured, 150 °C cure, and mica data were originally presented in Chapter 4.

As shown in **Figure 5.9** adhesion increases with velocity for all the DGEBA-Tris adhesives investigated (different degree of curing, debonding temperature), but not for controls (mica, grey) unless much higher speeds are reached. The slow, continuous crack propagation observed with DGEBA-Tris is caused by an amplification of adhesion by the crack velocity, as discussed in Chapter 4. For oligomeric DGEBA-Tris (red), G increases over the entire measurable range of velocities we can capture with our experimental setup. As DGEBA-Tris is cured (6 h 150 °C, purple; 18 h 150 °C, blue; 4 h 200 °C, green), G only begins to increase after a certain onset velocity. As the material is cured further a large increase in the onset velocity is observed from around 50 nm/s to around 1 μm/s, accompanied by a decrease in the slope of G vs crack velocity. At even higher rates (50 – 100 μm/s), G increases faster with crack velocity. Note here that the highest crack velocities are obtained at the beginning of the experiments (crack starts moving quickly, then slows), and there are more uncertainties in our measurements due to difficulties in accurately measuring the velocity at high speeds.

The increase in onset velocity with increased degree of curing for DGEBA-Tris is likely due to the increase in molecular weight of the polymer upon curing. In **Eqn. 5.2** two terms could be directly affected by molecular weight – n and M. The Lake-Thomas amplification factor, n, can be interpreted as the number of bonds in the polymer chain that are stretched as the interfacial bond is pulled.[25] Therefore, n would naturally increase with increasing chain length, although a roughly 80-fold increase would be needed to explain the shift in threshold velocity from the oligomeric to fully cured (4 h, 200 °C) adhesive. The polymer spring constant, M, would logically decrease with curing, as force required to stretch a chain is inversely related to the contour length of the chain.[62] Decreasing M would also increase u_0, and the 80-fold decrease needed to explain the data may be warranted if the chains stretch purely entropically before the bond is broken. A combination of these two effects can also account for the measured trend with more moderate changes to M and n. Finally, a decrease in E_a of around 4 k_BT could also explain the shift of u_0 to higher velocities, which may be possible if tridentate binding is hindered in cured DGEBA-Tris. The exact role of these individual parameters cannot be determined from **Fig. 5.9** alone, but all of them are consistent with curing.

To further investigate the role of bond strength on the threshold velocity, we measured the velocity dependence of cured DGEBA-Tris adhesion across a range of temperatures (**Fig. 5.10**). As the debonding temperature increases from 9 °C (blue) to 21 °C (green), a subtle increase in the onset velocity occurs, from around 300 nm/s to around 700 nm/s. Yet when the temperature is further increased to 40 °C (purple), the onset velocity jumps to above 10 μm/s. As temperature increases, G is also seen to rapidly grow almost immediately above the onset velocity, in particular for the measurements at 60 °C (red). In fact, the rate-dependent adhesion of cured DGEBA-Tris at 60 °C is difficult to distinguish from that of DGEBA at 60 °C (orange). At 60 °C the crack halts after around 0.7 s for both materials, and therefore any differences at velocities above u_0 may occur to quickly to be captured by our camera.

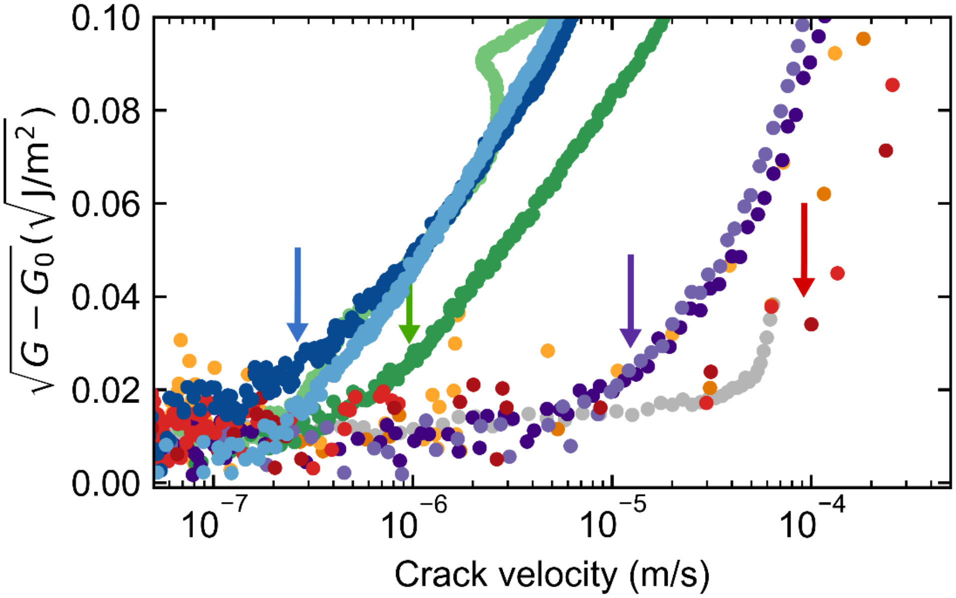

Figure 5.10. **Effect of measurement temperature on adhesion and velocity dependence**. Scaled increase in strain energy release rate vs crack velocity for cured DGEBA-Tris (4 h 200 ºC cure) at 9 ºC (blue), 21 ºC (green), 40 ºC (purple), and 60 ºC (red). Also shown are DGEBA at 60 ºC (orange), and H^+ mica at 21 ºC. Arrows indicate approximate locations of the threshold velocity, determined by the point where adhesion increases significantly over the equilibrium value.

The increase in threshold velocity with debonding temperature is hypothesized to be caused by a thermally-induced decrease in bond lifetime. As shown in **Fig. 5.3**, τ is expected to decrease by over 2 orders of magnitude between 9 ºC and 60 ºC solely due the contribution of increased thermal bond dissociation, which would lead to an increase in u_0 inversely proportional to the decrease in τ. We next seek to test this hypothesis by extracting u_0 from the measured data. We first determine G_0 by averaging values of G after the apparent crack velocity drops below our resolution, around 1 nm/s. We next locate the point where $G - G_0 > 0.5$ mJ/m^2, where an increase in adhesion could be clearly differentiated from the noise in the experimental data.

If the measured adhesion is due to activated bond scission at the interface, $\ln(u_0)$ should scale approximately linearly with $\left(\frac{1}{T}\right)$, as predicted by **Eqn. 5.4**. **Figure 5.11** shows that the estimated u_0 does behave according to **Eqn. 5.4**, with $-\ln(u_0)$ decreasing at higher temperatures. Linear regression of the data in **Fig. 5.11** yields $E_a = 14 \pm 2\,\mathrm{x}10^{-20}$ J (R^2 = 0.74), equivalent to $E_a = 35 \pm 4\ k_BT$ at 20 ºC. While this estimate is higher than those obtained in Chapter 4 for uncured DGEBA-Tris adhesion with mica (23 – 31 k_BT), it remains close to the estimated value for cooperative tridentate hydrogen bonding interactions ($\approx 30k_BT$). Possible errors associated with the different methods of estimating E_a could play a role as well – a slight overestimate of G_0 in Chapter 4 or and underestimate of u_0 in the present work would align these values. Furthermore, the present value of E_a does not rely upon estimates of M or n, and thus is less reliant upon assumptions about the polymer stretching behavior. Finally, the polymer studied here is expected to be significantly more cured, and entanglement could affect the ability of moieties to form cooperative interactions.[56]

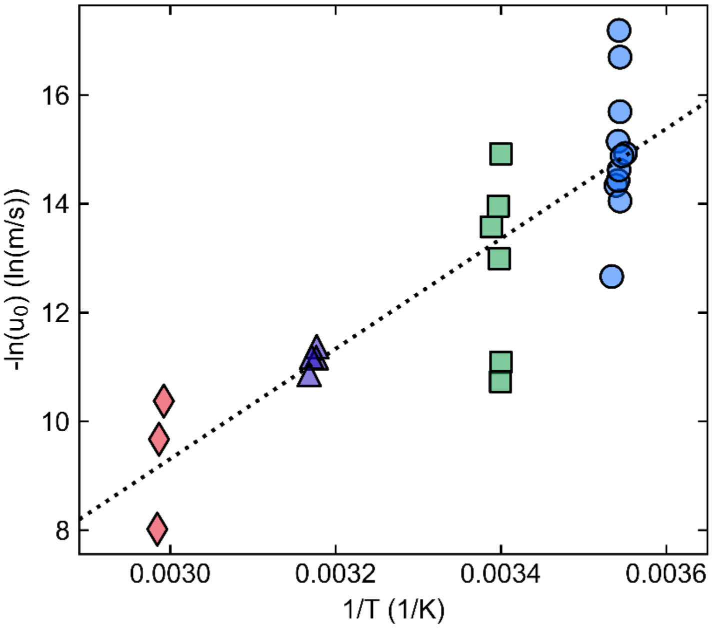

Figure 5.11. Effect of debonding temperature on threshold velocity. Inverse temperature vs negative natural logarithm of the threshold velocity. Temperatures shown are 9 ºC (blue circles), 21 ºC (green squares), 40 ºC (purple triangles), and 60 ºC (red diamonds).

Despite the strong correlation between the data in **Fig. 5.11** and the predictions of **Eqn. 5.4**, other mechanisms may also contribute to the observed increase in u_0 with temperature. **Eqn. 5.2** predicts that u_0 is inversely proportional to M. While polymer force-vs-elongation behavior is not expected to change significantly with temperature over this range, a shortened bond survival time could lead to polymer stretching that is largely entropically dominated, resulting in a reduction in M at higher temperatures.[198, 199] Similar effects could occur from bulk softening of the material at higher temperatures,[195] and would require single-molecule study to disentangle further. Finally, the fracture of epoxies is known to transition to stick-slip motion at higher temperatures, which could make u_0 appear to be higher than that predicted through **Eqn. 5.4**.[8] Stick-slip motion was sometimes observed during peeling, particularly around defects within the sample. These measurements were excluded from analysis, but defects occurring near the final crack position could be difficult to detect. Nevertheless, while these effects may contribute to the observed trend in **Fig. 5.11**, they are unlikely to dominate the effect of temperature on the bond failure rate.

We thus conclude that the adhesion of DGEBA-Tris to mica occurs via tridentate hydrogen bonds with E_a of $O(30k_BT)$, in agreement with the findings in Chapter 4. These findings rule out a decrease in E_a as a mechanism for the increase in threshold velocity with curing seen in **Fig.**

5.9, suggesting that increased molecular weight is primarily responsible for the two-orders of magnitude increase in u_0 after cure. We further see that interfacial bond fracture dynamics follow an Arrhenius-like dependence, which is commonly used to describe chemical reaction rates.[192] This provides a direct connection between the dynamics of a chemical bond at an interface and the overall adhesive strength of a system.

This has additional implications for the durability of adhesives relying upon multidentate bonds at elevated temperatures, as the longevity of the cooperative bond drastically decreases at higher temperatures. Since cooperative bonding is believed to be behind the remarkable water resistance of multidentate adhesives,[156, 158] their ability to adhere underwater may be diminished at elevated temperatures. The shift in threshold velocity with increasing temperature or molecular weight may further impact the long-term aging and creep behavior, as the loss of adhesion amplification at low velocities eliminates a possible mechanism for arresting interfacial cracks.

5.6 Conclusion

The adhesion of model DGEBA epoxy adhesives with tridentate hydrogen bonding groups (Tris) to mica was studied as a function of degree of cure and measurement temperature. We confirmed that the adhesion of DGEBA-Tris scales with crack velocity over a wide range of conditions according to Chaudhury's model,[69] and observed the presence of a characteristic threshold velocity, above which adhesion increases with crack velocity. While the zero-velocity threshold strain energy release rate exhibited only minor increases with cure and temperature, the threshold velocity increased by two orders of magnitude with both curing and with an increase in temperature of 40 °C. The increase in u_0 with cure was attributed to increased molecular weight, with a softer polymer chain transferring less force to the interfacial bond. The shift in u_0 with temperature followed an Arrhenius-like dependence with an activation energy of 14 ± 2 x10^{-20} J ($35 \pm 4\ k_B T$ at 20 °C), which further validates the hypothesis that DGEBA-Tris bonds to mica through cooperative tridentate hydrogen bonds. The temperature dependence of u_0 occurs due to the increased thermal dissociation rate of interfacial bonds at elevated temperatures, necessitating higher velocities to see an improvement in adhesive strength. These results have implications for our understanding of how multidentate bonds function at an adhesive interface particularly at non-ambient temperatures and provide new avenues for connecting chemical bond dynamics to macroscale adhesive strength.

6 Summary & Outlook

The ability to design and optimize future adhesives relies upon our ability to relate the chemical structure of an adhesive to its performance on a macroscopic scale.[200] While great progress has been made in understanding structure-property relationships in the bulk of an adhesive,[8, 36, 93] much remains unclear about the relationship between interfacial chemistry and macroscale adhesion.[68, 200, 201] This knowledge gap particularly impacts structural adhesives, where the stiff bulk of the adhesive makes them especially sensitive to interfacial bond strength.[201, 202] To address this gap, this dissertation implements theories and methods to probe the chemical behavior of a model epoxy adhesive modified with tridentate hydrogen bonding function groups. As part of these investigations, we further developed techniques to mitigate confounding experimental factors, allowing us to conduct sensitive interfacial measurements.

In Chapter 3, we developed and demonstrated a method of producing ultra-smooth aluminum films through evaporating onto a mica template, followed by removal of the mica template in water. We first characterized the deposited films through Atomic Force Microscopy, revealing an extremely low RMS roughness of 0.2 nm. We then confirmed that the surface was composed of aluminum/aluminum oxide through X-ray photoelectron spectroscopy and contact angle goniometry after self-assembled monolayer deposition. We next demonstrated the use of these films, showing that they are suitable for interferometry and have a nearly 6-fold increase in adhesion with mica over rougher aluminum surfaces. We further investigated the electrostatic double-layer around aluminum surfaces in LiCl solution and additionally measured improved corrosion resistance of smooth aluminum films, demonstrating the crucial role surface roughness has on accurately measuring interfacial phenomena.

In Chapter 4 we investigated the adhesion of a multidentate hydrogen bonding epoxy adhesive (DGEBA-Tris), with promising applications in improving the water resistance of structural adhesives. We first established that the DGEBA-Tris epoxies exhibited a strong increase in adhesion with crack velocity, which was shown to scale as predicted by a model for thermally-activated bond scission at an interface. We next showed that the adhesion of DGEBA-Tris to mica and aluminum was not undermined when the bond was formed in water. We further demonstrated that the underwater adhesion of DGEBA-Tris scaled similarly with velocity to the adhesion in air, and that the measured scaling could be explained by the Tris groups bonding cooperatively. We discussed how the cooperative bonding of Tris groups is likely responsible for its remarkable adhesion in water, as tridentate bonds may be able to compete for interfacial bonding sites with water molecules.

In Chapter 5 we built upon our previous studies of DGEBA-Tris to investigate the role of temperature and curing on the interfacial chemical bond dynamics. We first showed that the threshold (zero-velocity) adhesion is only minorly affected by increasing molecular weight and temperature. However, the threshold velocity increased dramatically with both increasing molecular weight and temperature. The two orders of magnitude increase in threshold velocity during cure was attributed to increasing polymer chain length necessitating larger extensions to apply the same force to the interfacial bond. The additional two orders of magnitude increase in transition velocity when temperature was increased from 9 °C to 60 °C was related to increased dissociation bond dissociation at elevated temperatures. The resulting Arrhenius-like dependence of threshold velocity on temperature yielded an activation energy of $35 \pm 4\ k_B T$ at 20 °C, further confirming that DGEBA-Tris adheres through cooperative tridentate bonds and that adhesive failure occurs through an activated process.

6.1 Future directions

This thesis established that tridentate hydrogen bonding moieties, when added into a structural epoxy, can allow the adhesive to bind strongly in water and yield strong underwater adhesive performance. It is further shown that the increase of adhesion with crack velocity can be used to probe the strength and mechanics of interfacial bonds, allowing remarkable insight into the dynamics of bonds at an interface. Refinement of the demonstrated theories to employ more accurate models, particularly for polymer stretching potentials and thermally-assisted bond failure (reaction rates), would enable more accurate *a priori* prediction of adhesive strength from molecular structure.[25, 203] Notable progress on this front has been recently reported by Yang, Liechti, and Huang, who developed a model incorporating widely-accepted polymer stretching and reaction rate equations for the fracture of an epoxy adhesive.[24] The generalization of this model to other systems would enable multiscale adhesion studies under more complex conditions and a broader understanding of the effects of bond strength, molecular weight, and temperature at an adhesive interface.

The results presented in Chapters 4 and 5 introduce further questions about the role of cooperative interactions in adhesion as well as the limitations imposed by chemical structure. Given the remarkable underwater adhesion characteristics promoted by Tris and other multidentate groups, such as DOPA[11, 204] or UPy,[156] investigation of other multidentate moieties could enable even stronger and more robust adhesives. Future investigations should focus on the role of moiety flexibility on its ability to form cooperative interactions in order to allow for binding to a wider variety of surfaces. Furthermore, intriguing results by Ghatak *et al.*[56] showing surprisingly high bond lifetimes for highly entangled systems poses questions on the ability for cooperative interactions to form among non-adjacent groups. Studies on multidentate moieties with a varied spacing between the individual binding sites would improve our understanding of how more complex systems function, as well as possibly open the door for using more diverse chemistries to improve adhesion. [158]

Finally, the emergence of multidentate groups to promote strong underwater adhesion raises questions about the mechanisms by which these types of groups form adhesives bonds underwater.[158, 205, 206] Previous results by Wang and Frechette show that hydrodynamic drainage can impede the formation of contact between adhesive and adherend,[207, 208] and spectroscopic studies have revealed the presence of interfacial water at a buried interface.[209] Careful studies on the formation of adhesive interactions will elucidate how certain chemical groups can dehydrate an interface, and will aid in improving deposition protocol to maximize underwater adhesion.

7 References

(1) Dillard, D. A. Fundamentals of Stress Transfer in Bonded Systems. In *The Mechanics of Adhesion*, 1 ed.; Dillard, D. A., Poicus, A. V. Eds.; Adhesion Science and Engineering, Elsevier, 2002; pp 1-44.

(2) Everaerts, A. I.; Xia, J. Indium-Tin-Oxide Compatible Optically Clear Adhesive. U.S. WO 2009/045889 A2, 2009.

(3) Petrie, E. M. An Overview of Adhesives and Sealants. In *Handbook of Adhesives and Sealants*, 2nd ed.; McGraw-Hill, 2007; pp 3-37.

(4) Skeist, I.; Miron, J. Introduction to Adhesives. In *Handbook of Adhesives*, 3rd ed.; Skeist, I. Ed.; Chapman & Hall, 1990; pp 3 - 20.

(5) Llorca, J.; Gonzalez, C.; Molina-Aldareguia, J. M.; Segurado, J.; Seltzer, R.; Sket, F.; Rodriguez, M.; Sadaba, S.; Munoz, R.; Canal, L. P. Multiscale Modeling of Composite Materials: A Roadmap Towards Virtual Testing. *Adv Mater* **2011**, *23* (44), 5130-5147. DOI: 10.1002/adma.201101683

(6) Cavezza, F.; Boehm, M.; Terryn, H.; Hauffman, T. A Review on Adhesively Bonded Aluminium Joints in the Automotive Industry. *Metals* **2020**, *10* (6). DOI: 10.3390/met10060730

(7) Politi, R. E. Structural Adhesives in the Aerospace Industry. In *Handbook of Adhesives*, 3rd ed.; Skeist, I. Ed.; Chapman & Hall, 1990; pp 713 - 728.

(8) Kinloch, A. J. *Adhesion and Adhesives*; Springer, 1987, DOI: 10.1007/978-94-015-7764-9.

(9) Bowditch, M. R. The Durability of Adhesive Joints in the Presence of Water. *International Journal of Adhesion and Adhesives* **1996**, *16* (2), 73-79. DOI: 10.1016/0143-7496(96)00001-2

(10) Kinloch, A. J.; Kronenberg, C. F.; Tan, K. T.; Watts, J. F. The Durability of Structural Adhesive Joints. In 7th European Adhesion Conference, Freidburg, Germany; 2004.

(11) Lee, B. P.; Messersmith, P. B.; Israelachvili, J. N.; Waite, J. H. Mussel-Inspired Adhesives and Coatings. *Annu Rev Mater Res* **2011**, *41*, 99-132. DOI: 10.1146/annurev-matsci-062910-100429

(12) Stewart, R. J.; Ransom, T. C.; Hlady, V. Natural Underwater Adhesives. *J Polym Sci B Polym Phys* **2011**, *49* (11), 757-771. DOI: 10.1002/polb.22256

(13) Maier, G. P.; Rapp, M. V.; Waite, J. H.; Israelachvili, J. N.; Butler, A. Biological Adhesives. Adaptive Synergy between Catechol and Lysine Promotes Wet Adhesion by Surface Salt Displacement. *Science* **2015**, *349* (6248), 628-632. DOI: 10.1126/science.aab0556

(14) Yuk, H.; Varela, C. E.; Nabzdyk, C. S.; Mao, X.; Padera, R. F.; Roche, E. T.; Zhao, X. Dry Double-Sided Tape for Adhesion of Wet Tissues and Devices. *Nature* **2019**, *575* (7781), 169-174. DOI: 10.1038/s41586-019-1710-5

(15) Yuk, H.; Zhang, T.; Lin, S.; Parada, G. A.; Zhao, X. Tough Bonding of Hydrogels to Diverse Non-Porous Surfaces. *Nat Mater* **2016**, *15* (2), 190-196. DOI: 10.1038/nmat4463

(16) Brewis, D. M.; Comyn, J.; Raval, A. K.; Kinloch, A. J. The Effect of Humidity on the Durability of Aluminium-Epoxide Joints. *International Journal of Adhesion and Adhesives* **1990**, *10* (4), 247-253. DOI: 10.1016/0143-7496(90)90042-v

(17) Tam, L. H.; Chow, C. L.; Lau, D. Moisture Effect on Interfacial Integrity of Epoxy-Bonded System: A Hierarchical Approach. *Nanotechnology* **2018**, *29* (2), 024001. DOI: 10.1088/1361-6528/aa9537

(18) Yang, J.; Bai, R.; Chen, B.; Suo, Z. Hydrogel Adhesion: A Supramolecular Synergy of Chemistry, Topology, and Mechanics. *Advanced Functional Materials* **2019**, *30* (2). DOI: 10.1002/adfm.201901693

(19) Lee, H.; Lee, B. P.; Messersmith, P. B. A Reversible Wet/Dry Adhesive Inspired by Mussels and Geckos. *Nature* **2007**, *448* (7151), 338-341. DOI: 10.1038/nature05968

(20) Raos, G.; Zappone, B. Polymer Adhesion: Seeking New Solutions for an Old Problem. *Macromolecules* **2021**, *54* (23), 10617-10644. DOI: 10.1021/acs.macromol.1c01182

(21) Hofman, A. H.; van Hees, I. A.; Yang, J.; Kamperman, M. Bioinspired Underwater Adhesives by Using the Supramolecular Toolbox. *Adv Mater* **2018**, *30* (19), e1704640. DOI: 10.1002/adma.201704640

(22) Matos-Perez, C. R.; White, J. D.; Wilker, J. J. Polymer Composition and Substrate Influences on the Adhesive Bonding of a Biomimetic, Cross-Linking Polymer. *J Am Chem Soc* **2012**, *134* (22), 9498-9505. DOI: 10.1021/ja303369p

(23) Gong, L.; Xiang, L.; Zhang, J.; Chen, J.; Zeng, H. Fundamentals and Advances in the Adhesion of Polymer Surfaces and Thin Films. *Langmuir* **2019**, *35* (48), 15914-15936. DOI: 10.1021/acs.langmuir.9b02123

(24) Yang, T.; Liechti, K. M.; Huang, R. A Multiscale Cohesive Zone Model for Rate-Dependent Fracture of Interfaces. *Journal of the Mechanics and Physics of Solids* **2020**, *145*. DOI: 10.1016/j.jmps.2020.104142

(25) Hui, C. Y.; Tang, T.; Lin, Y. Y.; Chaudhury, M. K. Failure of Elastomeric Polymers Due to Rate Dependent Bond Rupture. *Langmuir* **2004**, *20* (14), 6052-6064. DOI: 10.1021/la0356607

(26) van Engers, C. D.; Lamberty, Z. D.; McGuiggan, P. M.; Frechette, J. Template-Stripped Ultra-Smooth Aluminum Films (0.2 Nm Rms) for the Surface Forces Apparatus. *Langmuir* **2021**, *37* (21), 6556-6565. DOI: 10.1021/acs.langmuir.1c00899

(27) Lamberty, Z. D.; Tran, N. T.; van Engers, C. D.; Karnal, P.; Knorr, D. B., Jr.; Frechette, J. Cooperative Tridentate Hydrogen-Bonding Interactions Enable Strong Underwater Adhesion. *ACS Appl Mater Interfaces* **2023**, *15* (29), 35720-35731. DOI: 10.1021/acsami.3c06545

(28) Israelachvili, J. *Intermolecular and Surface Forces*; Academic Press, 2011, p^pp 291-337.

(29) Berg, J. C. *An Introduction to Interfaces and Colloids*; World Scientific, 2010.

(30) Li, J.; Celiz, A. D.; Yang, J.; Yang, Q.; Wamala, I.; Whyte, W.; Seo, B. R.; Vasilyev, N. V.; Vlassak, J. J.; Suo, Z.; et al. Tough Adhesives for Diverse Wet Surfaces. *Science* **2017**, *357* (6349), 378-381. DOI: 10.1126/science.aah6362

(31) Lee, H.; Scherer, N. F.; Messersmith, P. B. Single-Molecule Mechanics of Mussel Adhesion. *Proc Natl Acad Sci U S A* **2006**, *103* (35), 12999-13003. DOI: 10.1073/pnas.0605552103

(32) Shull, K. R. Contact Mechanics and the Adhesion of Soft Solids. *Materials Science and Engineering: R: Reports* **2002**, *36* (1), 1-45. DOI: 10.1016/s0927-796x(01)00039-0

(33) Karnal, P.; Roberts, P.; Gryska, S.; King, C.; Barrios, C.; Frechette, J. Importance of Substrate Functionality on the Adhesion and Debonding of a Pressure-Sensitive Adhesive under Water. *ACS Appl Mater Interfaces* **2017**, *9* (48), 42344-42353. DOI: 10.1021/acsami.7b13984

(34) Butt, H.-J.; Kappl, M. *Surface and Interfacial Forces*; Wiley, 2010.

(35) Bartlett, M. D.; Croll, A. B.; King, D. R.; Paret, B. M.; Irschick, D. J.; Crosby, A. J. Looking Beyond Fibrillar Features to Scale Gecko-Like Adhesion. *Adv Mater* **2012**, *24* (8), 1078-1083. DOI: 10.1002/adma.201104191

(36) Gent, A. N.; Kinloch, A. J. Adhesion of Viscoelastic Materials to Rigid Substrates. Iii. Energy Criterion for Failure. *Journal of Polymer Science Part A-2: Polymer Physics* **1971**, *9* (4), 659-668. DOI: 10.1002/pol.1971.160090408

(37) Maugis, D. *Contact, Adhesion and Rupture of Elastic Solids*; Springer, 2000, DOI: 10.1007/978-3-662-04125-3.

(38) Croll, A. B.; Hosseini, N.; Bartlett, M. D. Switchable Adhesives for Multifunctional Interfaces. *Advanced Materials Technologies* **2019**, *4* (8). DOI: 10.1002/admt.201900193

(39) Johnson, K. L. *Contact Mechanics*; 2012, DOI: 10.1017/cbo9781139171731.

(40) Johnson, K. L.; Kendall, K.; Roberts, A. D. Surface Energy and the Contact of Elastic Solids. *Proceedings of the Royal Society of London. A. Mathematical and Physical Sciences* **1971**, *324*, 301-313. DOI: 10.1098/rspa.1971.0141

(41) Maugis, D. Adhesion of Spheres: The JKR-Dmt Transition Using a Dugdale Model. *Journal of Colloid and Interface Science* **1992**, *150* (1), 243-269. DOI: 10.1016/0021-9797(92)90285-t

(42) Maugis, D.; Barquins, M. Fracture Mechanics and the Adherence of Viscoelastic Bodies. *Journal of Physics D: Applied Physics* **1978**, *11* (14), 1989-2023. DOI: 10.1088/0022-3727/11/14/011

(43) Shull, K. R.; Ahn, D.; Chen, W.-L.; Flanigan, C. M.; Crosby, A. J. Axisymmetric Adhesion Tests of Soft Materials. *Macromolecular Chemistry and Physics* **1998**, *199* (4), 489-511. DOI: 10.1002/(sici)1521-3935(19980401)199:4<489::Aid-macp489>3.0.Co;2-a

(44) Bartlett, M. D.; Case, S. W.; Kinloch, A. J.; Dillard, D. A. Peel Tests for Quantifying Adhesion and Toughness: A Review. *Progress in Materials Science* **2023**, *137*. DOI: 10.1016/j.pmatsci.2023.101086

(45) Qian, J.; Lin, J.; Xu, G.-K.; Lin, Y.; Gao, H. Thermally Assisted Peeling of an Elastic Strip in Adhesion with a Substrate Via Molecular Bonds. *Journal of the Mechanics and Physics of Solids* **2017**, *101*, 197-208. DOI: 10.1016/j.jmps.2017.01.007

(46) Vajpayee, S.; Khare, K.; Yang, S.; Hui, C.-Y.; Jagota, A. Adhesion Selectivity Using Rippled Surfaces. *Advanced Functional Materials* **2011**, *21* (3), 547-555. DOI: 10.1002/adfm.201001652

(47) Ghatak, A.; Mahadevan, L.; Chaudhury, M. K. Measuring the Work of Adhesion between a Soft Confined Film and a Flexible Plate. *Langmuir* **2005**, *21* (4), 1277-1281. DOI: 10.1021/la0484826

(48) Cedano-Serrano, F. J.; Sidoli, U.; Synytska, A.; Tran, Y.; Hourdet, D.; Creton, C. From Molecular Electrostatic Interactions and Hydrogel Architecture to Macroscopic Underwater Adherence. *Macromolecules* **2019**, *52* (10), 3852-3862. DOI: 10.1021/acs.macromol.8b02696

(49) Levine, M.; Ilkka, G.; Weiss, P. Relation of the Critical Surface Tension of Polymers to Adhesion. *Journal of Polymer Science Part B: Polymer Letters* **1964**, *2* (9), 915-919. DOI: 10.1002/pol.1964.110020918

(50) Musolino, S. F.; Wulff, J. E. Catalytic C–H Oxidation Enhances Polyethylene Bonding. *Chem* **2021**, *7* (1), 7 - 9. DOI: https://doi.org/10.1016/j.chempr.2020.12.019.

(51) Zeng, H.; Huang, J.; Tian, Y.; Li, L.; Tirrell, M. V.; Israelachvili, J. N. Adhesion and Detachment Mechanisms between Polymer and Solid Substrate Surfaces: Using Polystyrene–Mica as a Model System. *Macromolecules* **2016**, *49* (14), 5223-5231. DOI: 10.1021/acs.macromol.6b00949

(52) Owens, D. K.; Wendt, R. C. Estimation of the Surface Free Energy of Polymers. *Journal of Applied Polymer Science* **1969**, *13* (8), 1741-1747. DOI: 10.1002/app.1969.070130815

(53) Evans, E.; Ritchie, K. Dynamic Strength of Molecular Adhesion Bonds. *Biophysical Journal* **1997**, *72* (4), 1541-1555. DOI: 10.1016/s0006-3495(97)78802-7

(54) Hänggi, P.; Talkner, P.; Borkovec, M. Reaction-Rate Theory: Fifty Years after Kramers. *Reviews of Modern Physics* **1990**, *62* (2), 251-341. DOI: 10.1103/RevModPhys.62.251

(55) Evans, E. Probing the Relation between Force--Lifetime--and Chemistry in Single Molecular Bonds. *Annu Rev Biophys Biomol Struct* **2001**, *30*, 105-128. DOI: 10.1146/annurev.biophys.30.1.105

(56) Ghatak, A.; Vorvolakos, K.; She, H.; Malotky, D. L.; Chaudhury, M. K. Interfacial Rate Processes in Adhesion and Friction. *The Journal of Physical Chemistry B* **2000**, *104* (17), 4018-4030. DOI: 10.1021/jp9942973

(57) Utzig, T.; Stock, P.; Valtiner, M. Resolving Non-Specific and Specific Adhesive Interactions of Catechols at Solid/Liquid Interfaces at the Molecular Scale. *Angew Chem Int Ed Engl* **2016**, *55* (33), 9524-9528. DOI: 10.1002/anie.201601881

(58) Wang, S.; Panyukov, S.; Rubinstein, M.; Craig, S. L. Quantitative Adjustment to the Molecular Energy Parameter in the Lake–Thomas Theory of Polymer Fracture Energy. *Macromolecules* **2019**, *52* (7), 2772-2777. DOI: 10.1021/acs.macromol.8b02341

(59) Lake, G. J.; Thomas, A. G. The Strength of Highly Elastic Materials. *Proceedings of the Royal Society of London. Series A. Mathematical and Physical Sciences* **1967**, *300* (1460), 108-119. DOI: 10.1098/rspa.1967.0160

(60) Ortiz, C.; Hadziioannou, G. Entropic Elasticity of Single Polymer Chains of Poly(Methacrylic Acid) Measured by Atomic Force Microscopy. *Macromolecules* **1999**, *32* (3), 780-787. DOI: 10.1021/ma981245n

(61) Smith, S. B.; Finzi, L.; Bustamante, C. Direct Mechanical Measurements of the Elasticity of Single DNA Molecules by Using Magnetic Beads. *Science* **1992**, *258* (5085), 1122-1126. DOI: 10.1126/science.1439819

(62) Giannotti, M. I.; Vancso, G. J. Interrogation of Single Synthetic Polymer Chains and Polysaccharides by AFM-Based Force Spectroscopy. *Chemphyschem* **2007**, *8* (16), 2290-2307. DOI: 10.1002/cphc.200700175

(63) Smith, S. B.; Cui, Y.; Bustamante, C. Overstretching B-DNA: The Elastic Response of Individual Double-Stranded and Single-Stranded DNA Molecules. *Science* **1996**, *271* (5250), 795-799. DOI: 10.1126/science.271.5250.795

(64) Lavoie, S. R.; Long, R.; Tang, T. Modeling the Mechanics of Polymer Chains with Deformable and Active Bonds. *J Phys Chem B* **2020**, *124* (1), 253-265. DOI: 10.1021/acs.jpcb.9b09068

(65) Griffith, A. A. Vi. The Phenomena of Rupture and Flow in Solids. *Philosophical Transactions of the Royal Society of London. Series A, Containing Papers of a Mathematical or Physical Character* **1921**, *221* (582-593), 163-198. DOI: 10.1098/rsta.1921.0006

(66) Creton, C.; Brown, H. R.; Shull, K. R. Molecular Weight Effects in Chain Pullout. *Macromolecules* **1994**, *27*, 3174-3183.

(67) Raphael, E.; de Gennes, P. G. Rubber-Rubber Adhesion with Connector Molecules. *The Journal of Physical Chemistry* **1991**, *1992* (96), 4002-4007.

(68) She, H.; Malotky, D.; Chaudhury, M. K. Estimation of Adhesion Hysteresis at Polymer/Oxide Interfaces Using Rolling Contact Mechanics. *Langmuir* **1998**, *14* (11), 3090-3100. DOI: 10.1021/la971061m

(69) Chaudhury, M. K. Rate-Dependent Fracture at Adhesive Interface. *The Journal of Physical Chemistry B* **1999**, *103* (31), 6562-6566. DOI: 10.1021/jp9906482

(70) Gent, A. N.; Petrich, R. P. Adhesion of Viscoelastic Materials to Rigid Substrates. *Proceedings of the Royal Society of London. A. Mathematical and Physical Sciences* **1969**, *310* (1502), 433-448. DOI: 10.1098/rspa.1969.0085

(71) de Gennes, P. G. Soft Adhesives. *Langmuir* **1996**, *12* (19), 4497-4500. DOI: 10.1021/la950886y

(72) Gent, A. N. Adhesion and Strength of Viscoelastic Solids. Is There a Relationship between Adhesion and Bulk Properties? *Langmuir* **1996**, *12* (19), 4492-4496. DOI: 10.1021/la950887q

(73) Schallamach, A. The Velocity and Temperature Dependence of Rubber Friction. *Proceedings of the Physical Society. Section B* **1953**, *66* (5), 386-392. DOI: 10.1088/0370-1301/66/5/306

(74) Grzelka, M.; Kooij, S.; Woutersen, S.; Adda-Bedia, M.; Bonn, D. Transition from Viscoelastic to Fracture-Like Peeling of Pressure-Sensitive Adhesives. *Soft Matter* **2022**, *18* (5), 999-1004. DOI: 10.1039/d1sm01270c

(75) Mulderrig, J.; Talamini, B.; Bouklas, N. A Statistical Mechanics Framework for Polymer Chain Scission, Based on the Concepts of Distorted Bond Potential and Asymptotic Matching. *Journal of the Mechanics and Physics of Solids* **2023**, *174*. DOI: 10.1016/j.jmps.2023.105244

(76) Lamont, S. C.; Mulderrig, J.; Bouklas, N.; Vernerey, F. J. Rate-Dependent Damage Mechanics of Polymer Networks with Reversible Bonds. *Macromolecules* **2021**, *54* (23), 10801-10813. DOI: 10.1021/acs.macromol.1c01943

(77) Yang, T.; Gandhi, V.; Huang, R.; Liechti, K. M. Rate Dependent Fracture Along a Silicon/Epoxy Interface under Mixed-Mode Loading Conditions. *International Journal of Solids and Structures* **2022**, *257*. DOI: 10.1016/j.ijsolstr.2021.111129

(78) Carre, A.; Schultz, J. Polymer-Aluminium Adhesion. I. The Surface Energy of Aluminium in Relation to Its Surface Treatment. *The Journal of Adhesion* **1983**, *15* (2), 151-161. DOI: 10.1080/00218468308073223

(79) Greenwood, J. A.; Williamson, J. B. P. Contact of Nominally Flat Surfaces. *Proceedings of the Royal Society of London. A. Mathematical and Physical Sciences* **1966**, *295* (1442), 300-319. DOI: https://www.jstor.org/stable/2415421

(80) Hyun, S.; Pei, L.; Molinari, J. F.; Robbins, M. O. Finite-Element Analysis of Contact between Elastic Self-Affine Surfaces. *Phys Rev E Stat Nonlin Soft Matter Phys* **2004**, *70* (2 Pt 2), 026117. DOI: 10.1103/PhysRevE.70.026117

(81) Persson, B. N. Elastoplastic Contact between Randomly Rough Surfaces. *Phys Rev Lett* **2001**, *87* (11), 116101. DOI: 10.1103/PhysRevLett.87.116101

(82) Persson, B. N. Relation between Interfacial Separation and Load: A General Theory of Contact Mechanics. *Phys Rev Lett* **2007**, *99* (12), 125502. DOI: 10.1103/PhysRevLett.99.125502

(83) Tran, N. T.; Flanagan, D. P.; Orlicki, J. A.; Lenhart, J. L.; Proctor, K. L.; Knorr, D. B., Jr. Polydopamine and Polydopamine-Silane Hybrid Surface Treatments in Structural Adhesive Applications. *Langmuir* **2018**, *34* (4), 1274-1286. DOI: 10.1021/acs.langmuir.7b03178

(84) Britton, J.; Cousens, N. E.; Coles, S. W.; van Engers, C. D.; Babenko, V.; Murdock, A. T.; Koos, A.; Perkin, S.; Grobert, N. A Graphene Surface Force Balance. *Langmuir* **2014**, *30* (38), 11485-11492. DOI: 10.1021/la5028493

(85) Dalvi, S.; Gujrati, A.; Khanal, S. R.; Pastewka, L.; Dhinojwala, A.; Jacobs, T. D. B. Linking Energy Loss in Soft Adhesion to Surface Roughness. *Proc Natl Acad Sci U S A* **2019**, *116* (51), 25484-25490. DOI: 10.1073/pnas.1913126116

(86) Christenson, H. K. Adhesion and Surface Energy of Mica in Air and Water. *The Journal of Physical Chemistry* **1993**, *97*, 12034-12041.

(87) Christenson, H. K.; Thomson, N. H. The Nature of the Air-Cleaved Mica Surface. *Surface Science Reports* **2016**, *71* (2), 367-390. DOI: 10.1016/j.surfrep.2016.03.001

(88) Mori, K.; Samata, S.; Mitsugi, N.; Teramoto, A.; Kuroda, R.; Suwa, T.; Hashimoto, K.; Sugawa, S. Influence of Silicon Wafer Surface Roughness on Semiconductor Device Characteristics. *Japanese Journal of Applied Physics* **2020**, *59* (SM). DOI: 10.35848/1347-4065/ab918c

(89) Knarr, R. F.; Quon, R. A.; Vanderlick, T. K. Direct Force Measurements at the Smooth Gold/Mica Interface. *Langmuir* **1998**, *14* (22), 6414-6418. DOI: 10.1021/la980133m

(90) Valtiner, M.; Banquy, X.; Kristiansen, K.; Greene, G. W.; Israelachvili, J. N. The Electrochemical Surface Forces Apparatus: The Effect of Surface Roughness, Electrostatic Surface Potentials, and Anodic Oxide Growth on Interaction Forces, and Friction between Dissimilar Surfaces in Aqueous Solutions. *Langmuir* **2012**, *28* (36), 13080-13093. DOI: 10.1021/la3018216

(91) Karnal, P. Adhesion of a Viscoelastic Polymer to Wet or Compliant Substrates. Johns Hopkins University, Baltimore, MD, 2021.

(92) Gent, A. N.; Schultz, J. Effect of Wetting Liquids on the Strength of Adhesion of Viscoelastic Material. *The Journal of Adhesion* **1972**, *3* (4), 281-294. DOI: 10.1080/00218467208072199

(93) Creton, C. Pressure-Sensitive Adhesives: An Introductory Course. *MRS Bulletin* **2011**, *28* (6), 434-439. DOI: 10.1557/mrs2003.124

(94) Chan, E. P.; Hu, Y.; Johnson, P. M.; Suo, Z.; Stafford, C. M. Spherical Indentation Testing of Poroelastic Relaxations in Thin Hydrogel Layers. *Soft Matter* **2012**, *8* (5), 1492-1498. DOI: 10.1039/c1sm06514a

(95) Delavoipiere, J.; Tran, Y.; Verneuil, E.; Chateauminois, A. Poroelastic Indentation of Mechanically Confined Hydrogel Layers. *Soft Matter* **2016**, *12* (38), 8049-8058. DOI: 10.1039/c6sm01448h

(96) Jha, A.; Karnal, P.; Frechette, J. Adhesion of Fluid Infused Silicone Elastomer to Glass. *Soft Matter* **2022**, *18* (39), 7579-7592. DOI: 10.1039/d2sm00875k

(97) Degen, G. D.; Chen, Y. T.; Chau, A. L.; Mansson, L. K.; Pitenis, A. A. Poroelasticity of Highly Confined Hydrogel Films Measured with a Surface Forces Apparatus. *Soft Matter* **2020**, *16* (35), 8096-8100. DOI: 10.1039/d0sm01312a

(98) Reale, E. R.; Dunn, A. C. Poroelasticity-Driven Lubrication in Hydrogel Interfaces. *Soft Matter* **2017**, *13* (2), 428-435. DOI: 10.1039/c6sm02111e

(99) Shoaib, T.; Espinosa-Marzal, R. M. Insight into the Viscous and Adhesive Contributions to Hydrogel Friction. *Tribology Letters* **2018**, *66* (3). DOI: 10.1007/s11249-018-1045-7

(100) McGhee, E. O.; Hart, S. M.; Uruena, J. M.; Sawyer, W. G. Hydration Control of Gel-Adhesion and Muco-Adhesion. *Langmuir* **2019**, *35* (48), 15769-15775. DOI: 10.1021/acs.langmuir.9b02816

(101) Maugis, D. Adherence of Elastomers: Fracture Mechanics Aspects. *Journal of Adhesion Science and Technology* **1987**, *1* (1), 105-134. DOI: 10.1163/156856187x00120

(102) Gent, A. N.; Hamed, G. R.; Hung, W. J. Adhesion of Elastomers: Dwell Time Effects. *The Journal of Adhesion* **2003**, *79* (4), 315-325. DOI: 10.1080/00218460309584

(103) Liu, Y.; Szlufarska, I. Chemical Origins of Frictional Aging. *Phys Rev Lett* **2012**, *109* (18), 186102. DOI: 10.1103/PhysRevLett.109.186102

(104) Creton, C.; Leibler, L. How Does Tack Depend on Time of Contact and Contact Pressure? *Journal of Polymer Science Part B: Polymer Physics* **1996**, *34* (3), 545-554. DOI: https://doi.org/10.1002/(SICI)1099-0488(199602)34:3%3C545::AID-POLB13%3E3.0.CO;2-I

(105) Thiemecke, J.; Hensel, R. Contact Aging Enhances Adhesion of Micropatterned Silicone Adhesives to Glass Substrates. *Advanced Functional Materials* **2020**, *30* (50). DOI: 10.1002/adfm.202005826

(106) Golan, Y.; Alcantar, N. A.; Kuhl, T. L.; Israelachvili, J. Generic Substrate for the Surface Forces Apparatus: Deposition and Characterization of Silicon Nitride Surfaces. *Langmuir* **2000**, *16* (17), 6955-6960. DOI: 10.1021/la000125h

(107) Fujii, S.; Kasuya, M.; Kurihara, K. Characterization of Platinum Electrode Surfaces by Electrochemical Surface Forces Measurement. *The Journal of Physical Chemistry C* **2017**, *121* (47), 26406-26413. DOI: 10.1021/acs.jpcc.7b09301

(108) Ren, H. Y.; Mizukami, M.; Kurihara, K. Preparation of Stable Silica Surfaces for Surface Forces Measurement. *Rev Sci Instrum* **2017**, *88* (9), 095108. DOI: 10.1063/1.4986613

(109) de Aguiar, H. B.; McGraw, J. D.; Donaldson, S. H., Jr. Interface-Sensitive Raman Microspectroscopy of Water Via Confinement with a Multimodal Miniature Surface Forces Apparatus. *Langmuir* **2019**, *35* (48), 15543-15551. DOI: 10.1021/acs.langmuir.9b01889

(110) Dobbs, H. A.; Kaufman, Y.; Scott, J.; Kristiansen, K.; Schrader, A. M.; Chen, S. Y.; Duda, P.; Israelachvili, J. N. Ultra-Smooth, Chemically Functional Silica Surfaces for Surface Interaction Measurements and Optical/Interferometry-Based Techniques. *Advanced Engineering Materials* **2017**, *20* (2). DOI: 10.1002/adem.201700630

(111) Kasuya, M.; Tomita, K.; Hino, M.; Mizukami, M.; Mori, H.; Kajita, S.; Ohmori, T.; Suzuki, A.; Kurihara, K. Nanotribological Characterization of Lubricants between Smooth Iron Surfaces. *Langmuir* **2017**, *33* (16), 3941-3948. DOI: 10.1021/acs.langmuir.7b00148

(112) Tivony, R.; Safran, S.; Pincus, P.; Silbert, G.; Klein, J. Charging Dynamics of an Individual Nanopore. *Nat Commun* **2018**, *9* (1), 4203. DOI: 10.1038/s41467-018-06364-1

(113) Pastewka, L.; Robbins, M. O. Contact between Rough Surfaces and a Criterion for Macroscopic Adhesion. *Proc Natl Acad Sci U S A* **2014**, *111* (9), 3298-3303. DOI: 10.1073/pnas.1320846111

(114) Bhattacharjee, S.; Ko, C.-H.; Elimelech, M. Dlvo Interaction between Rough Surfaces. *Langmuir* **1998**, *14* (12), 3365-3375. DOI: 10.1021/la971360b

(115) Koinkar, V. N.; Bhushan, B. Effect of Scan Size and Surface Roughness on Microscale Friction Measurements. *Journal of Applied Physics* **1997**, *81* (6), 2472-2479. DOI: 10.1063/1.363954

(116) Valtiner, M.; Kristiansen, K.; Greene, G. W.; Israelachvili, J. N. Effect of Surface Roughness and Electrostatic Surface Potentials on Forces between Dissimilar Surfaces in Aqueous Solution. *Adv Mater* **2011**, *23* (20), 2294-2299. DOI: 10.1002/adma.201003709

(117) Monti, J. M.; McGuiggan, P. M.; Robbins, M. O. Effect of Roughness and Elasticity on Interactions between Charged Colloidal Spheres. *Langmuir* **2019**, *35* (48), 15948-15959. DOI: 10.1021/acs.langmuir.9b02161

(118) Vogel, N.; Zieleniecki, J.; Koper, I. As Flat as It Gets: Ultrasmooth Surfaces from Template-Stripping Procedures. *Nanoscale* **2012**, *4* (13), 3820-3832. DOI: 10.1039/c2nr30434a

(119) Chai, L.; Klein, J. Large Area, Molecularly Smooth (0.2 Nm Rms) Gold Films for Surface Forces and Other Studies. *Langmuir* **2007**, *23* (14), 7777-7783. DOI: 10.1021/la063738o

(120) Tivony, R.; Yaakov, D. B.; Silbert, G.; Klein, J. Direct Observation of Confinement-Induced Charge Inversion at a Metal Surface. *Langmuir* **2015**, *31* (47), 12845-12849. DOI: 10.1021/acs.langmuir.5b03326

(121) Bray, E. L. *Usgs: Aluminum Statistics and Information*. https://www.usgs.gov/centers/nmic/aluminum-statistics-and-information (accessed 2020 Mar 1, 2020).

(122) Rode, D. L.; Gaddam, V. R.; Yi, J. H. Subnanometer Surface Roughness of Dc Magnetron Sputtered Al Films. *Journal of Applied Physics* **2007**, *102* (2). DOI: 10.1063/1.2756039

(123) Higo, M.; Lu, X.; Mazur, U.; Hipps, K. W. Preparation of Atomically Smooth Aluminum Films: Characterization by Transmission Electron Microscopy and Atomic Force Microscopy. *Langmuir* **1997**, *13* (23), 6176-6182. DOI: 10.1021/la9703959

(124) Levine, I.; Yoffe, A.; Salomon, A.; Li, W.; Feldman, Y.; Vilan, A. Epitaxial Two Dimensional Aluminum Films on Silicon (111) by Ultra-Fast Thermal Deposition. *Journal of Applied Physics* **2012**, *111* (12). DOI: 10.1063/1.4730411

(125) Bordo, K.; Rubahn, H.-G. Effect of Deposition Rate on Structure and Surface Morphology of Thin Evaporated Al Films on Dielectrics and Semiconductors. *Materials Science* **2012**, *18* (4). DOI: 10.5755/j01.ms.18.4.3088

(126) McPeak, K. M.; Jayanti, S. V.; Kress, S. J.; Meyer, S.; Iotti, S.; Rossinelli, A.; Norris, D. J. Plasmonic Films Can Easily Be Better: Rules and Recipes. *ACS Photonics* **2015**, *2* (3), 326-333. DOI: 10.1021/ph5004237

(127) Rossetti, F. F.; Reviakine, I.; Textor, M. Characterization of Titanium Oxide Films Prepared by the Template-Stripping Method. *Langmuir* **2003**, *19* (24), 10116-10123. DOI: 10.1021/la034280i

(128) Perkin, S.; Chai, L.; Kampf, N.; Raviv, U.; Briscoe, W.; Dunlop, I.; Titmuss, S.; Seo, M.; Kumacheva, E.; Klein, J. Forces between Mica Surfaces, Prepared in Different Ways, across Aqueous and Nonaqueous Liquids Confined to Molecularly Thin Films. *Langmuir* **2006**, *22* (14), 6142-6152. DOI: 10.1021/la053097h

(129) Nečas, D.; Klapetek, P. Gwyddion: An Open-Source Software for Spm Data Analysis. *Open Physics* **2012**, *10* (1). DOI: 10.2478/s11534-011-0096-2

(130) Israelachvili, J.; Min, Y.; Akbulut, M.; Alig, A.; Carver, G.; Greene, W.; Kristiansen, K.; Meyer, E.; Pesika, N.; Rosenberg, K.; et al. Recent Advances in the Surface Forces Apparatus (SFA) Technique. *Reports on Progress in Physics* **2010**, *73* (3). DOI: 10.1088/0034-4885/73/3/036601

(131) Heuberger, M. The Extended Surface Forces Apparatus. Part I. Fast Spectral Correlation Interferometry. *Review of Scientific Instruments* **2001**, *72* (3). DOI: 10.1063/1.1347978

(132) Schwenzfeier, K. A.; Erbe, A.; Bilotto, P.; Lengauer, M.; Merola, C.; Cheng, H. W.; Mears, L. L. E.; Valtiner, M. Optimizing Multiple Beam Interferometry in the Surface Forces Apparatus: Novel Optics, Reflection Mode Modeling, Metal Layer Thicknesses, Birefringence, and Rotation of Anisotropic Layers. *Rev Sci Instrum* **2019**, *90* (4), 043908. DOI: 10.1063/1.5085210

(133) Rakic, A. D.; Djurisic, A. B.; Elazar, J. M.; Majewski, M. L. Optical Properties of Metallic Films for Vertical-Cavity Optoelectronic Devices. *Appl Opt* **1998**, *37* (22), 5271-5283. DOI: 10.1364/ao.37.005271

(134) Kienle, D. F.; de Souza, J. V.; Watkins, E. B.; Kuhl, T. L. Thickness and Refractive Index of Dppc and Dppe Monolayers by Multiple-Beam Interferometry. *Anal Bioanal Chem* **2014**, *406* (19), 4725-4733. DOI: 10.1007/s00216-014-7866-9

(135) McGuiggan, P. M.; Wallace, J. S.; Smith, D. T.; Sridhar, I.; Zheng, Z. W.; Johnson, K. L. Contact Mechanics of Layered Elastic Materials: Experiment and Theory. *Journal of Physics D: Applied Physics* **2007**, *40* (19), 5984-5994. DOI: 10.1088/0022-3727/40/19/031

(136) Derjaguin, B.; Landau, L. Theory of the Stability of Strongly Charged Lyophobic Sols and of the Adhesion of Strongly Charged Particles in Solutions of Electrolytes. *Progress in Surface Science* **1993**, *43* (1-4), 30-59. DOI: 10.1016/0079-6816(93)90013-l

(137) Verwey, E. J. W. O., J. T. *Theory of Stability of Lyophobic Colloids*; 1948.

(138) Pick, C.; Argento, C.; Drazer, G.; Frechette, J. Micropatterned Charge Heterogeneities Via Vapor Deposition of Aminosilanes. *Langmuir* **2015**, *31* (39), 10725-10733. DOI: 10.1021/acs.langmuir.5b02771

(139) Fréchette, J.; Vanderlick, T. K. Double Layer Forces over Large Potential Ranges as Measured in an Electrochemical Surface Forces Apparatus. *Langmuir* **2001**, *17* (24), 7620-7627. DOI: 10.1021/la011087k

(140) Liakos, I. L.; Newman, R. C.; McAlpine, E.; Alexander, M. R. Study of the Resistance of Sams on Aluminium to Acidic and Basic Solutions Using Dynamic Contact Angle Measurement. *Langmuir* **2007**, *23* (3), 995-999. DOI: 10.1021/la062233v

(141) Michel, R.; Lussi, J. W.; Csucs, G.; Reviakine, I.; Danuser, G.; Ketterer, B.; Hubbell, J. A.; Textor, M.; Spencer, N. D. Selective Molecular Assembly Patterning: A New Approach to Micro- and Nanochemical Patterning of Surfaces for Biological Applications. *Langmuir* **2002**, *18* (8), 3281-3287. DOI: 10.1021/la011715y

(142) Kaiser, N. Review of the Fundamentals of Thin-Film Growth. *Appl Opt* **2002**, *41* (16), 3053-3060. DOI: 10.1364/ao.41.003053

(143) Vedder, W.; Vermilyea, D. A. Aluminum + Water Reaction. *Transactions of the Faraday Society* **1969**, *65*. DOI: 10.1039/tf9696500561

(144) Chang, C. C.; Fraser, D. B.; Grieco, M. J.; Sheng, T. T.; Haszko, S. E.; Kerwin, R. E.; Marcus, R. B.; Sinha, A. K. Aluminum Oxidation in Water. *Journal of The Electrochemical Society* **2019**, *125* (5), 787-792. DOI: 10.1149/1.2131549

(145) McPeak, K. M.; van Engers, C. D.; Bianchi, S.; Rossinelli, A.; Poulikakos, L. V.; Bernard, L.; Herrmann, S.; Kim, D. K.; Burger, S.; Blome, M.; et al. Ultraviolet Plasmonic Chirality from Colloidal Aluminum Nanoparticles Exhibiting Charge-Selective Protein Detection. *Adv Mater* **2015**, *27* (40), 6244-6250. DOI: 10.1002/adma.201503493

(146) Bailey, A. I.; Kay, S. M. Measurement of Refractive Index and Dispersion of Mica, Employing Multiple Beam Interference Techniques. *British Journal of Applied Physics* **1965**, *16* (1), 39-44. DOI: 10.1088/0508-3443/16/1/307

(147) Ducker, W. A.; Xu, Z.; Clarke, D. R.; Israelachvili, J. N. Forces between Alumina Surfaces in Salt Solutions: Non-Dlvo Forces and the Implications for Colloidal Processing. *Journal of the American Ceramic Society* **1994**, *77* (2), 437-443. DOI: 10.1111/j.1151-2916.1994.tb07012.x

(148) Horn, R. G.; Clarke, D. R.; Clarkson, M. T. Direct Measurement of Surface Forces between Sapphire Crystals in Aqueous Solutions. *Journal of Materials Research* **2011**, *3* (3), 413-416. DOI: 10.1557/jmr.1988.0413

(149) Franks, G. V.; Gan, Y. Charging Behavior at the Alumina–Water Interface and Implications for Ceramic Processing. *Journal of the American Ceramic Society* **2007**, *90* (11), 3373-3388. DOI: 10.1111/j.1551-2916.2007.02013.x

(150) Cherepy, N. J.; Shen, T. H.; Esposito, A. P.; Tillotson, T. M. Characterization of an Effective Cleaning Procedure for Aluminum Alloys: Surface Enhanced Raman Spectroscopy and Zeta Potential Analysis. *J Colloid Interface Sci* **2005**, *282* (1), 80-86. DOI: 10.1016/j.jcis.2004.08.064

(151) Zadorozne, N. S.; Giordano, C. M.; Rodríguez, M. A.; Carranza, R. M.; Rebak, R. B. Crevice Corrosion Kinetics of Nickel Alloys Bearing Chromium and Molybdenum. *Electrochimica Acta* **2012**, *76*, 94-101. DOI: 10.1016/j.electacta.2012.04.157

(152) Shrestha, B. R.; Hu, Q.; Baimpos, T.; Kristiansen, K.; Israelachvili, J. N.; Valtiner, M. Real-Time Monitoring of Aluminum Crevice Corrosion and Its Inhibition by Vanadates with Multiple Beam Interferometry in a Surface Forces Apparatus. *Journal of The Electrochemical Society* **2015**, *162* (7), C327-C332. DOI: 10.1149/2.0501507jes

(153) Merola, C.; Cheng, H. W.; Schwenzfeier, K.; Kristiansen, K.; Chen, Y. J.; Dobbs, H. A.; Israelachvili, J. N.; Valtiner, M. In Situ Nano- to Microscopic Imaging and Growth Mechanism of Electrochemical Dissolution (E.G., Corrosion) of a Confined Metal Surface. *Proc Natl Acad Sci U S A* **2017**, *114* (36), 9541-9546. DOI: 10.1073/pnas.1708205114

(154) Shriver, D. F.; Weller, M. T.; Overton, T.; Rourke, J.; Armstrong, F. A. *Inorganic Chemistry*; W. H. Freeman & Co., 2014, p^pp 229.

(155) Anderson, T. H.; Yu, J.; Estrada, A.; Hammer, M. U.; Waite, J. H.; Israelachvili, J. N. The Contribution of Dopa to Substrate-Peptide Adhesion and Internal Cohesion of Mussel-Inspired Synthetic Peptide Films. *Adv Funct Mater* **2010**, *20* (23), 4196-4205. DOI: 10.1002/adfm.201000932

(156) Faghihnejad, A.; Feldman, K. E.; Yu, J.; Tirrell, M. V.; Israelachvili, J. N.; Hawker, C. J.; Kramer, E. J.; Zeng, H. Adhesion and Surface Interactions of a Self-Healing Polymer with Multiple Hydrogen-Bonding Groups. *Advanced Functional Materials* **2014**, *24* (16), 2322-2333. DOI: 10.1002/adfm.201303013

(157) Chen, J.; Wu, M.; Gong, L.; Zhang, J.; Yan, B.; Liu, J.; Zhang, H.; Thundat, T.; Zeng, H. Mechanistic Understanding and Nanomechanics of Multiple Hydrogen-Bonding Interactions in Aqueous Environment. *The Journal of Physical Chemistry C* **2019**, *123* (7), 4540-4548. DOI: 10.1021/acs.jpcc.8b11790

(158) Yu, J.; Kan, Y.; Rapp, M.; Danner, E.; Wei, W.; Das, S.; Miller, D. R.; Chen, Y.; Waite, J. H.; Israelachvili, J. N. Adaptive Hydrophobic and Hydrophilic Interactions of Mussel Foot Proteins with Organic Thin Films. *Proc Natl Acad Sci U S A* **2013**, *110* (39), 15680-15685. DOI: 10.1073/pnas.1315015110

(159) Tran, N. T.; Boyer, A. J.; Knorr, D. B. Multiple Local Hydroxyl Groups as a Way to Improve Bond Strength and Durability in Structural Adhesives. *The Journal of Adhesion* **2021**, 1-21. DOI: 10.1080/00218464.2021.1939692

(160) Zhang, F.; Yang, X.; Wang, H.-P.; Zhang, X.; Xia, Y.; Zhou, Q. Durability of Adhesively-Bonded Single Lap–Shear Joints in Accelerated Hygrothermal Exposure for Automotive Applications. *International Journal of Adhesion and Adhesives* **2013**, *44*, 130-137. DOI: 10.1016/j.ijadhadh.2013.02.009

(161) Jiang, X.; Kolstein, H.; Bijlaard, F. S. K. Moisture Diffusion and Hygrothermal Aging in Pultruded Fibre Reinforced Polymer Composites of Bridge Decks. *Materials & Design* **2012**, *37*, 304-312. DOI: 10.1016/j.matdes.2012.01.017

(162) Levins, J. M. V., T. Kyle. Extended Spectral Analysis of Multiple Beam Interferometry: A Technique to Study Metallic Films in the Surface Forces Apparatus. *Langmuir* **1994**, *10*, 2389-2394.

(163) Yu, Y.; Zhang, Y.; Jiang, Z.; Zhang, X.; Zhang, H.; Wang, X. Full View of Single-Molecule Force Spectroscopy of Polyaniline in Oxidized, Reduced, and Doped States. *Langmuir* **2009**, *25* (17), 10002-10006. DOI: 10.1021/la901169p

(164) Zou, S.; Schönherr, H.; Vancso, G. J. Stretching and Rupturing Individual Supramolecular Polymer Chains by AFM. *Angewandte Chemie* **2005**, *117* (6), 978-981. DOI: 10.1002/ange.200460963

(165) Li, H.; Liu, B.; Zhang, X.; Gao, C.; Shen, J.; Zou, G. Single-Molecule Force Spectroscopy on Poly(Acrylic Acid) by AFM. *Langmuir* **1999**, *15* (6), 2120-2124. DOI: 10.1021/la9800304

(166) Wang, J.; Kalinichev, A. G.; Kirkpatrick, R. J. Effects of Substrate Structure and Composition on the Structure, Dynamics, and Energetics of Water at Mineral Surfaces: A Molecular Dynamics Modeling Study. *Geochimica et Cosmochimica Acta* **2006**, *70* (3), 562-582. DOI: 10.1016/j.gca.2005.10.006

(167) Wang, J.; Kalinichev, A. G.; Kirkpatrick, R. J. Asymmetric Hydrogen Bonding and Orientational Ordering of Water at Hydrophobic and Hydrophilic Surfaces: A Comparison of Water/Vapor, Water/Talc, and Water/Mica Interfaces. *The Journal of Physical Chemistry C* **2009**, *113* (25), 11077-11085. DOI: 10.1021/jp9018316

(168) Spruijt, E.; van den Berg, S. A.; Cohen Stuart, M. A.; van der Gucht, J. Direct Measurement of the Strength of Single Ionic Bonds between Hydrated Charges. *ACS Nano* **2012**, *6* (6), 5297-5303. DOI: 10.1021/nn301097y

(169) Han, L.; Gong, L.; Chen, J.; Zhang, J.; Xiang, L.; Zhang, L.; Wang, Q.; Yan, B.; Zeng, H. Universal Mussel-Inspired Ultrastable Surface-Anchoring Strategy Via Adaptive Synergy of Catechol and Cations. *ACS Appl Mater Interfaces* **2018**, *10* (2), 2166-2173. DOI: 10.1021/acsami.7b15756

(170) Martiniano, H. F.; Galamba, N. Insights on Hydrogen-Bond Lifetimes in Liquid and Supercooled Water. *J Phys Chem B* **2013**, *117* (50), 16188-16195. DOI: 10.1021/jp407768u

(171) Degen, G. D.; Cristiani, T. R.; Cadirov, N.; Andresen Eguiluz, R. C.; Kristiansen, K.; Pitenis, A. A.; Israelachvili, J. N. Surface Damage Influences the JKR Contact Mechanics of Glassy Low-Molecular-Weight Polystyrene Films. *Langmuir* **2019**, *35* (48), 15674-15680. DOI: 10.1021/acs.langmuir.9b02037

(172) Sridhar, I.; Johnson, K. L.; Fleck, N. A. Adhesion Mechanics of the Surface Force Apparatus. *Journal of Physics D: Applied Physics* **1997**, *30* (12), 1710-1719. DOI: 10.1088/0022-3727/30/12/004

(173) Bergström, L. Hamaker Constants of Inorganic Materials. *Advances in Colloid and Interface Science* **1997**, *70*, 125-169. DOI: 10.1016/s0001-8686(97)00003-1

(174) Steinberg, S.; Ducker, W.; Vigil, G.; Hyukjin, C.; Frank, C.; Tseng, M. Z.; Clarke, D. R.; Israelachvili, J. N. Van Der Waals Epitaxial Growth of Agr-Alumina Nanocrystals on Mica. *Science* **1993**, *260* (5108), 656-659. DOI: 10.1126/science.260.5108.656

(175) Sheppard, N. F.; Senturia, S. D. Chemical Interpretation of the Relaxed Permittivity During Epoxy Resin Cure. *Polymer Engineering and Science* **1986**, *26* (5), 354-357. DOI: 10.1002/pen.760260505

(176) Yeh, I.-C.; Lenhart, J. L.; Rinderspacher, B. C. Molecular Dynamics Simulations of Adsorption of Catechol and Related Phenolic Compounds to Alumina Surfaces. *The Journal of Physical Chemistry C* **2015**, *119* (14), 7721-7731. DOI: 10.1021/jp512780s

(177) Higuchi, C.; Tanaka, H.; Yoshizawa, K. Molecular Understanding of the Adhesive Interactions between Silica Surface and Epoxy Resin: Effects of Interfacial Water. *J Comput Chem* **2019**, *40* (1), 164-171. DOI: 10.1002/jcc.25559

(178) Bahlakeh, G.; Ramezanzadeh, B. A Detailed Molecular Dynamics Simulation and Experimental Investigation on the Interfacial Bonding Mechanism of an Epoxy Adhesive on Carbon Steel Sheets Decorated with a Novel Cerium-Lanthanum Nanofilm. *ACS Appl Mater Interfaces* **2017**, *9* (20), 17536-17551. DOI: 10.1021/acsami.7b00644

(179) Tam, L.-h.; Lau, D. Moisture Effect on the Mechanical and Interfacial Properties of Epoxy-Bonded Material System: An Atomistic and Experimental Investigation. *Polymer* **2015**, *57*, 132-142. DOI: 10.1016/j.polymer.2014.12.026

(180) Mian, S. A.; Saha, L. C.; Jang, J.; Wang, L.; Gao, X.; Nagase, S. Density Functional Theory Study of Catechol Adhesion on Silica Surfaces. *The Journal of Physical Chemistry C* **2010**, *114* (48), 20793-20800. DOI: 10.1021/jp1070538

(181) Mian, S. A.; Yang, L. M.; Saha, L. C.; Ahmed, E.; Ajmal, M.; Ganz, E. A Fundamental Understanding of Catechol and Water Adsorption on a Hydrophilic Silica Surface: Exploring the

Underwater Adhesion Mechanism of Mussels on an Atomic Scale. *Langmuir* **2014**, *30* (23), 6906-6914. DOI: 10.1021/la500800f

(182) Mc Aninch, I. M.; Palmese, G. R.; Lenhart, J. L.; La Scala, J. J. Epoxy-Amine Networks with Varying Epoxy Polydispersity. *Journal of Applied Polymer Science* **2015**, *132* (8), n/a-n/a. DOI: 10.1002/app.41503

(183) Pate, K. D. Applications of Adheives in Aerospace. In *Surfaces, Chemistry, & Applicaitions*, Chaudhury, M. K., Pocius, A. V. Eds.; Adhesion Science and Engineering - 2, Vol. 1; Elsevier Science, 2002; pp 1129-1192.

(184) Schneberger, G. L. Adhesives in the Automotive Industry. In *Handbook of Adhesives*, 3rd ed.; Skeist, I. Ed.; Van Nostrand Reinhold, 1990; pp 729-735.

(185) Kinloch, A. J. Toughening Epoxy Adhesives to Meet Today's Challenges. *MRS Bulletin* **2011**, *28* (6), 445-448. DOI: 10.1557/mrs2003.126

(186) Hart-Smith, L. J. The Design of Adhesively Bonded Joints. In *The Mechanics of Adhesion*, Dillard, D. A., Pocius, A. V. Eds.; Adhesion Science and Engineering, Vol. 1; Elsevier Science, 2002; pp 725-777.

(187) Knorr, D. B.; Yu, J. H.; Richardson, A. D.; Hindenlang, M. D.; McAninch, I. M.; La Scala, J. J.; Lenhart, J. L. Glass Transition Dependence of Ultrahigh Strain Rate Response in Amine Cured Epoxy Resins. *Polymer* **2012**, *53* (25), 5917-5923. DOI: 10.1016/j.polymer.2012.09.058

(188) da Silva, L. F. M.; Adams, R. D. Measurement of the Mechanical Properties of Structural Adhesives in Tension and Shear over a Wide Range of Temperatures. *Journal of Adhesion Science and Technology* **2005**, *19* (2), 109-141. DOI: 10.1163/1568561053148449

(189) Adams, R. D.; Coppendale, J.; Mallick, V.; Al-Hamdan, H. The Effect of Temperature on the Strength of Adhesive Joints. *International Journal of Adhesion and Adhesives* **1992**, *12* (3), 185-190. DOI: 10.1016/0143-7496(92)90052-w

(190) Kinloch, A. J. The Durability of Adhesive Joints. In *The Mechanics of Adhesion*, dillard, D. A., Poicus, A. V. Eds.; Adhesion Science and Engineering, Vol. 1; Elsevier Science, 2002; pp 661-698.

(191) Lee, H.; Dellatore, S. M.; Miller, W. M.; Messersmith, P. B. Mussel-Inspired Surface Chemistry for Multifunctional Coatings. *Science* **2007**, *318* (5849), 426-430. DOI: 10.1126/science.1147241

(192) Laurendeau, N. M. *Statistical Thermodynamics: Fundamentals and Applications*; Cambridge University Press, 2005.

(193) Plazek, D. J.; Frund, Z. N. Epoxy Resins (Dgeba): The Curing and Physical Aging Process. *Journal of Polymer Science Part B: Polymer Physics* **1990**, *28* (4), 431-448. DOI: 10.1002/polb.1990.090280401

(194) Cherdoud-Chihani, A.; Mouzali, M.; Abadie, M. J. M. Study of Crosslinking Acid Copolymer/Dgeba Systems by Ftir. *Journal of Applied Polymer Science* **2003**, *87* (13), 2033-2051. DOI: 10.1002/app.11389

(195) Reis, J. M. L.; Amorim, F. C.; da Silva, A. H. M. F. T.; da Costa Mattos, H. S. Influence of Temperature on the Behavior of Dgeba (Bisphenol a Diglycidyl Ether) Epoxy Adhesive. *International Journal of Adhesion and Adhesives* **2015**, *58*, 88-92. DOI: 10.1016/j.ijadhadh.2015.01.013

(196) Schmidt, R. G.; Bell, J. P. Epoxy Adhesion to Metals. In *Epoxy Resins and Composites Ii*, Dusek, K. Ed.; Advances in Polymer Science, Springer, 1986; pp 33-71.

(197) Apicella, A.; Nicolais, L. Effect of Water on the Properties of Epoxy Matrix and Composite. In *Epoxy Resins and Composites I*, Advances in Polymer Science, Springer, 1985; pp 69-77.

(198) Janshoff, A.; Neitzert, M.; Oberdorfer, Y.; Fuchs, H. Force Spectroscopy of Molecular Systems-Single Molecule Spectroscopy of Polymers and Biomolecules. *Angew Chem Int Ed Engl* **2000**, *39* (18), 3212-3237. DOI: 10.1002/1521-3773(20000915)39:18<3212::aid-anie3212>3.0.co;2-x

(199) Schlierf, M.; Rief, M. Temperature Softening of a Protein in Single-Molecule Experiments. *J Mol Biol* **2005**, *354* (2), 497-503. DOI: 10.1016/j.jmb.2005.09.070

(200) Berg, J. C. Semi-Empirical Strategies for Predicting Adhesion. In *Surfaces, Chemistry, and Applications*, Chaudhury, M. K., Pocius, A. V. Eds.; Adhesion Science and Engineering, Vol. 1; Elsevier Science, 2002; pp 1-73.

(201) Gent, A. N.; Hamad, G. R. Fundamentals of Adhesion. In *Handbook of Adhesives*, 3rd ed.; Skeist, I. Ed.; Van Nostrand Reinhold, 1990; pp 39-73.

(202) Meath, A. R. Epoxy Resin Adhesives. In *Handbook of Adhesives*, 3rd ed.; Skeist, I. Ed.; Van Nostrand Reinhold, 1990; pp 347-358.

(203) Dudko, O. K.; Hummer, G.; Szabo, A. Theory, Analysis, and Interpretation of Single-Molecule Force Spectroscopy Experiments. *Proc Natl Acad Sci U S A* **2008**, *105* (41), 15755-15760. DOI: 10.1073/pnas.0806085105

(204) Meredith, H. J.; Jenkins, C. L.; Wilker, J. J. Enhancing the Adhesion of a Biomimetic Polymer Yields Performance Rivaling Commercial Glues. *Advanced Functional Materials* **2014**, *24* (21), 3259-3267. DOI: 10.1002/adfm.201303536

(205) Sun, M.; Kumar, N.; Dhinojwala, A.; King, H. Attractive Forces Slow Contact Formation between Deformable Bodies Underwater. *Proc Natl Acad Sci U S A* **2021**, *118* (41). DOI: 10.1073/pnas.2104975118

(206) Wilson, M. C.; Lu, Q.; Nachtrieb, K. R.; Fuller, J. S.; Skogg, C. M.; Yates, E. A.; Thum, M. D.; So, C. R. Underwater Adhesives Produced by Chemically Induced Protein Aggregation. *Advanced Functional Materials* **2023**. DOI: 10.1002/adfm.202308790

(207) Wang, Y.; Tan, M. R.; Frechette, J. Elastic Deformation of Soft Coatings Due to Lubrication Forces. *Soft Matter* **2017**, *13* (38), 6718-6729. DOI: 10.1039/c7sm01061c

(208) Wang, Y.; Feng, Z.; Frechette, J. Dynamic Adhesion Due to Fluid Infusion. *Current Opinion in Colloid & Interface Science* **2020**, *50*. DOI: 10.1016/j.cocis.2020.101397

(209) Defante, A. P.; Nyarko, A.; Kaur, S.; Burai, T. N.; Dhinojwala, A. Interstitial Water Enhances Sliding Friction. *Langmuir* **2018**, *34* (13), 4084-4094. DOI: 10.1021/acs.langmuir.8b00100